LEABHARLANN CHOLÁISTE NA TRÍONÓIDE, BAILE ÁTHA CLIATH
Ollscoil Átha Cliath

TRINITY COLLEGE LIBRARY DUBLIN
The University of Dublin

Terms and Conditions of Use of Digitised Theses from Trinity College Library Dublin

Copyright statement

All material supplied by Trinity College Library is protected by copyright (under the Copyright and Related Rights Act, 2000 as amended) and other relevant Intellectual Property Rights. By accessing and using a Digitised Thesis from Trinity College Library you acknowledge that all Intellectual Property Rights in any Works supplied are the sole and exclusive property of the copyright and/or other IPR holder. Specific copyright holders may not be explicitly identified. Use of materials from other sources within a thesis should not be construed as a claim over them.

A non-exclusive, non-transferable licence is hereby granted to those using or reproducing, in whole or in part, the material for valid purposes, providing the copyright owners are acknowledged using the normal conventions. Where specific permission to use material is required, this is identified and such permission must be sought from the copyright holder or agency cited.

Liability statement

By using a Digitised Thesis, I accept that Trinity College Dublin bears no legal responsibility for the accuracy, legality or comprehensiveness of materials contained within the thesis, and that Trinity College Dublin accepts no liability for indirect, consequential, or incidental, damages or losses arising from use of the thesis for whatever reason. Information located in a thesis may be subject to specific use constraints, details of which may not be explicitly described. It is the responsibility of potential and actual users to be aware of such constraints and to abide by them. By making use of material from a digitised thesis, you accept these copyright and disclaimer provisions. Where it is brought to the attention of Trinity College Library that there may be a breach of copyright or other restraint, it is the policy to withdraw or take down access to a thesis while the issue is being resolved.

Access Agreement

By using a Digitised Thesis from Trinity College Library you are bound by the following Terms & Conditions. Please read them carefully.

I have read and I understand the following statement: All material supplied via a Digitised Thesis from Trinity College Library is protected by copyright and other intellectual property rights, and duplication or sale of all or part of any of a thesis is not permitted, except that material may be duplicated by you for your research use or for educational purposes in electronic or print form providing the copyright owners are acknowledged using the normal conventions. You must obtain permission for any other use. Electronic or print copies may not be offered, whether for sale or otherwise to anyone. This copy has been supplied on the understanding that it is copyright material and that no quotation from the thesis may be published without proper acknowledgement.

Cerium dioxide redox cycle for fuel production

Brendan Bulfin

School of Physics

Trinity College Dublin

A thesis submitted for the degree of

Doctor of Philosophy

February 2015

Declaration

I declare that this thesis has not been submitted as an exercise for a degree at this or any other university and apart from the advice, assistance and joint effort acknowledged and mentioned in the text, it is entirely my own work.

I agree to deposit this thesis in the University's open access institutional repository or allow the library to do so on my behalf, subject to Irish Copyright Legislation and Trinity College Library conditions of use and acknowledgement.

Brendan Bulfin B. Bulfin.
February 12, 2015

Summary

The following thesis covers a number of topics related to thermochemical fuel production using the CeO_2 redox cycle. Chapter 1 gives an introduction to the topic, providing motivation, historical development and the main physical properties of thermochemical fuel production with emphasis on the ceria redox cycle. The following chapters tackle three separate topics; an analytical description of the ceria redox system, a thermochemical analysis of this fuel production technology and finally an investigation of the effect of dopants on the oxidation and reduction kinetics.

In Chapter 2, an analytical model of cerium oxidation and reduction in an oxygen atmosphere is presented. The system is modelled as an equilibrium reaction with Arrhenius rate constants. By analysing literature equilibrium data, some of the model's constants are determined and conditions are placed on others. In order to fix the remainder of the constants the kinetics of ceria oxidation were investigated. Experimental oxidation and reduction was achieved using a novel experimental apparatus developed and constructed by the author. The apparatus allows oxidation and reduction to be measured via changes in pressure in a sealed vacuum chamber in which ceria samples can be rapidly heated to high temperatures.

The model accurately predicts the equilibrium composition of CeO_2 over a wide range of oxygen partial pressures (10^{-4}–$10^{3}\,\mathrm{Pa}$) and temperatures (1000-1900 °C). It is also shown to agree with the oxidation and reduction of ceria observed using the apparatus discussed above.

Finally, to demonstrate the practicality of the model it was coupled to a radiative heating simulation of a hypothetical cavity receiver. This allows

easy assessment of the effect of different reactor configurations and designs and should prove invaluable to engineers developing this technology.

Chapter 3 presents a thermodynamic evaluation of the technology with an in depth analysis of the energies required to reduce the oxygen partial pressure (pumping) during reduction and sustain the oxidation step. The efficiency of the pumps was given a pressure dependence, determined from the investigation of commercially available vacuum pumps. With this realistic pumping expression and 60% solid state heat recovery (as process heat), the fuel production efficiency of the cycle was maximised with respect to the cycle conditions. The maximum efficiency for a cycle with a reduction temperature of 1500 °C was 11%. Isothermal cycles ($\Delta T = 0$) were found to have poor efficiency under all conditions (< 2 %).

The amount of ceria which is needed per kW of output power was also investigated. For the normal cycle conditions considered, the amount of ceria required was very excessive. It was thus concluded that Ceria's redox properties must be improved and some core technologies, such as efficient vacuum pumps, developed.

In the final chapter, ceria samples doped with both Zr and Hf were examined using the apparatus discussed above to measure their oxidation and reduction kinetics. These particular dopants were investigated as they are known to improve the redox properties of ceria.

The oxidation kinetics became slower upon addition of Zr and Hf dopants, and increasing the dopant concentrations further decreased the oxidation rate. This was quantified using Arrhenius fits of the data. Interestingly the dopants reduced the activation energy of oxidation, but simultaneously greatly reduced the frequency factor, which had the net result of lowering the reaction rates at the temperatures considered.

Larger ceria samples provided by our collaborators at the German Aerospace Centre, with Zr again used as a dopant, were also investigated. These samples offered better measurement resolution and more clearly showed the decrease in oxidation kinetics for increasing Zr concentration.

The reduction kinetics all appeared to be limited by the heating rate (> 50 C° s^{-1}), suggesting that the reduction reaction is extremely rapid.

Acknowledgements

Spending four years working on a Phd is a good way to accumulate a lot of acknowledgements. Firstly, I would like to acknowledge my supervisor, Prof Igor Shvets, for giving me the opportunity to join his group. I have gained a lot from working with Igor and hope I have shared some knowledge in return.

A large amount of thanks is due to a number of members of the applid physics group. Olaf Lübben and Barry Murphy for their friendship and support in work performed on the cluster, and to Karsten Fletcher for his unrelenting patience and guidance. Thanks also to the rest of the Applied Physics Group, both past and present members, especially to Roman Kantor for his friendship and the guidance he offered at the very start of my phd.

Friedemann Call from the DLR in Cologne deserves a special thank you. Friedemann recently moved to Dublin to pursue a collaboration with my branch of the group. He has since become a good friend and an excellent person for scientific debate especially in the areas covered in this thesis.

Without my other college friends, Kyle, Tim, and John, to keep me sane, I don't think I would have made it to the end. Thanks lads. My old housemates and good friends Donal, Marty, Ed and Dan were also always around to bring me back down to earth if I was getting a bit ahead of myself. I would also like to thank my friends from home who have always been a source of encouragement and support.

One of the most important people in my life for the last 3-4 years has been my girlfriend, Matilda. She has been excellent company throughout my studies and never lost her patience over what at times could be described as a chaotic lifestyle.

Finally a big thanks to the family. My Brother Alan and his girlfriend Pii who I see too seldom, have been excellent over the last four years. My two younger sisters Aveen and Aoife have been great fun over the years and help to keep me younger at heart. Finally to my parents Catherine and Coleman who have given me their support and taught me important life lessons for the last 26 years.

I dedicate this thesis to my parents,

Catherine and Colman.

List of publications

1. ***Rotational transitions in a C_{60} monolayer on the WO_2 surface***

   Sergey I. Bozhko, Sergey A. Krasnikov, Olaf Lübben, Barry E. Murphy, Kevin Radican, Valery N. Semenov, Han Chun Wu, **Brendan Bulfin**, and Igor V. Shvets
   Physical Review B **84** (2011) 195412

2. ***Finite element method simulations of heat flow in fixed bed solar water splitting redox reactors***

   Brendan Bulfin, Barry E. Murphy, Olaf Lübben, Sergey A. Krasnikov, and Igor V. Shvets
   International Journal of Hydrogen Energy **37**(13) (2012) 10028–10035

3. ***Writing with atoms: Oxygen adatoms on the MoO_2/Mo(110) surface***

   Sergey A. Krasnikov, Olaf Lübben, Barry E. Murphy, Sergey I. Bozhko, Alexander N. Chaika, Natalia N. Sergeeva, **Brendan Bulfin**, and Igor V. Shvets
   Nano Research **6** (2013) 929–937

4. ***Manipulating and probing the growth of plasmonic nanoparticle arrays using light***

   Oral Ualibek, Ruggero Verre, **Brendan Bulfin**, Victor Usov, Karsten Fleischer, John F. McGilp and Igor V. Shvets
   Nanoscale **5** (2013) 4923–4930

5. ***An analytical model of CeO_2 oxidation and reduction***

   Brendan Bulfin, Arran J. Lowe, Kevin A. Keogh, Barry E. Murphy, Olaf Lübben, Sergey A. Krasnikov, and Igor V. Shvets
   Journal of Physical Chemistry C **46** (2013) 24129–24137

6. ***Thermodynamics of CeO_2 thermochemical fuel production.***
   Brendan Bulfin, Friedemann Call, Matthias Lange, Olaf Lübben, Christian Sattler, Robert Pitz-Paal, and Igor V. Shvets
   Energy and Fuels, **Accepted January 2015**

Contents

List of Tables

List of Figures

Nomenclature

T	Temperature
P	Pressure
ΔG	Change in Gibbs free energy
ΔH	Change in enthalpy
ΔS	Change in entropy
R	Ideal gas constant
δ	Oxygen stoichiometry
δ_{max}	Maximum δ
$[\mathrm{O_{Ce}}]$	Removable oxygen concentration
$[\mathrm{O_{vac}}]$	Oxygen vacancy concentration
$[\mathrm{O_{gas}}]$	Oxygen gas concentration
$[\mathrm{Ce}]$	Concentration of cerium
n	Oxygen gas power dependency of oxidation
k_a	Rate constant
A_a	Frequency factor
E_a	Activation energy
$P_{\mathrm{O_2}}$	Oxygen partial pressure
D	Diffusion coefficient
r_p	Radius of spherical CeO_2 particle

δ_{r_p}	Boundary vacancy concentration
α	Fraction completed
k	Thermal conductivity
C_p	Specific heat capacity at constant pressure
ρ	Density
$\hat{n}$	Surface normal vector
ϵ	Surface emissivity
σ	Stefan-Boltzmann constant
G	Total incoming radiation
F	View factor
ΔT	$T_{\mathrm{rd}} - T_{\mathrm{ox}}$
$\Delta\delta_{eq}$	Equilibrium yield
$P_{f\mathrm{O}_2}$	Final P_{O_2} during reduction
P_{O_2}	Oxygen partial pressure
ε	Heat exchanger effectiveness
n_i	Moles of component i
x_i	Mole fraction of component i
m_i	Mass of component i
η_i	Efficiency of process i
$R_{\frac{\mathrm{H}_2}{\mathrm{H}_2\mathrm{O}}}$	Equilibrium ratio between H_2 and H_2O in contact with $CeO_{2-\delta}$
C	Solar concentration
Q	A quantity of heat
Q_{rd}	Energy consumed by reduction
Q_{CeO_2}	Energy used to heat ceria

Q_{N_2}	Energy required to produce nitrogen
Q_{gas}	Energy required to heat the sweep gas
Q_{pmp}	Energy required to pump gases
Q_{H_2O}	Energy required to heat oxidiser
Q_{ox}	Energy released by oxidation reaction
Q_{rec}	Recovered heat
t_{cyc}	Time for one full cycle
$\dot{Q}_{out}$	Output power

Common subscripts

ws	Water splitting: $H_2O \longrightarrow H_2 + \frac{\delta}{2}O_2$
ox	Oxidation
rd	Reduction
amb	Ambient
ij or j	Index notation

Abbreviations

CPC	compound parabolic concentrator
CSP	concentrated solar power
DLR	German Aerospace Center
HHV	higher heating value
FEM	finite element method
FWHM	full width at half maximum
UHV	ultra-high vacuum
SEM	scanning electron microscope
TCD	Trinity College Dublin
XRD	X-ray diffraction
XPS	X-ray photoemssion spectroscopy

Chapter 1

Introduction

During the summer months of 2014 climate change made many news headlines, largely due to the publication of a three part report on the subject which provided a review of scientific bases, impacts and vulnerability, and possible mitigation plans [3–5]. The report was commissioned by the United Nations, put together by the Intergovernmental Panel on Climate Change, and was the fifth report of its kind. It is based on some 12000 peer reviewed publications. Although often sensationalised by the media and policy makers, the report presents strong evidence that there will be serious implications for society as a result of climate change. In addition fossil fuels are not an infinite resource and future generations will be faced with the issues of decreasing availability.

In order to combat and reduce the long term damages caused by climate change, and to ensure long term stability, the economy needs to move away from its large reliance on fossil fuels. Scientific efforts aimed at achieving this goal are on-going and widespread. There are many alternative sources of energy including the elusive nuclear fusion, increased scale of global use of nuclear fission and many large scale renewable energy projects. There is also a large reliance on dense liquid based fuels in many industries such as transportation of goods and people. These liquid fuels are for the most part derived from fossil fuels. Many areas of research aim to tackle this, leading to great improvements in electrical energy storage [6], increased interest in the production of synthetic fuels [7], and the proposed hydrogen economy [8].

One method of producing fuel which does not rely on fossil fuels is to utilise either nuclear heat or renewable energy sources to drive reversible endothermic chemical reactions. This introduction gives an overview of the area of solar fuel production with emphasis on thermochemical cycles and in particular the cerium dioxide redox cycle.

1.1 Introduction to solar fuel production

The most well known form of solar fuel production is carbon fixation performed by plants and algae via photosynthesis. Solar energy is utilised to turn carbon dioxide and water into organic compounds, which can be used as fuel. This could be considered the oldest form of solar fuel production, as biological organisms formed via photosynthesis are the basic ingredients for fossil fuel deposits. From this point of view the burning of fossil fuels is essentially using stored up solar energy from the earths ancient geological past. This burning of fuels which were fixated out of the atmosphere in the distant past, reverses the process and releases previously stored carbon as carbon dioxide. In this way climate change can in some ways be compared to turning back the geological clock to a time when the earth was a warmer and wetter place.

This same solar powered carbon fixation by plants and algae is also the basis for most biofuel production. The difference is that biofuel is formed by geologically recent carbon fixation, meaning the input products are grown in the present time. There have been many recent developments in this field [9] and biofuel has already become a practical substitute for fossil fuels in many countries. However the production of biofuel is not environmentally benign [10], and with a growing global population to feed, it is unclear how much cultivatable land could be devoted to biofuel crops.

Another important area of research in recent years has been the production of hydrogen via artificial photosynthesis [11]. This is achieved via photocatalytic water splitting in which light is absorbed by a photo-catalyst, which is a semi-conductor with a large enough band-gap to split water ($>$ 1.23 eV). The generated electron hole pairs can then react at surface sites with water molecules to produce hydrogen and oxygen. This phenomena was first documented by Fujishima and Honda in 1972 using a TiO_2 photo-catalyst [12]. TiO_2 based photo-catalysts only absorb UV which means a low solar to fuel efficiency, but any light with wavelength less than approximately 1000 nm has the required energy. Thus, even with the requirement of a small over-potential, it should be possible to utilise a large part of the visible range. However TiO_2 based catalysts still offer the best performance as other photo-catalysts with lower band gaps are susceptible to photo-corrosion [13].

1.1.1 Water thermolysis

A very direct method of producing solar fuel is to use solar power as a heat input to drive endothermic reactions such as the water splitting reaction. The splitting of water by heating it directly is known as water thermolysis and was investigated as a means of producing hydrogen from solar power as early as the 1970s [14]. This idea offers a conceptually very simple and potentially very efficient method of splitting water to produce hydrogen. The water splitting reaction and the change of the Gibbs free energy are

$$\mathrm{H_2O} \xrightarrow{\text{heat}} \mathrm{H_2} + \frac{1}{2}\mathrm{O_2} \tag{1.1}$$

$$\Delta G_{\mathrm{ws}}(T) = \Delta H_{\mathrm{ws}} - T\Delta S_{\mathrm{ws}}. \tag{1.2}$$

For complete decomposition, ΔG must become negative, which does not occur for temperatures less than 4500 K. In fact the situation is a little more complicated, because at high temperatures, atomic hydrogen, atomic oxygen, and OH molecules, can make up a significant proportion of the mixture. The equilibrium equation which must be considered is

$$\mathrm{H_2O} \rightleftharpoons x_1\mathrm{H_2O} + x_2\mathrm{H_2} + x_3\mathrm{O_2} + x_4\mathrm{H} + x_5\mathrm{O} + x_6\mathrm{OH}. \tag{1.3}$$

Since the Gibbs energies of formation and the enthalpies of formation of all the species at standard temperature and pressure are known, it is possible to iteratively solve the equilibrium composition for higher temperatures [15, 16].

Figure 1.1 shows the mole fraction of each species as a function of temperature, which was calculated using FactSage thermochemical software [17, 18].

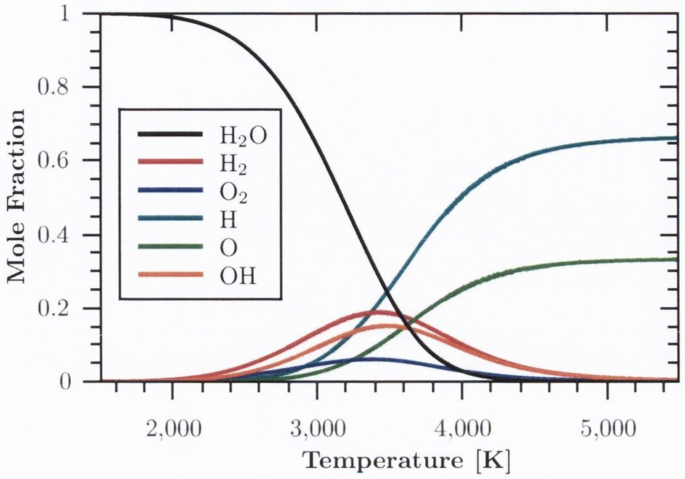

Figure 1.1: Mole fraction of different species in steam vs. the temperature

The mole fraction is the number of moles of a species divided by the total number of moles of all the species present. There is no appreciable decomposition below approximately 2500 K. In addition, when water is split in this way the products form a high temperature mixture of gases which must be separated. Research in this area is often focused on using ceramic membranes (yttria stabilised zirconium) which allow oxygen to pass through, separating it from the high temperature mixture [19, 20].

The high temperature and corrosive atmosphere which any thermolysis reactor must be subject to make the development of this particular technology a difficult task. However it has recieved some attention in recent times with a large project conducted around the turn of the millennium by Kogan *et al.* [15, 19, 21, 22]. More recently it has been the subject of a number of reviews suggesting the technology is still being developed [23, 24].

1.2 Thermochemical Cycles

A more feasible route to water splitting can be achieved via a thermochemical cycle, in which a series of reactions are performed, the sum of which is the water splitting reaction. One or more of the reactions must be endothermic requiring a heat source to drive the reaction.

The concept was first proposed by Funk and Reinstrom [25, 26]. They oversaw a project in the early 1960s called Energy Depot, which was aimed at finding ways of producing fuel from a heat source. The fuels being considered for production were hydrogen and ammonia, and the heat source was to be a small portable nuclear reactor. Fuel availability was not an issue at the time, rather the motivation was to target niche markets such as the production of fuel in remote military battlefields and outposts.

The authors considered a number of multiple step thermochemical cycles. As a bench mark for their investigation they used the already proved method of nuclear electricity generation followed by electrolysis. The results of this study were not promising enough to continue the development of the thermochemical cycles they investigated and this particular project came to an end.

Then during the 1970s there were a number of oil/energy crises which had a strong effect on some of the worlds largest economies such as the US. This alerted people to the fact that fossil fuels were not an unlimited source of energy. In the wake of these crises, thermochemical water splitting began to receive more attention [27, 28], this time for more peaceful reasons such as to reduce reliance upon fossil fuels. The most likely heat source considered to drive the reactions was still nuclear reactors [29].

A number of searches were conducted to compile all of the possible known cycles for evaluation during this period of activity [30, 31]. Activity peaked in the mid 70s with over 100 publications on the subject in 1976. This slowly decreased throughout the early 80s and by 1990 publications had decreased to less than 20 per year [24]. This was largely due to the recovery of the economy and the end of the fuel crisis of the 70s. In addition the enthusiasm of the thermodynamic studies was somewhat dampened by economic studies of the technology, which showed that it was not competitive with other standard methods of producing hydrogen from water (electrolysis) at the time [32].

Today 95% of hydrogen is still produced from fossil fuels by steam reforming or partial oxidation of methane and coal gasification, with the remaining 5% mostly produced by electrolysis [33]. This makes electrolysis powered by renewable sources the most likely near term renewable hydrogen production method and a benchmark in terms of performance.

1.2.1 The Sulphur cycles

A good example of a cycle which was developed during this period is the sulfur-iodine cycle proposed by General Automatic in the 70s [34]. It is a three step cycle with various separation techniques also implied to separate reactants. It contains the following chemical reactions

$$
\begin{aligned}
I_2 + SO_2 + 2H_2O &\xrightarrow{\text{Exothermic}} 2HI + H_2SO_4 && (120\ ^\circ C) && (1.4)\\
2H_2SO_4 &\xrightarrow{\text{Endothermic}} 2SO_2 + 2H_2O + O_2 && (830\ ^\circ C) && (1.5)\\
2HI &\xrightarrow{\text{Endothermic}} I_2 + H_2 && (450\ ^\circ C) && (1.6)
\end{aligned}
$$

where the Eqn. 1.4 is exothermic and Eqn. 1.5 and 1.6 are endothermic. The difference in heat consumed by the endothermic reactions and released by the exothermic reaction is stored in the hydrogen.

A hybrid sulphur cycle was also developed [35], with the reactions

$$
\begin{aligned}
2H_2SO_4 &\xrightarrow{\text{Endothermic}} 2SO_2 + 2H_2O + O_2 && (830\ ^\circ C) && (1.7)\\
SO_2 + 2H_2O &\xrightarrow{\text{Electrolysis}} H_2SO_4 + H_2 && (100\ ^\circ C) && (1.8)
\end{aligned}
$$

where electrolysis is used to reduce the number of steps. The voltage needed for this electrolysis is 0.158 V, compared to 1.223 V for water electrolysis, which greatly reduces the electrical power consumption.

These cycles are still being studied to this day, and in recent years this work has gained momentum. There are currently a number of large scale projects aimed at producing hydrogen on an industrial scale using the sulphur-iodine cycle. One example is a pilot plant which has been constructed and tested by the Japan Atomic Energy Agency, which couples the cycle to a nuclear reactor as a heat source [36]. There have also been investigations into coupling either the sulphur-iodine or the hybrid sulphur cycle with large scale concentrated solar power plants [37], using the concentrated solar power directly as a heat input. These developments could see these sulphur cycles become an economically competitive method of producing hydrogen for industrial purposes and potentially as a fuel.

1.3 Two-step metal-oxide redox cycles

Since approximately the year 2000 there has been a revival of interest in the thermochemical route of producing hydrogen. This can be explained by mounting pressure in many countries to reduce the consumption of fossil fuels, as well as developments in the area of concentrated solar power [38, 39]. With the development of parabolic dish and solar tower receiver systems, very high solar concentrations of up to 5000 times the ambient solar concentration can be obtained. This means that much higher temperatures are available than previously considered when using nuclear power as a heat source. This caused the area of thermochemical cycles to diversify with more emphasis on two step metal-oxide redox cycles which require higher temperature than other multi-step or hybrid cycles [40, 41]. Although two-step metal-oxide cycles require higher temperatures the energy efficiency has the potential to be higher than multi-step cycles.

The basic reactions are

$$\mathrm{MO}_x \xrightarrow{\text{Endothermic}} \mathrm{MO}_{x-\delta} + \frac{\delta}{2}\mathrm{O}_2 \quad \text{Reduction - } \quad T_{\mathrm{rd}} \qquad (1.9)$$

$$\mathrm{MO}_{x-\delta} + \delta\mathrm{H}_2\mathrm{O} \xrightarrow{\text{Exothermic}} \mathrm{MO}_x + \delta\mathrm{H}_2 \quad \text{Oxidation - } \quad T_{\mathrm{ox}} \qquad (1.10)$$

where the metal oxide is reduced at high temperature T_{rd}, consuming heat, and then oxidised in steam at a lower temperature T_{ox}, releasing heat. The sum of the two reactions is the water splitting reaction given in Eqn. 1.2. For most metal oxides the reduced oxide can also be used to split carbon dioxide, which is discussed in more detail in Section 1.4.

These two step cycles can be described with a simple analogy to the standard thermodynamic heat engine. We have a quantity of heat supplied to the cycle at high temperature T_{rd} and some fraction of this heat is released at lower temperature T_{ox}. The difference in heat is stored as chemical energy in the hydrogen, instead of being released as work. A schematic of this idea is shown in Fig. 1.2. The metal oxide is simply recycled within the system and is not consumed.

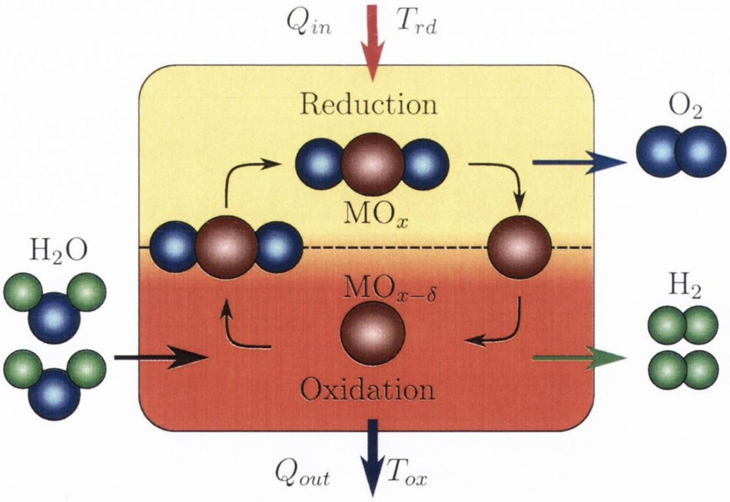

Figure 1.2: A schematic of a two step cycle showing the recycling of the metal oxide within the cycle.

The thermodynamic efficiency can be defined in a similar way to that of a heat engine. Instead of the work output divided by the heat input we have the higher heating value of the fuel divided by the heat input.

$$\eta = \frac{W}{Q_{in}} \quad \longrightarrow \quad \eta = \frac{\mathrm{HHV}_{\mathrm{H_2}}}{Q_{in}} \tag{1.11}$$

For the oxidation step to proceed the metal oxygen bond energy must be greater than that of the water molecule, and so $Q_{in} > \mathrm{HHV}_{\mathrm{H_2}}$ and $0 < \eta < 1$.

Some basic thermodynamic restrictions on these cycles can be understood by considering the fact that the two reactions must sum to water splitting. Therefore at any given temperature the change in Gibbs free energy for the reduction and oxidation reactions must sum to that of water splitting.

$$\Delta G_{\mathrm{ws}} = \Delta G_{\mathrm{rd}} + \Delta G_{ox} \tag{1.12}$$

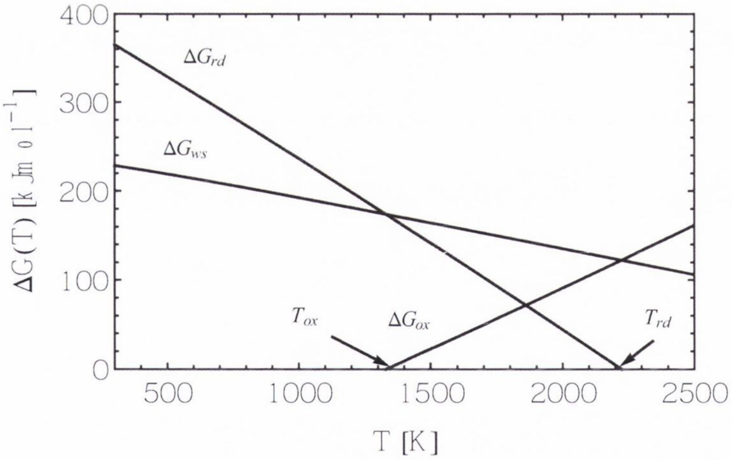

Figure 1.3: The change in Gibbs free energy for water splitting and an example two-step thermochemical cycle showing the additive nature of the change in Gibbs free energies

Figure 1.3 shows $\Delta G_{\mathrm{ws}}(T)$ as well as a hypothetical $\Delta G_{\mathrm{rd}}(T)$ and $\Delta G_{ox}(T)$. It can be seen that at a given temperature the change in Gibbs energy for the reduction and oxidation reactions satisfy Eqn. 1.12. Where the lines cut the y-axis is approximately the change in enthalpy and the slope is the change in entropy for the reactions. We can see from this diagram why reduction takes place at high temperature and the oxidation at lower temperature as ΔG must be less than zero for the reactions to become spontaneous.

In addition the reduction must have a greater change in enthalpy than water-splitting, meaning that the oxide must have a stronger bond with oxygen than the water molecule in order to take the oxygen from the water molecule. This can be seen in Fig. 1.3 as the reduction reaction has a higher intercept with the y-axis than water splitting, which corresponds roughly to their change in enthalpy. The reduction must also have a greater change in entropy than the water splitting reaction so that the reaction becomes spontaneous at lower temperatures. This can also be seen in Fig. 1.3 by the steeper slope of the reduction reaction compared to that of water splitting.

Many metal oxides have been considered for these cycles. A list of the main cycles was compiled from the literature by Abanades *et al.* [42]. Here we briefly discuss the cycles which have received the most interest and, which demonstrate the main characteristics of two-step thermochemical water splitting.

1.3.1 Ferrites

The first and the most extensively studied of the two step cycles was proposed by Nakamura in 1977 [43]. Nakamura compared the iron oxide thermochemical cycle to direct water thermolysis. The reaction equations are

$$\mathrm{Fe_3O_4}(s) \longrightarrow 3\mathrm{FeO}(l) + \frac{1}{2}\mathrm{O_2}(g) \qquad (2200\,^{\circ}C) \qquad (1.13)$$

$$3\mathrm{FeO}(s) + \mathrm{H_2O}(g) \longrightarrow \mathrm{Fe_3O_4}(s) + \mathrm{H_2}(g) \qquad (700\,^{\circ}C) \qquad (1.14)$$

where the letter in brackets after each species refers to the phase; solid, liquid or gaseous.

This cycle requires a large temperature swing between the two steps, and after reduction the reduced oxide and oxygen are in different phases so there is no need for separation techniques [44, 45]. The solar reduction step was investigated in a solar furnace by Sibieude *et al.* [46]. They found that full decomposition was obtained in an argon atmosphere and 40 % decomposition in an air atmosphere at 2200 °C.

Alternative cycle materials based on mixed iron oxides of the form $\mathrm{M}_x\mathrm{Fe}_{3-x}\mathrm{O}_4$ (M = Mn, Mg, Co, Zn, Ni) have been extensively investigated [45, 47, 48]. The idea is to reduce the reduction temperature of the ferrites, but still maintain a good hydrogen yield during the oxidation step. A thermodynamic study was recently performed by Allendorf *et al.* [49], and there have been many experimental investigations of mixed ferrites [50–55]. They show that dopants such as Mn, Co and Ni can improve the extent of reduction at lower temperatures.

The effects of supporting the mixed ferrites on more stable oxides such as $\mathrm{ZrO_2}$ to reduce sintering during reduction have been studied by Kodama *et al.* [56, 57]. The idea is to partially reduce the ferrite at lower temperature while it is supported with a more stable oxide. This way the ferrite remains in the solid phase, reducing the complexity of the reactor needed.

Prototype reactors

Thermodynamic studies by Driver *et al.* showed that the fuel production efficiencies for ferrite cycles have a maximum of 36 % without heat recuperation and could be as high as 78 % with heat recuperation [58]. The same group at Sandia National Laboratories have proposed and tested a solar powered reactor based on mixed ferrite materials [58–61]. The reactor uses mixed ferrites supported on counter rotating rings which pass through reduction and oxidation zones allowing for continuous operation and heat recuperation. A schematic of the proposed design is shown in Fig. 1.4. Efficiencies of this design in practice have so far been low ($<$ 2 %) and the reactor design complexity is rather high due to the counter rotating rings concept.

A circulating fluidised bed reactor has been proposed and tested at the laboratory scale by Kodama *et al.* [62–64], which used $NiFe_2O_4$ particles as the redox material. The $NiFe_2O_4$ was supported on ZrO_2 and cycled between 1000 - 1500 °C. The reduction was performed in an inert nitrogen atmosphere. The reactor is designed to be used with a beam down solar concentrator. A schematic of the proposed design is shown in Fig. 1.5. The input gas stream drives the circulation of the particles. The input stream is changed to H_2O for oxidation. This prototype was thus operated in batch mode with reduction and oxidation taking place alternately. They observed that approximately 44 % of the ferrite material was reduced and then fully re-oxidised using steam. This concept is promising, as with some design modification using a fluidised

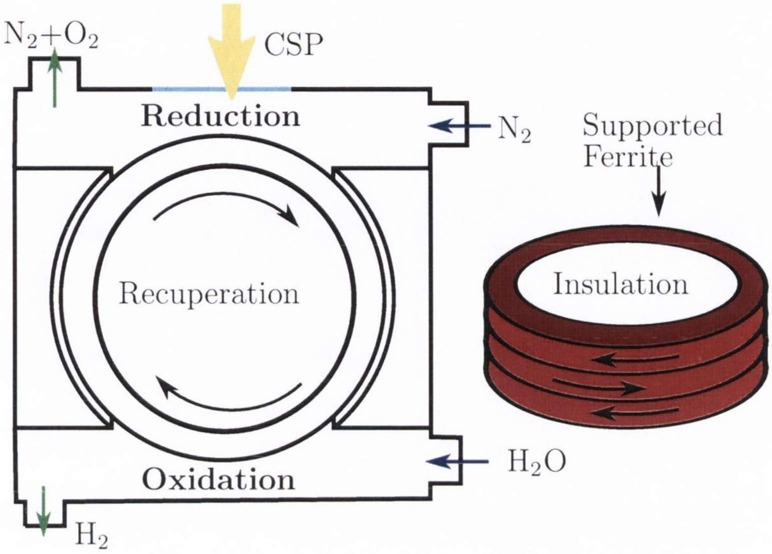

Figure 1.4: A schematic showing the design proposed by Sandia National Laboratories, with a plan of the reactor and the counter rotating rings used for heat recuperation.

bed could conceivably allow for continuous operation and heat recuperation with lower design complexity than the reactor proposed by Sandia National Laboratories.

A semi batch process reactor using mixed ferrites has been developed as part of the HYDROSOL project run by the German Aerospace Centre (DLR) [65, 66]. In this reactor honeycomb monoliths coated with the reactive ferrite are first heated for reduction, then at lower temperature oxidised with steam. A 100 kW pilot plant was tested at the Plataforma Solar de Almeria, in which two reactor zones were alternatively switched between oxidation and reduction to obtain continuous hydrogen production [67]. This reactor concept offers a very simple fixed bed design which was successfully tested and is still under development by Sattler *et al.* [68, 69].

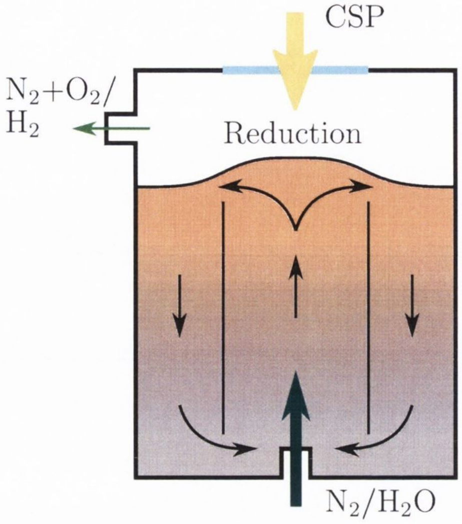

Figure 1.5: A schematic showing the design proposed by Kodama *et al.*. The black arrows show the circulation of the supported ferrite.

1.3.2 Volatile oxides

In terms of thermodynamics, volatile oxides may offer the most efficient thermochemical cycles for water splitting. The decomposition involves sublimation of the oxide into a gaseous metal and oxygen [70, 71]. Compared to the ferrite cycle where the oxide remains solid or liquid this offers a larger change in entropy, ΔS. In Fig. 1.3 this would give us a relatively sharper decrease in $\Delta G_{\mathrm{rd}}(T)$, which should allow reduction to spontaneously proceed at lower temperatures. However there is a level of complexity added, because the gaseous mixture formed during reduction must be separated.

Zinc oxide

The zinc oxide cycle has received the most attention amongst the volatile oxides.

$$\mathrm{ZnO}(s) \longrightarrow \mathrm{Zn}(g) + \frac{1}{2}\mathrm{O_2}(g) \qquad (2000\ ^{\circ}C) \qquad (1.15)$$

$$\mathrm{Zn}(l) + \mathrm{H_2O}(g) \longrightarrow \mathrm{ZnO}(s) + \mathrm{H_2}(g) \qquad (800\ ^{\circ}C) \qquad (1.16)$$

A large amount of research on this particular cycle was conducted by Steinfeld *et al.* at ETH Zurich [72–74]. A reactor for the solar reduction of ZnO was developed and tested by the same group [75, 76]. In the reactor ZnO particles are fed into an insulated rotating cavity. The rotation creates a centrifugal force which keeps the ZnO particles stuck to the outside walls. In this way the ZnO is directly heated by concentrated solar power and in addition forms an insulator to protect the walls.

An argon gas flow is used to remove the products from the reactor and to keep the reactor aperture glass free of ZnO. The product stream must then be quenched in order to prevent recombination. The quenching was achieved by passing the stream onto a water cooled wall which rapidly cools the mixture to below the melting point of zinc (410 °C) [77]. This quenching prevents heat recovery, but even without heat recovery the efficiency could be as high as 29 % [78].

Tin oxide

Abanades *et al.* recently proposed a cycle in which tin oxide is partially reduced at reasonably low temperatures [79].

$$\mathrm{SnO_2}(s) \longrightarrow \mathrm{SnO}(g) + \frac{1}{2}\mathrm{O_2}(g) \qquad (1600\ °C) \qquad (1.17)$$

$$\mathrm{SnO}(s) + \mathrm{H_2}O(g) \longrightarrow \mathrm{SnO_2}(s) + \mathrm{H_2}(g) \qquad (600\ °C) \qquad (1.18)$$

Similar to the zinc oxide cycle the reduction product stream must be quenched in order to separate the oxygen and reduced tin oxide. However, the melting point of SnO (1080 °C) is much higher than that of zinc and thus potentially less heat is lost in quenching. In addition the quenching is easier as the condensation of SnO starts at approximately 1500 °C.

The oxidation reaction for SnO proceeds slower than that of zinc [80]. This is due to the fact that the change in enthalpy for the reduction of $\mathrm{SnO_2}$ ($-296\,\mathrm{kJ\,mol^{-1}}$) is quite close to that of water splitting ($-241\,\mathrm{kJ\,mol^{-1}}$). This is one of the reasons why the reduction reaction proceeds at such low temperatures. The driving force for the reaction is a change in enthalpy of $55\,\mathrm{kJ\,mol^{-1}}$. In order to increase the rate we must increase the temperature, and from Fig. 1.3 we see that this increases $\Delta G(T)$ for the oxidation making the reaction less favorable. If the cycle is used to split $\mathrm{CO_2}$ instead, the difference in the enthalpy change is lower ($23\,\mathrm{kJ\,mol^{-1}}$) and the oxidation reaction is even less favorable [81]. However, given the ease of reduction for this oxide the slower reaction kinetics of oxidation may be an acceptable drawback and the cycle does merit further study. Alternatively the SnO could itself be used as a fuel to generate heat or as a heat storage medium for off sunlight power generation in concentrated solar power plants.

1.4 Cerium Dioxide

The focus of this thesis is the cerium dioxide redox cycle, which as we shall see has a number of benefits over other metal oxide cycles. In addition to fuel production cerium dioxide (ceria) has found many applications due to its unique properties. At high temperatures it is an oxygen ion conductor and is also noted for its oxygen storage and redox properties [82–84]. This makes it a good material for applications in catalysis and solid oxide fuel cells [85–88]. Ceria has found far-reaching applications in catalysis where it is used in automotive catalysts, oxidation catalysts and reforming catalysts.

The application of the ceria redox cycle for splitting water was first studied by Otsuka *et al.* in 1985 [89]. They performed kinetic studies of the oxidation of reduced ceria ($CeO_{1.8}$) in a steam atmosphere, producing H_2. They found that reduced ceria could easily be oxidised in a steam atmosphere and they concluded that the kinetics were not limited by water absorption on the surface or by diffusion in the bulk.

The cycle was first demonstrated by Abanades *et al.* using a solar reactor to reduce the ceria [90]. The cycle reactions are

$$\begin{aligned} 2\mathrm{CeO_2}(s) &\longrightarrow \mathrm{Ce_2O_3}(l) + \frac{1}{2}\mathrm{O_2}(g) && (2000\ ^\circ C) && (1.19) \\ \mathrm{Ce_2O_3}(s) + \mathrm{H_2O}(g) &\longrightarrow 2\mathrm{CeO_2}(s) + \mathrm{H_2}(g) && (800\ ^\circ C). && (1.20) \end{aligned}$$

In these experiments the reduction was performed at a reduced pressure of 100–200 mbar, which by Le Chatliers principle will favour reduction. The reduced oxide was then cooled to room temperature and later the oxidation in a steam atmosphere was tested. The oxidation was seen to proceed rapidly. The authors conclude that the cycle is technically feasible and warrants further study. The temperature for reduction is still very high and offers high technical demands in terms of reactor engineering.

1.4.1 Partial reduction

Ceria can be partially reduced at lower temperatures in atmospheres of low oxygen partial pressure. The extent of the reduction δ, depends on the temperature and the oxygen partial pressure [91].

$$\mathrm{CeO_2} \xrightarrow{\text{heat} = \Delta H_{\mathrm{rd}}} \mathrm{CeO_{2-\delta}} + \frac{\delta}{2}\mathrm{O_2} \tag{1.21}$$

The reduced oxide can be used to split both H_2O and CO_2 producing H_2 and CO respectively [92, 93].

$$\mathrm{CeO_{2-\delta}} + \delta \mathrm{H_2}O \longrightarrow \mathrm{CeO_2} + \delta \mathrm{H_2} \tag{1.22}$$

$$\mathrm{CeO_{2-\delta}} + \delta \mathrm{CO_2} \longrightarrow \mathrm{CeO_2} + \delta CO \tag{1.23}$$

Ceria is unique in that this reduction does not change the phase. During reduction at temperatures lower than its melting point ($< 2000\,°\mathrm{C}$), ceria remains in the fluorite phase, which is shown if Fig. 1.6, up to a non-stoichiometry of approximately $\delta = 0.35$ [94–96]. This is a remarkable ma-

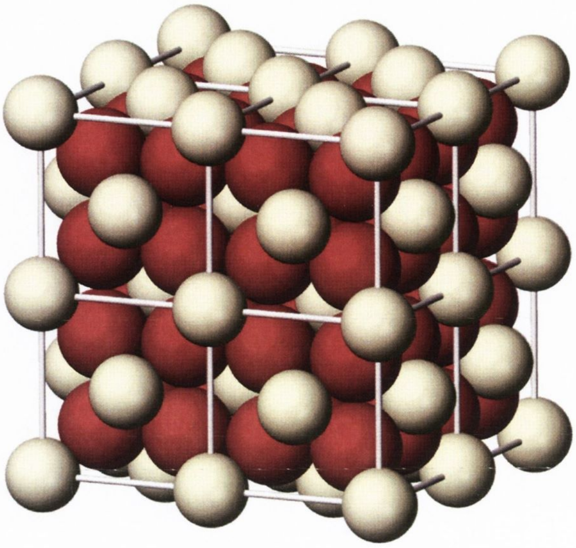

Figure 1.6: A schematic showing the flourite crystal structure of ceria where the oxygen molecules are white and the cerium red.

terial property, in that removing more than 15 % of the oxygen from the crystal lattice does not change the crystal structure. This also makes ceria reduction a very technically simple process, as there is no additional phase changes consuming heat or complicating the reduction process.

The products, CO and H_2 form syn-gas, which can be converted into denser diesel-type fuel using the Fischer-Tropsch process [97, 98]. If the reduction is driven by concentrated solar power this process could allow the production of renewable dense liquid fuels. In Fig. 1.7 we see a schematic showing the cycle with its inputs and products.

A thermodynamic bound on the efficiency of the ceria redox cycle, similar to the Carnot efficiency for heat engines, can be obtained using Eqn. 1.11 and setting $Q_{in} = \Delta H_{\text{rd}}$. The change in enthalpy of the reduction is a function of δ [91], so the average value over the range $\delta = 0$ to 0.1 is taken, which

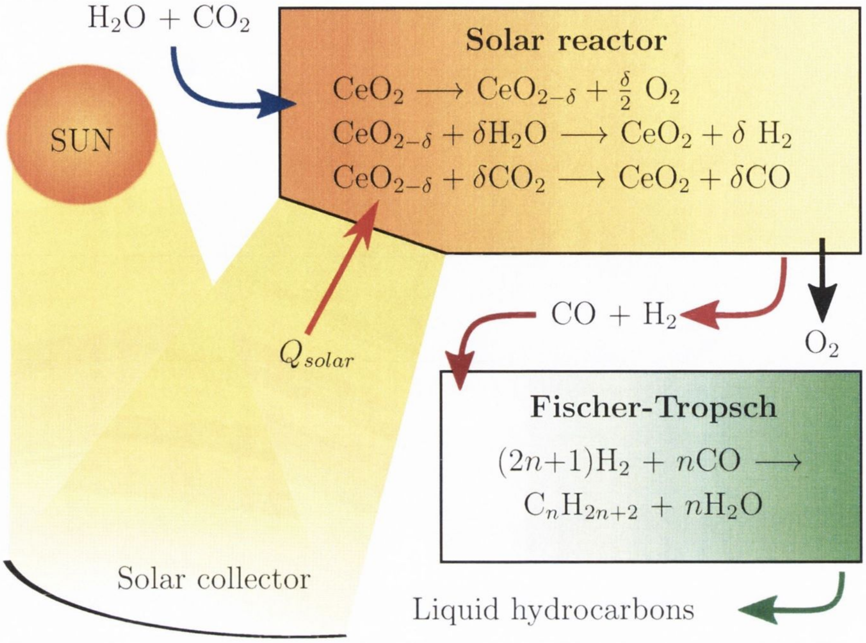

Figure 1.7: A schematic showing the conversion of H_2O and CO_2 into liquid hydrocarbons using solar power to drive the ceria redox cycle followed by the conversion of syn-gas to liquid hydrocarbons via the Fischer-Tropsch process.

gives $\Delta H_{\mathrm{rd}} = 430\,\mathrm{kJ\,mol^{-1}}$. Now simply using the higher heating values of H_2 ($286\,\mathrm{kJ\,mol^{-1}}$) and CO ($283\,\mathrm{kJ\,mol^{-1}}$), the maximum thermodynamic efficiency for water splitting and carbon dioxide splitting were calculated to be

$$\eta_{\mathrm{ws}} = 67\% \tag{1.24}$$

$$\eta_{cs} = 66\%. \tag{1.25}$$

In addition the oxidation can proceed at high temperatures ($> 1000\,^{\circ}\mathrm{C}$) [99], and thus the waste heat from the cycle can still be used as high temperature process heat to perform work.

1.4.2 Proof of concept reactors

The reactor concepts which were discussed for ferrites could also be utilised for the ceria redox cycle. Ceria could be used without supports in the counter rotating ring reactor shown in Fig. 1.4. In addition ceria particles could be used without supporting zirconia particles in the fluidised bed reactor shown in Fig. 1.5. Ceria is more stable than ferrites, especially when doped as we shall see later.

Tamaura *et al.* at the Tokyo Institute of Technology built a test reactor which was tested with both CeO_2 and $NiFe_2O_4$ [100, 101]. The reactor was very similar in design to the reactor developed by Sandia National Laboratories, which is shown in Fig. 1.4. However there was no counter rotating rings for solid state heat recuperation. The reactor is more simple in that it just features a large rotating drum (500 mm diameter) with the cycled oxide on the outside. The oxide passes through reduction and oxidation zones allowing for continuous fuel production.

Chueh *et al.* constructed a small scale cavity type reactor for testing the potential of ceria for thermochemical fuel production [102]. A schematic of their design is shown in Fig. 1.8. The ceria itself was formed into porous monoliths which lined the interior of the cavity. For reduction the reactor interior was heated to 1600 °C and a sweep gas passed through to remove the oxygen. The reactor is then switched to oxidation by cooling it down to 1000 °C and passing CO_2 through the monolith as shown in the schematic. They completed 500 cycles showing that ceria could be used for fixed bed reactors without supporting materials.

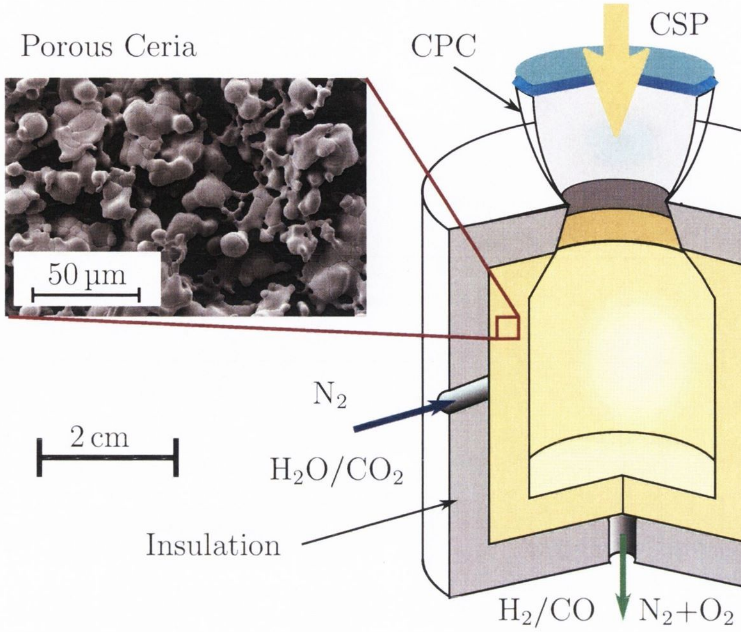

Figure 1.8: A schematic showing the design of the prototype tested by Chueh *et al.*.

A cavity reactor is a standard idea for high temperature solar applications. Concentrated solar radiation is focused onto a compound parabolic concentrator (CPC), which further concentrates the beam through an aperture. The emerging concentrated solar radiation is diverging after passing through the CPC, and is incident onto a hollow cavity. The cavity is insulated on the outside. At high temperatures the radiative heat transfer becomes significant, and the amount of radiated heat is proportional to the radiating surface area. The cavity re-radiates as if the radiating area were only that of the aperture. This means a very concentrated beam focused through a small aperture and onto a relatively large amount of material, results in lower radiation losses per unit of material heated.

The same reactor design seen in Fig. 1.8 was used by Furler *et al.* to simultaneously split H_2O and CO_2 producing syn-gas [93]. They successfully tuned the ratio of H_2 to CO produced, by changing the input ratio of H_2O and CO_2. This is important as this ratio is one of the factors which determines the fuel consistency, and it must be optimised. The syn-gas produced by this method is also pure which means that contaminants such as sulphur, which are common in other syn-gas production methods, do not need to be removed.

1.4.3 Doping ceria to improve redox properties

Similar to the case of ferrites, dopants can be added to ceria to improve its redox properties. The main goals of doping ceria are to improve its high temperature stability and to increase the hydrogen and carbon monoxide yields of the ceria fuel production cycle.

By replacing some of the cerium atoms in the fluorite crystal structure with other cationic metals, the redox properties of ceria can be modified. For example, doping with metals which have a lower valence than Ce^{4+}, such as Sm^{3+}, introduces oxygen vacancies into the fluorite structure, which increases the oxygen ion mobility [103, 104]. The increased mobility may improve the reaction kinetics, but it can also reduce the overall oxygen yield [105, 106].

Doping ceria with ions which have the same valence, but lower ionic radius, such as Zr^{4+} and Hf^{4+}, can increase the reducibility [106–110]. This is very important as it can increase the overall yield of the cycles. Cerium has a very accommodating lattice for these dopants allowing up to 40 % of the ceria ions to be replaced and still maintaining the fluorite structure [111].

For maximum fuel production yield there is an optimum dopant concentration for Zr which was determined via thermogravimetric analysis to be $Ce_{0.85}Zr_{0.15}O_2$ by Call *et al.* [112]. At this optimal Zr concentration, the hydrogen production yield is approximately double that of pure ceria and for higher Zr concentrations the fuel production yield was seen to begin decreasing.

Tamaura *et al.* investigated a number of dopants and similarly found that Zr doubled the yield, but also that Hf dopants could increase the fuel production yield by a factor of approximately 2.2 [106]. They attribute the improvement to the fact that Hf has the same valence as Zr, but also has an even smaller ionic radius [106]. This could only have a very small effect as Hf(85 pm) has approximately the same ionic radius as Zr(86 pm) when compared to Ce(101).

Chapter 2

Analytical model of CeO_2 oxidation and reduction

In this chapter an Arrhenius-based model for the high temperature reduction and oxidation of CeO_2 is developed. The model is shown to agree well with both literature data for the equilibrium oxygen vacancy concentration and novel experimental kinetics of oxidation and reduction obtained as part of the research for this phd thesis.

The form of the Arrhenius rate equation was determined from the properties of the reaction. Equilibrium data from the literature was analyzed with respect to our rate equation. From this analysis a number of constraints on the model parameters were determined and some of the constants of the model were fixed. The model accurately predicts the equilibrium composition of CeO_2 over a wide range of oxygen partial pressures (10^{3}–10^{-4} Pa) and temperatures (1000-1900 °C).

Novel results of the experimental re-oxidation of ceria were analyzed in order to fix the remainder of the constants. Porous cerium dioxide pellets were reduced at high temperature (1600 °C) and low oxygen partial pressure (1 Pa). The reduced cerium pellets were then re-oxidised in an oxygen atmosphere of 14 Pa at temperatures in the range 500-1000 °C. The re-oxidation was conducted in a sealed vacuum chamber. The reaction was monitored via the change in pressure and gas composition measured by a manometer and mass spectrometer. The results from this re-oxidation experiment allowed us to fix the values of the activation energies and frequency factors of the oxidation and reduction. The model was then compared to experimental reaction kinetics of thermal oxidation and reduction and showed good agreement. Finally the model was coupled to heat flow simulations to demonstrate its use.

2.1 Introduction

In the past, studies have been conducted into developing numerical models of the phase diagrams and composition of CeO_2 over a wide range of conditions [95, 113, 114]. These models however give us no information about the reaction kinetics of the reduction and oxidation of ceria. It is interesting to note that ceria remains in the fluorite phase throughout the range of temperatures and pressures of interest for these fuel conversion cycles [92, 95]. Even with large numbers of oxygen vacancies, the fluorite phase is still stable. The fact that no phase changes occur should allow the development of a reasonably simple model of the reactions.

The lack of such a simple analytical model for the reaction kinetics of ceria reduction makes assessment of the performance of ceria reduction difficult. If one has a simple model which only depends on the concentrations of the reactants, the temperature and the oxygen partial pressure, it can easily be linked to heat flow and diffusion simulations [96]. This will greatly improve reactor design capabilities, and allow for more accurate assessment of this proposed fuel production technology.

In this chapter an analytical model for the reduction and oxidation of ceria in an oxygen atmosphere is developed. The model should predict both the equilibrium composition and reaction kinetics if it is to accurately simulate the performance of the reactions. It should prove to be an invaluable tool in the development of the discussed fuel production technology. It could also be of use in any cerium dioxide high temperature redox processes. The model itself is of theoretical interest as it should allow for a better understanding of the role of diffusion and surface reactions in ceria reduction and oxidation.

2.2 Model

The system is modeled as an equilibrium reaction with Arrhenius rate constants [115]. The equilibrium reaction is

$$CeO_2 \rightleftharpoons CeO_{2-\delta} + \frac{\delta}{2}O_2. \tag{2.1}$$

The reaction does not proceed to complete decomposition in this regime. If enough oxygen is removed, the fluorite phase will no longer be stable and a phase transition will be inevitable. If there is a phase change the fundamental properties of the reaction kinetics will change and our equation will no longer be valid. Therefore it is assumed that not all of the oxygen can be removed by this reaction and that it is proceeding towards a certain maximum value of δ, say δ_{max}, with the complete reaction

$$CeO_2 \longrightarrow CeO_{2-\delta_{\mathrm{max}}} + \frac{\delta_{\mathrm{max}}}{2} O_2. \tag{2.2}$$

The reduction reaction depends on the concentration of removable oxygen and the oxidation reaction depends on the concentration of vacancies and the concentration of oxygen gas. Initially, oxygen diffusion in the bulk shall be ignored and the vacancy concentration is assumed to be constant throughout. The rate of change of the oxygen vacancy concentration is the rate at which oxygen leaves CeO$_2$ (reduction) minus the rate at which it recombines (oxidation). This can be formulated as

$$\frac{d[\mathrm{O_{vac}}]}{dt} = [\mathrm{O_{Ce}}]k_{\mathrm{rd}} - [\mathrm{O_{vac}}][\mathrm{O_{gas}}]^n k_{\mathrm{ox}}; \tag{2.3}$$

where k_{rd} and k_{ox} are the rate constants of reduction and oxidation, and $[\mathrm{O_{Ce}}]$, $[\mathrm{O_{vac}}]$ and $[\mathrm{O_{gas}}]$ are the concentrations of removable oxygen in the ceria, oxygen vacancies in the ceria and the oxygen gas concentration. These concentrations will be explicitly defined later. For simplicity it is assumed that the rate constants have a basic Arrhenius temperature dependence and they are given by

$$k_a = A_a \exp\left(\frac{-E_a}{RT}\right). \tag{2.4}$$

The concentration terms can be made unit-less by dividing Eqn. 2.3 by the concentration of cerium [Ce], giving

$$\frac{1}{[\mathrm{Ce}]}\frac{d[\mathrm{O_{vac}}]}{dt} = \frac{[\mathrm{O_{Ce}}]}{[\mathrm{Ce}]}k_{\mathrm{rd}} - \frac{[\mathrm{O_{vac}}]}{[\mathrm{Ce}]}[\mathrm{O_{gas}}]^n k_{\mathrm{ox}}. \tag{2.5}$$

The rate is now in terms of moles of oxygen vacancies per mole of cerium per second, or simply per second. From Eqn. 2.1 and 2.2 the values $\frac{[\mathrm{O_{Ce}}]}{[Ce]}$ and $\frac{[\mathrm{O_{vac}}]}{[\mathrm{Ce}]}$, can be defined in terms of the stoichiometry parameters, δ and δ_{max}.

$$\frac{[\mathrm{O_{Ce}}]}{[\mathrm{Ce}]} = \delta_{\mathrm{max}} - \delta \tag{2.6}$$

$$\frac{[\mathrm{O_{vac}}]}{[\mathrm{Ce}]} = \delta \tag{2.7}$$

The oxygen gas concentration is directly proportional to the oxygen partial pressure $P_{\mathrm{O_2}}$. Therefore the constant of proportionality can simply be included as part of the rate constant $\mathrm{k_{ox}}$, and the oxygen gas concentration is taken to be the oxygen partial pressure. Initially we wish to look at equilibrium data so we set the rate to zero. Setting Eqn. 2.5 equal to zero and using Eqn. 2.4, 2.6 and 2.7 we get the equilibrium condition

$$(\delta_{\mathrm{max}} - \delta)A_{\mathrm{rd}} \exp\left(\frac{-E_{\mathrm{rd}}}{RT}\right) - \delta P_{O_2}^n A_{\mathrm{ox}} \exp\left(\frac{-E_{\mathrm{ox}}}{RT}\right) = 0, \tag{2.8}$$

shown schematically in Fig. 2.1.

At equilibrium the rate of oxidation is equal to the rate of reduction. The equilibrium oxygen vacancy concentration can now be expressed as a

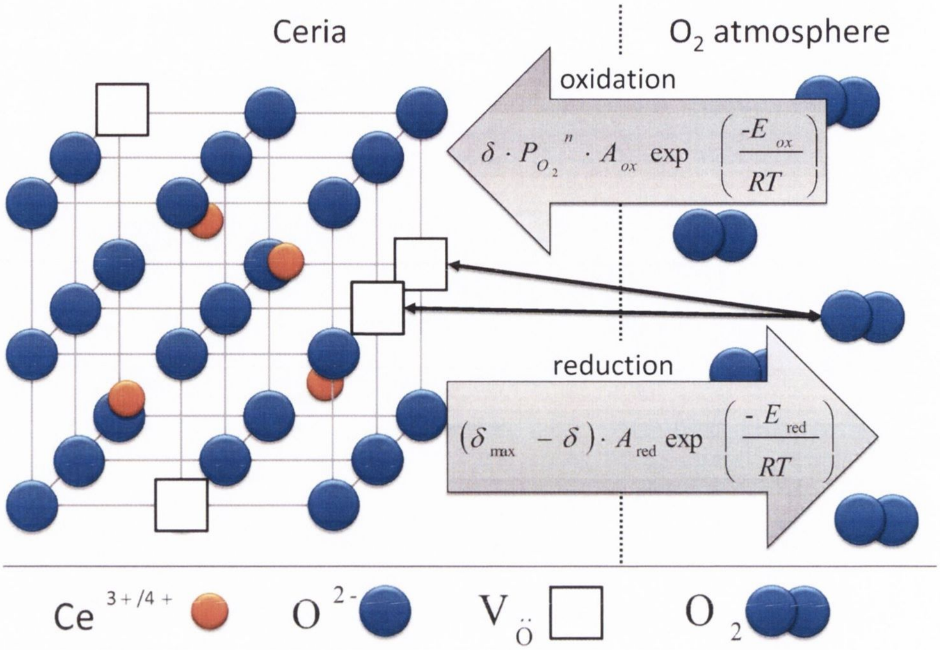

Figure 2.1: A schematic showing the equilibrium nature of the reduction and oxidation reactions.

function of temperature and oxygen partial pressure with the equation

$$\left(\frac{\delta}{\delta_{\text{max}} - \delta}\right) = \frac{A_{\text{rd}}}{A_{\text{ox}}} P_{O_2}^{-n} \exp\left(\frac{-(E_{\text{rd}} - E_{\text{ox}})}{RT}\right). \tag{2.9}$$

The difference in activation energies E_{rd}-E_{ox} is labeled ΔE for the remainder of the chapter.

2.2.1 Equilibrium Composition

It is common in the literature for equilibrium data obtained at constant temperature and varied pressure to plot $\log(\delta)$ vs. $\log(P_{O_2})$. If the logarithm of Eqn. 2.9 is taken, it is clear that a more suitable plot can be made from the equation

$$\log\left(\frac{\delta}{\delta_{\max}-\delta}\right) = -n\log(P_{O_2}) + \log\left(\frac{A_{\mathrm{rd}}}{A_{\mathrm{ox}}}\exp\left(\frac{-\Delta E}{RT}\right).\right) \qquad (2.10)$$

From Eqn. 2.10 it is clear that a plot of $\log(\delta)$ vs. $\log(P_{O_2})$ will yield a straight line with slope $-n$, but only when $\delta << \delta_{\max}$. Supporting this, both Panlener and Dawicke [91, 116] found that in the region $0.001 < \delta < 0.004$, this plot yields a straight line, and the pressure dependence was well characterised by the relation $\delta \propto P_{\mathrm{O}_2}^{-\frac{1}{5}}$.

As we are not dealing with a dilute species reaction it may not be possible to use the law of mass action to accurately predict $\delta_{\max}$ and n. It can however provide a good starting point. From Eqn. 2.2, the law of mass action predicts that $n = \frac{\delta_{\max}}{2}$. Using the findings of Panlener *et al.* as an estimate gives $n = 0.2$, and thus a good starting point would be to set $\delta_{\max} = 0.4$. Using these parameters, experimental equilibrium data can be analyzed. Data in the range 1000 °C - 1500 °C was extracted from the experimental work of Panlener *et al.* [91]. For temperatures above this, the numerical model of Zinkevich *et al.* [95] was used, which is in good agreement with experimental findings [91, 116–119]. We look at pressures in the range of 10^{-4}–10^{3} Pa.

The analysis of data from the literature is presented in Fig. 2.2, with the parameter $\delta_{\max} = 0.35$. For constant temperature, the data show linear dependencies over a wide range of pressures. This is in contrast to the plots made previously of $\log(\delta)$ vs. $\log(P_{O_2})$ [91], where the data begins to deviate from the linear dependence as δ increases and drastically so for values of δ

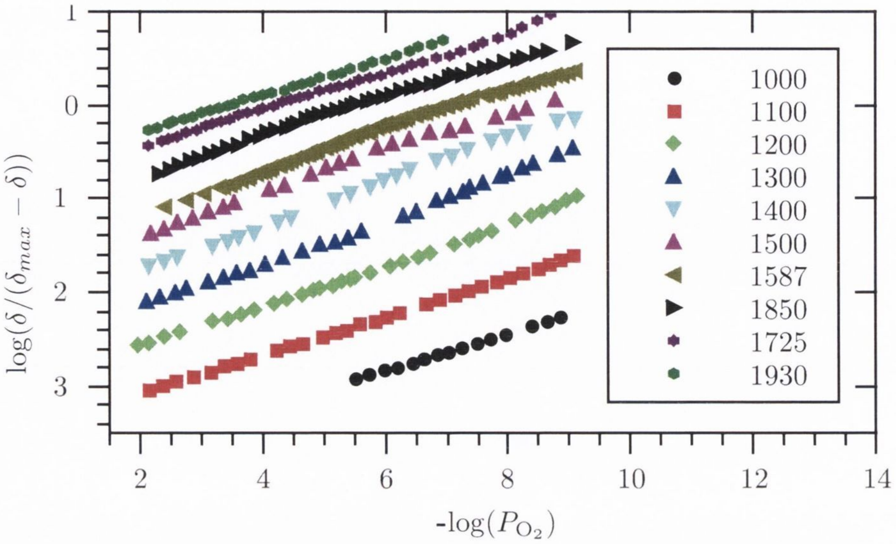

Figure 2.2: Isothermal plots of $\log(\frac{\delta}{\delta_{\text{max}}-\delta})$ vs. -$\log(P_{O_2})$ with the value of $\delta_{\text{max}} = 0.35$. The temperatures plotted are from bottom to top 1000, 1100, 1200, 1300, 1400, 1500, 1587, 1725, 1850, and 1930 °C. The data is taken from Panlener *et al.* [91] and Zinkevich *et al.* [95].

greater than 0.1. This is as predicted by Eqn. 2.8, providing strong evidence in support of this analytical model.

In order to determine the best value of δ_{max}, the data was plotted for a range of different values of δ_{max}. The plots were then fit linearly and the variation in slope and the R^2 regression value of each set of data was compared.

The dependency of slope on the temperature is plotted in Fig. 2.3. For simplicity we want the value of n to be constant. The best choice of δ_{max} would therefore be that which gives the least variation in slope. Comparing the statistics of the range of slopes obtained for each value of δ_{max}, the value of δ_{max} which gives the lowest standard deviation of n is $\delta_{\text{max}} = 0.35$. Taking

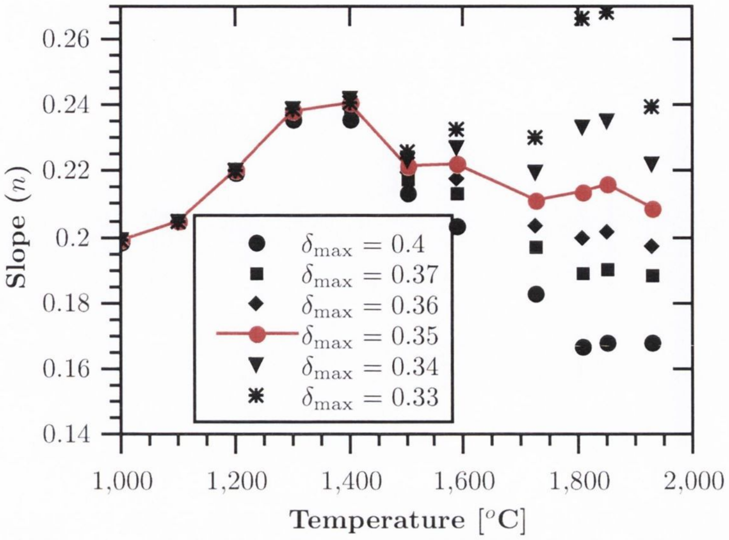

Figure 2.3: The slope obtained from a linear fit of $\log(\frac{\delta}{\delta_{\text{max}}-\delta})$ vs. -$\log(P_{O_2})$ plotted against temperature for six different values of the parameter δ_{max}. The red points correspond to the slopes of lines plotted in Fig. 2.2.

the average of these slopes to be n and the standard deviation to be the error we get $n = 0.218 \pm 0.013$.

To evaluate each linear fit, the variance in the R^2 regression value was plotted against temperature. From Fig. 2.4 we can see that for $\delta_{\text{max}} = 0.33$ the R^2 regression value drops below 0.96 at high temperatures. The rest of the values of δ_{max} give good linear fits over the range investigated, with δ_{max} = 0.35 - 0.36 having the best average values, both around $R^2 = 0.997$. The value $\delta_{\text{max}} = 0.35$ gave the most consistent slope and is the best fit of the published equilibrium data.

The best fit value of $\delta_{\text{max}} = 0.35$ can now be applied to further analyze the equilibrium data. Taking the natural logarithm of Eqn. 2.9 allows us to

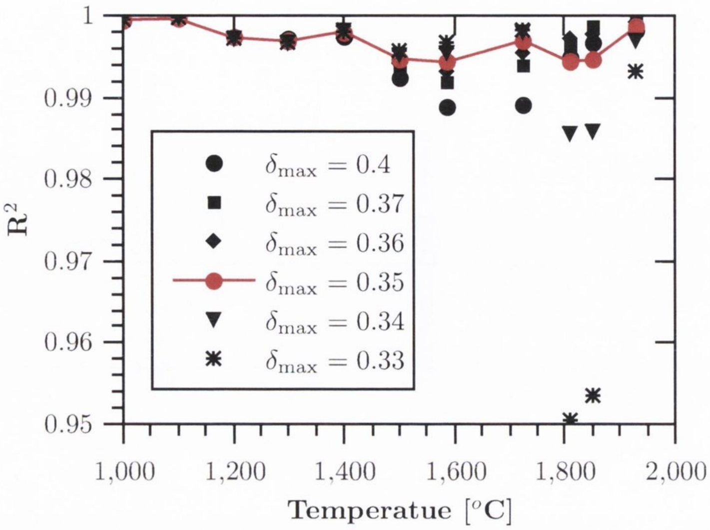

Figure 2.4: The R^2 value obtained from a linear fit of $\log(\frac{\delta}{\delta_{\max}-\delta})$ vs. $-\log(P_{O_2})$ plotted against temperature for five different values of the parameter $\delta_{\max}$. Again the red points correspond to the data plotted in Fig. 2.2.

easily extract the difference in activation energies ΔE.

$$\ln\left(\frac{\delta}{\delta_{\max}-\delta}\right) = \frac{-\Delta E}{RT} + \ln\left(P_{O_2}^{\,n}\frac{A_{\mathrm{rd}}}{A_{\mathrm{ox}}}\right) \tag{2.11}$$

From Eqn. 2.11 we see that a plot of $\ln\left(\frac{\delta}{x-\delta}\right)$ vs. $\frac{1}{RT}$ should be lines with slope $-\Delta E$.

Each set of data plotted in Fig. 2.5 was fit linearly. Taking the average value calculated from the slopes as the activation energy and the standard deviation as the error we get $\Delta E = 195.6 \pm 1.2\,\mathrm{kJ\,mol^{-1}}$

The values of $\delta_{\max}$, n and ΔE can now be used to get information from the intercepts of Fig. 2.2 and 2.5. This will allow us to determine the ratio between the frequency factors $\dfrac{A_{\mathrm{rd}}}{A_{\mathrm{ox}}}$. Taking the average of all the values determined from the linear fit intercepts of Fig. 2.2 and Fig. 2.5, and taking

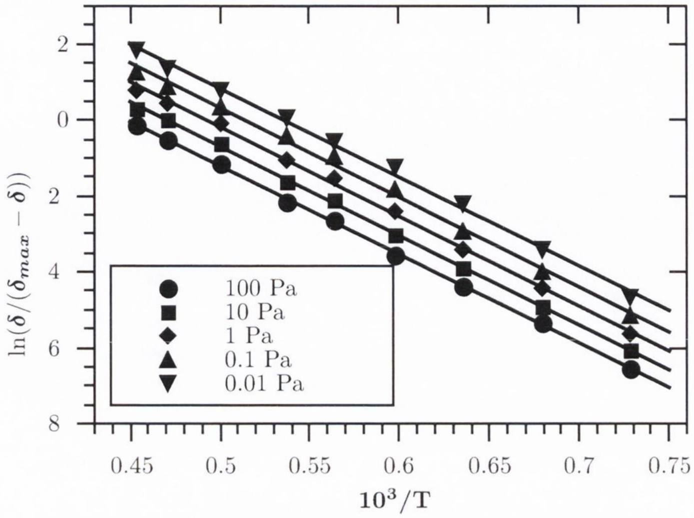

Figure 2.5: A graph of $\ln\left(\frac{\delta}{\delta_{\mathrm{max}} - \delta}\right)$ vs. $\frac{10^3}{T}$ for a range of different pressures. The data is again taken from Panlener *et al.* [91] and Zinkevich *et al.* [95]. The data was fit linearly and from the slope of each line we can calculate the difference in activation energies ΔE

the standard deviation as the error we get $\frac{A_{\mathrm{rd}}}{A_{\mathrm{ox}}} = 106000 \pm 1000\ \mathrm{Pa}^n$. The units of Pa^n are from our choice to absorb the constant of proportionality between the oxygen partial pressure and the oxygen gas concentration into A_{ox}.

Substituting the above values into Eqn. 2.9 gives

$$\left(\frac{\delta}{0.35 - \delta}\right) = 106000 \times P_{O_2}^{-0.217} \exp\left(\frac{-195.6\ \mathrm{k\,J\,mol^{-1}}}{RT}\right), \qquad (2.12)$$

which only depends on the oxygen partial pressure and temperature. In Fig. 2.6, we plot the results of the fits along with the original data from Fig. 2.5 on a linear scale. As can be seen, the results of the fit match the original data quite well on a linear scale.

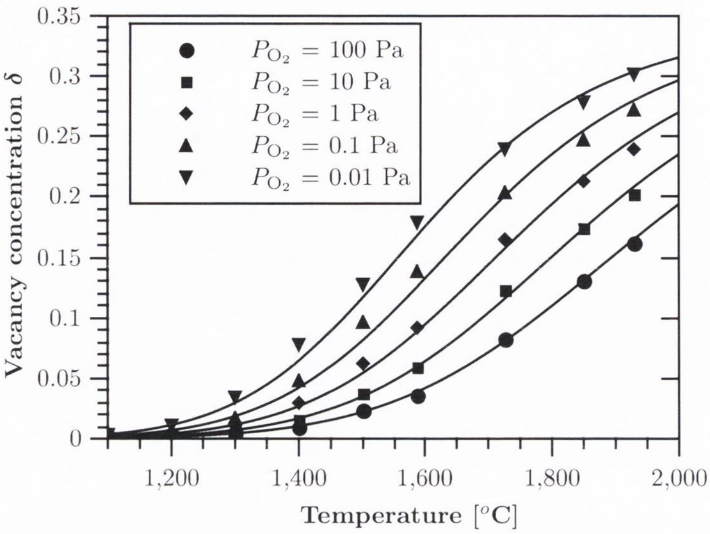

Figure 2.6: A plot of the vacancy concentration δ vs. temperature. The points are the same data (from the literature) as Fig. 2.5, and the lines are the values predicted by the model.

2.2.2 Reaction kinetics

In order for oxygen to leave CeO_2 it must first diffuse to the surface. This diffusion process may conversely be considered as the diffusion of oxygen vacancies. For simplicity we will consider spherical particles. This means we can use the spherically symmetric diffusion equation

$$\frac{\partial \delta(T,t,r)}{\partial t} = \frac{1}{r^2}\frac{\partial}{\partial r} D(\delta,T) r^2 \frac{\partial \delta(T,t,r)}{\partial r}, \tag{2.13}$$

where the solution only depends on the radial position.

The boundary condition at the surface of a spherical particle of radius r_p can now be set as our reaction rate formula

$$\frac{\partial \delta_{r_p}}{\partial t} = (\delta_{\max} - \delta_{r_p}) A_{\mathrm{rd}} \exp\left(\frac{-E_{\mathrm{rd}}}{RT}\right) - \delta_{r_p} P_{O_2}^{n} A_{\mathrm{ox}} \exp\left(\frac{-E_{\mathrm{ox}}}{RT}\right), \tag{2.14}$$

where δ_{r_p} is the boundary vacancy concentration. As before, the units could be simplified by dividing each concentration by the concentration of cerium.

If the diffusion coefficient D, and the particle radius r_p, are both known then the problem is a simple partial differential equation in one spatial dimension. The diffusion coefficient for CeO_2 can generally be well described with an Arrhenius dependence on temperature [120, 121].

$$D(T) = D_o \exp\left(\frac{-E_d}{RT}\right) \tag{2.15}$$

As we deviate from stoichiometry and the concentration of oxygen vacancies increases the diffusion coefficient will also increase [122]. Therefore the complete diffusion coefficient should be a function of both temperature and oxygen vacancy concentration.

$$D(\delta, T) = D_o(\delta) \exp\left(\frac{-E_d(\delta)}{RT}\right) \tag{2.16}$$

In the temperature range 900 - 1100 °C and for vacancy concentrations δ in the range 0 - 0.2, Stan *et al.* [123] found that both $D_o(\delta)$ and the diffusion activation energy $E_d(\delta)$ were well described by a linear dependence on δ. The temperature range however is too narrow for use in this work. Here we are dealing with a wide range of temperatures and oxygen partial pressures, and so a full analytical solution of the diffusion problem is impractical. We will later simplify the effect of diffusion by assuming a shrinking core model.

To complete the rate equation, the values of E_{rd} and A_{rd} or E_{ox} and A_{ox} need to be determined. During the reduction of ceria at high temperature, the kinetics are determined by the balance between both the oxidation and reduction terms in our equation. There are sources which suggest activation energies for the reduction reaction [105, 107, 124], although the values vary from 101.2 kJ mol^{-1} [105] to 221 kJ mol^{-1} [107]. It is also difficult to determine exactly what activation energy they have extracted from the data due to the combination of oxidation and reduction.

Instead consider the oxidation of oxygen deficient ceria at moderate temperatures. At relatively moderate temperatures (500 - 1000 °C), the reduction term should be very small relative to the oxidation term due to its much larger activation energy (E_{rd}-$E_{\mathrm{ox}} \approx 196\,\mathrm{kJ\,mol^{-1}}$). So at moderate temperatures we can treat the reaction kinetics for a reduced sample as only the oxidation term in Eqn. 2.5, which gives

$$\frac{d\delta}{dt} = -\delta P_{O_2}^{\,n} A_{\mathrm{ox}} \exp\left(\frac{-E_{\mathrm{ox}}}{RT}\right). \tag{2.17}$$

By examining this reaction it should be possible to determine the remainder of the unknown constants in the rate equation.

2.3 Experimental Procedure

The aim of the following experiments was to investigate both the backward and forward reactions of the equilibrium reaction shown in Eqn. 2.1. In other words when displaced from equilibrium in either direction how quickly does the system return to equilibrium. Most importantly we first wish to investigate the re-oxidation of cerium since, according to Eqn. 2.17 this should allow us to extract E_{ox} and A_{ox}.

An apparatus was built by the author which allows oxides to be heated to high temperatures in a controlled atmosphere. The apparatus consists of a vacuum chamber in which the sample is placed, and a focused Xenon lamp for rapidly heating the sample to reaction temperatures. The Xenon lamp uses an elliptical mirror to focus 100 Watts of broadband power into a focal point less than 8 mm in diameter. This allows temperatures up to 1650 °C to be achieved.

Changes in pressure are measured using a capacitance manometer, and the gas composition is monitored using a mass spectrometer. Oxygen released from the sample is observed by an increase in pressure and an increase in the oxygen signal measured by the mass spectrometer. Conversely oxygen absorbed by the sample is accompanied by a drop in pressure and a drop in the oxygen signal.

Figure 2.7 shows a schematic of our apparatus (for a photograph of the system see Fig. 4.4). The type B thermocouple is placed on top of the sample and the Xenon lamp is focused onto the sample and thermocouple. The sample holder is an alumina crucible surrounded by another layer of alumina to protect the steel chamber from the high temperatures.

A reduction cycle is started by pumping the chamber down to 1 Pa, and then sealing the chamber off from the pump. The lamp is then switched on to heat the sample to high temperatures. The changes in sample temperature, gas temperature, pressure and gas composition are recorded.

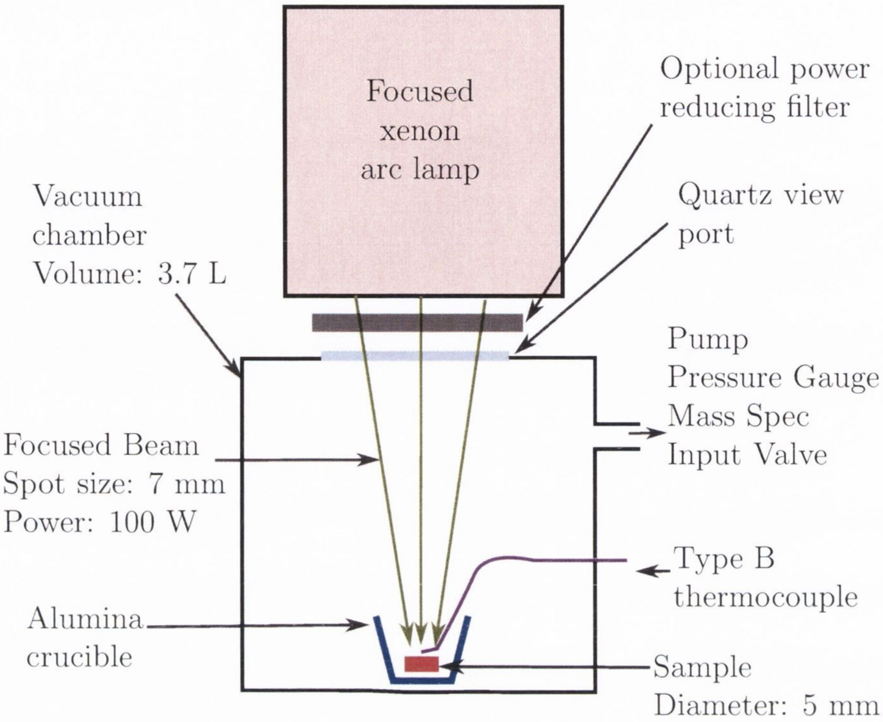

Figure 2.7: Apparatus schematic showing the vacuum chamber, Xenon lamp, sample, thermocouple and connected instruments.

A re-oxidation cycle is conducted by first pumping the chamber down to 1 Pa, the chamber is then back-filled with oxygen to a pressure of $P_{O_2} = 14\,\text{Pa}$. This pressure was selected to give us a measurable reaction rate at the temperatures used for re-oxidation (500 - 1000 $°C$). The sample is then heated using the Xenon lamp with the input power reduced by a filter. The changes in temperature, pressure and gas composition are again recorded.

The background pressure increase due to heating of the chamber without a sample present was taken into account for both an empty chamber under reduction conditions and a chamber filled with oxygen under oxidation conditions. In the case of the re-oxidation cycles, the power incident into the chamber is relatively moderate and the increase in pressure is negligible.

One issue identified with the system is that for the high temperature reduction cycles, the oxygen given off was seen to take part in other reactions as the cycle proceeds. This was observed as a decrease in the oxygen signal from the mass spectrometer and an increase in the carbon dioxide signal. No such competing reactions were observed in the re-oxidation cycles. We believe that the high power incident into our chamber during the reduction cycles is causing reactions with the chamber walls. For this reason our system is less accurate in measuring reduction than oxidation. This is not a big problem as the main experimental focus is on re-oxidation and reduction experiments will only be used for comparison with the model.

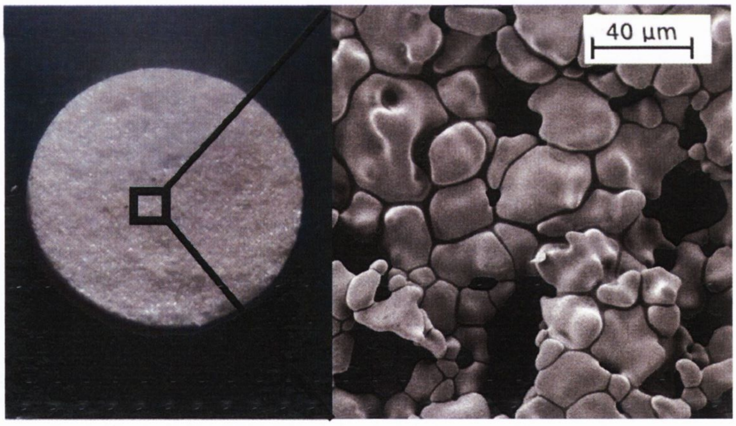

Figure 2.8: Image of a sample with an image taken using a scanning electron microscope showing its porosity.

The samples used are porous pellets of CeO_2. They were prepared by mixing CeO_2 powder (Sigma-Aldrich: **544841**) with a grain size less than 25 nm and graphite powder (Sigma-Aldrich: **282863**) with a grain size less than 20 μm. They were mixed in a volumetric ratio of three parts graphite to one part ceria. The powders were thoroughly mixed by placing them in a beaker and vibrating them in a sonic bath for fifteen minutes. Additionally polished ball bearings were placed in the beaker to accelerate mixing. The mixed powder was then pressed into pellets using a pellet die and a hydraulic press. The pellets are then annealed at 1000 °C for 3 hours. During this annealing the graphite undergoes auto-combustion leaving void space within the pellets. This was followed by 24 hrs of annealing at 1500 °C to induce sintering. The sintered pellets are on average 4.5 mm in diameter and 1 mm in height. The porosity was calculated by measuring the mass and volume of the samples to be in the range 60-65% void space and their masses were in the range 28-30 mg.

The arc lamp focuses the light into a spot approximately 7 mm in diameter, and therefore the entire sample fits into the focal point. For this reason we believe that the temperature gradients throughout the sample will be small, and in the analysis it is assumed that the sample temperature was uniform.

2.4 Experimental Results

As described above we will first look at the re-oxidation of reduced cerium,

$$CeO_{2-\delta} + \frac{\delta}{2}O_2 \longrightarrow CeO_2 \tag{2.18}$$

which should allow the remaining parameters to be fixed.

Typically in these oxidation experiments, the total amount of oxygen absorbed was in the range of δ = 0.06-0.07. Again here, δ is a dimensionless number of moles of vacancies per moles of cerium. The variance was thought to come from the reduction step carried out prior to the start of the experiment, and the samples were assumed to be fully re-oxidised at the end of the experiment. This is an approximation, as there will still be some vacancies present, but the concentration of vacancies can be assumed to be small.

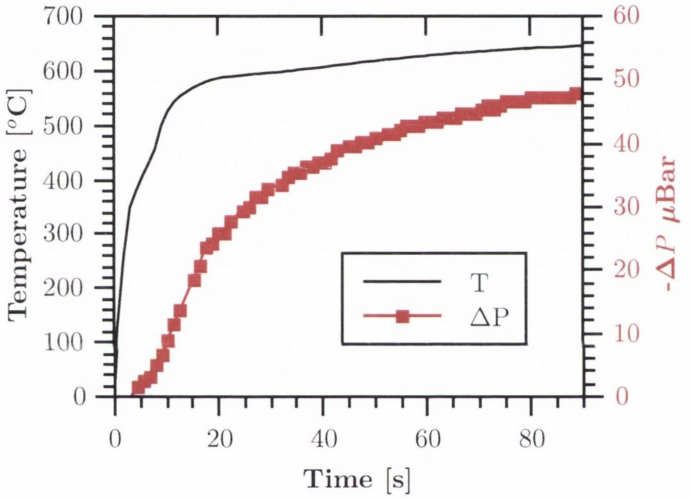

Figure 2.9: A graph showing sample temperature and the drop in pressure for the re-oxidation of a ceria pellet.

The volume of the chamber, changes in pressure and gas temperature are all known. Therefore, using the formula $\Delta PV = \Delta nRT$, the number of moles of oxygen which have been absorbed by the sample can be calculated. For the initial phase of the reaction, the rate-determining feature is the reaction at the surface and not the diffusion through the bulk. Additionally, to make an Arrhenius plot, a varying temperature is needed which happens during the initial stage of the reaction. As seen in figure 2.9 the samples quickly reach steady state temperature after which point the data is no longer useful for Arrhenius plots as the temperature is no longer changing. For these reasons it is convenient to study the reaction in the region of 0-40% completion. Equation 2.17 can be rearranged to

$$\ln\left(-\frac{d\delta}{dt}\right) - \ln(\delta P_{O_2}^{n}) = \frac{-E_{\text{ox}}}{RT} + \ln(A_{\text{ox}}), \tag{2.19}$$

which gives a suitable plot for extracting the activation energy E_{ox} and frequency factor A_{ox}.

This can be thought of as an Arrhenius plot of $\ln(k)$ vs. $\frac{10^3}{T}$. The values of δ and P_{O_2} are calculated from the data obtained from the pressure manometer and mass spectrometer. A number of cycles were conducted. All cycles started at room temperature similar to that shown in Fig. 2.9. The cycles were run for a range of different input powers, with the final temperatures reached in the range 500-1000 °C. We assume that in this range the reaction kinetics are still of the type discussed and should be well described by Eqn. 2.19.

The data was analysed with a regression fit as seen in Fig. 2.10, and the 95 % confidence interval was taken as the error in the slope and the intercept. The oxidation activation energy was calculated to be $E_{\text{ox}} = 36 \pm 4$ kJ mol^{-1} and the frequency factor found was $A_{\text{ox}} = 6.7 \pm 3.4$ s^{-1} Pa^{-n}. This value should depend on the surface to volume ratio. The value of surface to volume ratio will change due to sintering during the reduction, so the low precision for the value A_{ox} is not surprising. However, the ratio between the

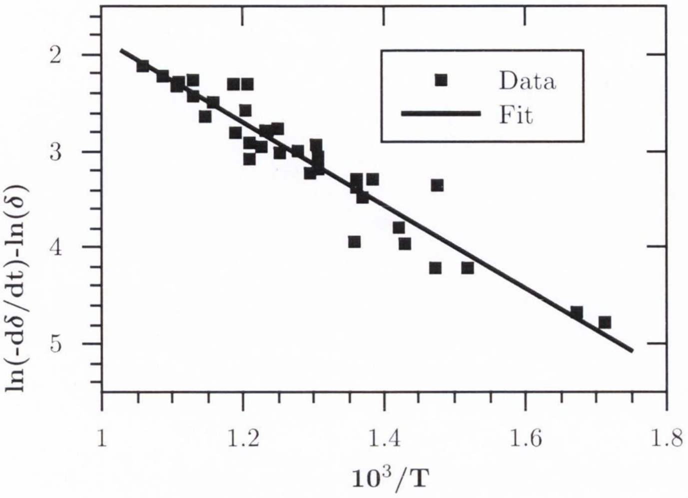

Figure 2.10: A plot of $\ln(k)$ vs. $\frac{10^3}{T}$. These points are from several different scans, where the temperature evolution during the initial heating period is plotted against the corresponding $\ln(k)$ at the same points.

frequency factors $\frac{A_{\text{rd}}}{A_{\text{ox}}}$ is a characteristic property of the material and was determined with greater precision.

E_{rd} and A_{rd} can now be calculated using our values for E_{ox}, A_{ox} and the results from the analysis of equilibrium data for ΔE and $\frac{A_{\text{rd}}}{A_{\text{ox}}}$. In summary we have the equation

$$\frac{d\delta}{dt} = (x-\delta)A_{\text{rd}}\exp\left(\frac{-E_{\text{rd}}}{RT}\right) - \delta P_{O_2}^{\,n} A_{\text{ox}}\exp\left(\frac{-E_{\text{ox}}}{RT}\right), \tag{2.20}$$

with the parameter values given in Table 2.1.

The oxygen partial pressure is in pascals, if another unit is used, the value of A_{ox} must be changed accordingly. Remember, the rate equation has been divided by the concentration of cerium to make the concentration terms unit-

δ_{max}	0.35
n	0.218 ± 0.0013
ΔE	$195.6 \pm 1.2\,\text{kJ mol}^{-1}$
E_{rd}	$232 \pm 5\,\text{kJ mol}^{-1}$
E_{ox}	$36 \pm 4\,\text{kJ mol}^{-1}$
$\frac{A_{\text{rd}}}{A_{\text{ox}}}$	$106000 \pm 1000\ \text{Pa}^{n}$
A_{rd}	$720000 \pm 360000\ \text{s}^{-1}$
A_{ox}	$6.7 \pm 3.4\ \text{s}^{-1}\text{Pa}^{-n}$

Table 2.1: Constants in Eqn. 2.20

less. Therefore this rate must be multiplied by the concentration of cerium to get the absolute rate of reaction. The oxidation term in the ranges of temperature, oxygen partial pressure and vacancy concentration considered in our re-oxidation experiment can now be calculated to be at least 4 orders of magnitude greater than the reduction term in our rate equation.

2.4.1 Model vs. Experiment

In order to test the model we can compare our re-oxidation reactions to ones predicted by the model. The temperatures recorded by the thermocouple were used in a numerical model of the rate. The oxygen partial pressure is set to be the same as the initial value and is reduced proportionally as the reaction proceeds. To account for diffusion at the later stages of the reaction, a shrinking particle model is used. In particular, the case of a small particle in which the surface reaction is the rate determining step is employed [125].

This assumes that there is a shrinking sphere of vacancies, and introduces the additional restriction

$$\frac{d\delta}{dt} = \mathbf{rate} \times (1-\alpha)^{\frac{1}{3}}. \tag{2.21}$$

Where **rate** in Eqn. 2.21 corresponds to the rate given in Eqn. 2.20. The fraction completed α, is the amount of absorbed oxygen divided by the total final absorbed oxygen. This is a simplification of the effect of diffusion, for a full analytical solution one must solve Eqn. 2.13 and 2.14 on a suitable sized sphere. It is assumed that the re-oxidation proceeds to the final fully oxidised state with $\delta = 0$.

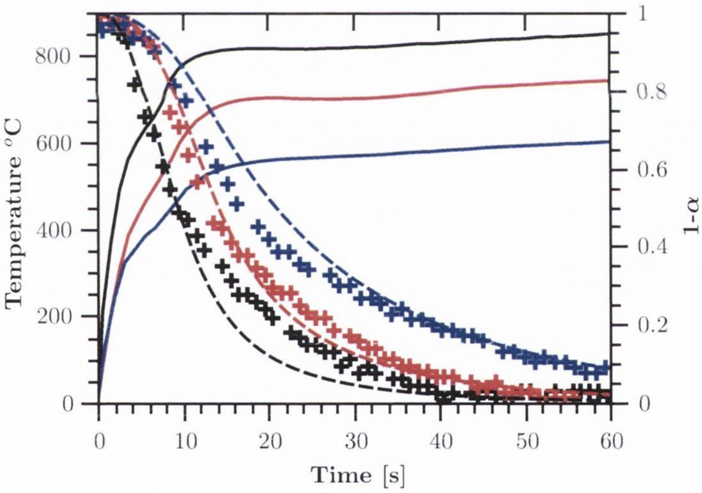

Figure 2.11: Experimental temperature and the corresponding fraction of remaining oxygen vacancies for three different input powers. The solid lines are the temperature, the crosses are the experimental fraction of remaining oxygen vacancies and the dashed lines are those predicted by Eqn. 2.21.

From Fig. 2.11 it can be seen that the experimental results agree well with the model. If the diffusion term is omitted, after the initial stages of the reaction the model predicts faster oxidation than was experimentally observed.

The rate of the reduction reaction of CeO_2 can also be compared to the model. Again Eqn. 2.21 is used to model the reaction. In the experiment the parameters are measured once every second, however the reduction reaction proceeds very rapidly, and so our temperature curves have low resolution. For this reason analytical curves of radiative heating which are very similar to the ones seen in the experiment were used in the numerical model. In this case the value α is more difficult to determine. As the temperature and oxygen pressure change so does the equilibrium δ. The fraction completed α can be defined as the instantaneous value of δ divided by the equilibrium value, so in order to determine α we must recalculate both the equilibrium δ and the actual δ in each iteration of the numerical model. Again as the reaction proceeds the oxygen partial pressure in the model increases accordingly, just as it would in the experiment.

The rate curves observed in the experiment have very similar shapes to those predicted by our model. The model predicts a somewhat faster reaction, which could be attributed to the assumption that the entire pellet is uniformly heated. In reality, the bottom of the pellet is heated at a lower rate as the pellet is a porous ceramic which has poor heat transfer properties[96]. This will reduce the rate. The final value in the model is that of equilibrium, but in our experiment the final values were all roughly 30% lower than predicted by the model. This could be due to reactions with the chamber walls absorbing oxygen as described in the experimental procedure. It could also be due to trapped unreacted oxide in our pellets.

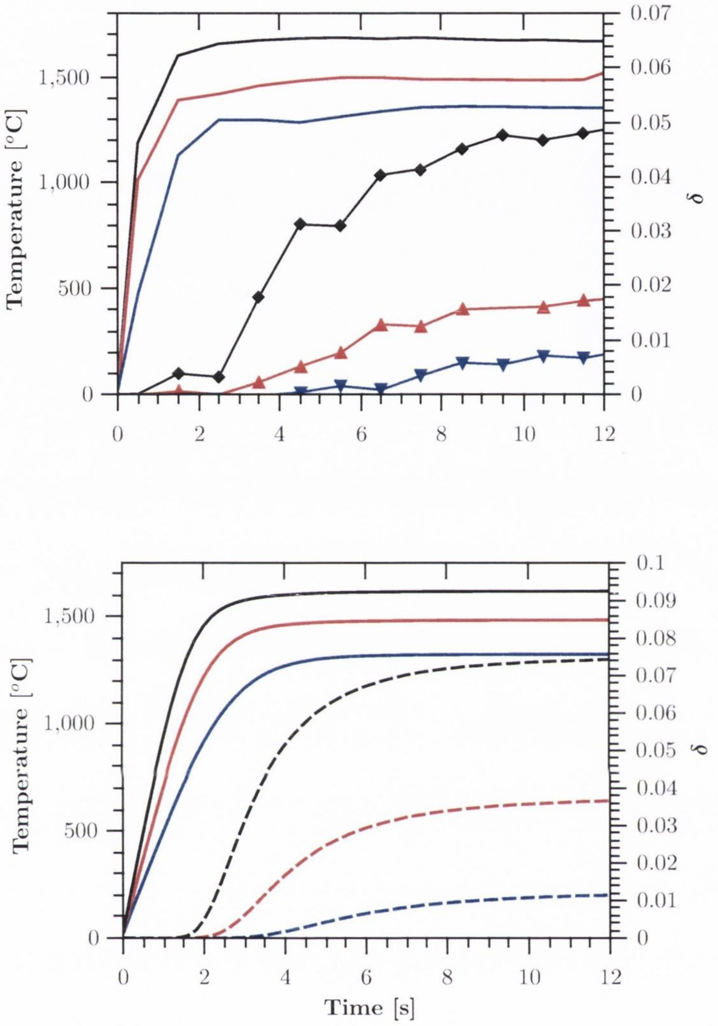

Figure 2.12: Top: Experimental temperature and the corresponding measured δ for three different input powers. Bottom: A numerical model with similar temperature curves and the corresponding numerical rates predicted.

2.5 Discussion

The discussed model of the kinetics of the high temperature reduction and oxidation of cerium dioxide agrees well with the equilibrium and kinetic data presented in this work, however the model kinetics remain to be tested over a wider range of temperatures and pressures.

2.5.1 Theoretical issues

It should be noted that the activation energy for reduction found here of $E_{\mathrm{rd}} = 232 \pm 5\,\mathrm{kJ\,mol^{-1}}$ is far lower than the overall change in enthalpy $\Delta\mathrm{H} \approx 480\,\mathrm{kJ\,mol^{-1}}$ for ceria reduction [91]. However, it is widely believed that producing an oxygen vacancy at the surface of ceria takes less energy than creating a vacancy in the bulk. The change in enthalpy is then broken up into two parts, the energy change required to produce a vacancy at the surface plus the energy change due to migration of this vacancy to the bulk. In the review by Saur *et al.* [126], a value of $321\,\mathrm{kJ\,mol^{-1}}$ is given in Table 4 for oxygen vacancy formation at the surface.

These formation energies are still a good deal larger than the activation energy we have found. However, this formation of a surface vacancy could itself be a multi step process. For example, initially an oxygen surface defect could be formed in which an oxygen molecule is displaced from its usual position, this oxygen molecule could then be removed from the surface more easily. Either of these steps could then be the rate determining step. The activation energy required to produce a vacancy could then be as low as the value we have found. This low activation energy may also explain the relative ease at which oxygen vacancies can be formed in ceria despite the large enthalpy of formation for bulk vacancies.

The activation energies determined experimentally by other authors for the thermal reduction of cerium are also very low when compared to the enthalpy of formation. A value of $221\,\mathrm{kJ\,mol^{-1}}$ was obtained by Alex Le Gal and Stephane Abanades for the reduction of cerium dioxide doped with zirconium [107]. This is lower than the value found here for pure cerium dioxide which makes sense, as a higher oxygen yield is obtained when cerium is doped with zirconium which would imply a lower activation energy. In the work presented by E. Ramos-Fernandez at The Materials for Energy conference held in Karslruhe Germany, they found an activation energy for the reduction of pure ceria to be $236\,\mathrm{kJ\,mol^{-1}}$ [127], which is within the error of the value found in this work.

Different surfaces of ceria will also have different formation energies for oxygen vacancies. This should not effect the bulk thermodynamics, but may have an effect on the kinetics. We cannot bring further clarity to this issue as our experiments were carried out with polycrystalline samples. Our values for activation energies are representative of averages over the various facets present in the ceria pellets.

2.5.2 Model applications

This model should be particularly useful in the development and assessment of syn-gas producing reactors based on the ceria redox system. It can easily be coupled to heat flow simulations, one simply needs to introduce a heat source to account for the reaction consuming or producing heat given by

$$Q = \frac{d\delta}{dt}\Delta H, \tag{2.22}$$

where ΔH is the change in enthalpy for the reaction [91].

In the case where dopants are added to ceria to improve the stability and reaction yields we should be able to modify our equation to suit. Both ZrO_2 and HfO_2 have been shown to improve the high temperature redox properties of CeO_2 [106, 108, 110, 128]. The crystal structure however remains unchanged and so the same reaction model should still be applicable with a suitable change in the constants.

The model also gives us the boundary condition for the diffusion equation if the ceria is in an oxygen atmosphere. This should allow for a more indepth study of the effect of temperature and composition on the diffusion of oxygen in the bulk.

2.6 Cavity Reactor

To demonstrate the model's practicality it has been coupled to FEM heat flow simulations of a cavity type rector. The simulated cavity reactor is very similar to the one constructed by Chueh *et al.* shown in Fig. 1.8 in Chapter 1 [102]. In terms of size the model was scaled up by approximately an order of magnitude compared to the tested reactor. The geometry was simplified to concentric shells of porous ceria and insulation, with an aperture through which radiation can enter and leave. Figure 2.13 shows the meshed geometry and for illustration it also shows the input CSP passing through a CPC. Both the ceria and the insulation layers are 2 cm thick.

The mesh has a course distribion along the inner surface as we would not expect a large temperature gradient along this surface. However, porous

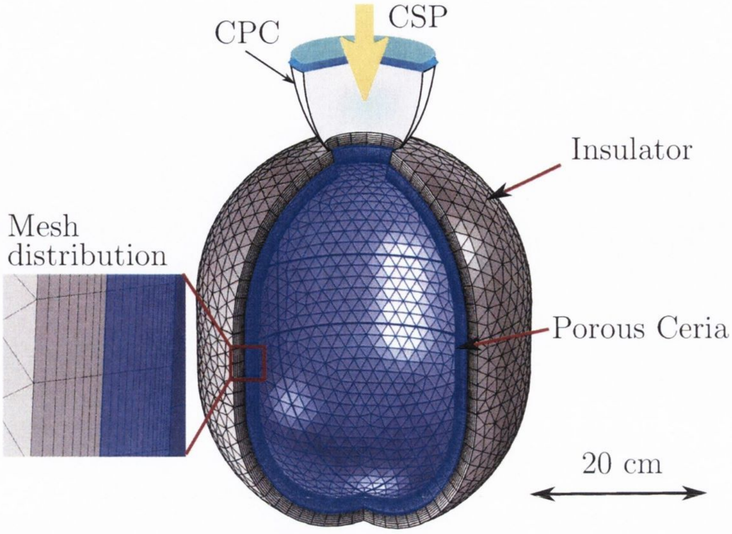

Figure 2.13: A schematic of the reactor FEM geometry, showing the mesh and a hypothetical solar power input through a CPC.

ceria is a poor heat conductor resulting in larger temperature gradients perpendicular to the surface. For this reason the mesh is denser perpendicular to the surface which receives the radiation. The simulation solves the heat equation

$$\rho C_p \frac{\partial T}{\partial t} = k \bigtriangleup T + Q \qquad [\mathrm{W\,m^{-3}}], \tag{2.23}$$

$$Q = \Delta H \frac{n_{\mathrm{CeO_2}}}{V_{\mathrm{CeO_2}}} \frac{d\delta}{dt} \qquad [\mathrm{W\,m^{-3}}], \tag{2.24}$$

where $\frac{n_{\mathrm{CeO_2}}}{V_{\mathrm{CeO_2}}}$ is the moles of ceria per unit volume (mol m^{-3}), k is the thermal conductivity, and ΔH is the energy consumed (J mol^{-1}). These equations are solved over the meshed geometry shown in Fig. 2.13.

The heat source Q, is negative due to heat being consumed by the reduction reaction described by Eqn. 2.24, where the rate is determined using the model. The outer surface of the cavity was assumed to lose heat to the surroundings via radiation exchange with the ambient, which can be described using the Stefan-Boltzmann law as a boundary condition,

$$\hat{n} \cdot (k\nabla T) = \epsilon\sigma(T_{amb}^4 - T^4). \tag{2.25}$$

On the inner boundary there is surface to surface radiation heat exchange and radiation losses through the cavity aperture via radiation to ambient. For a given surface node this is given by

$$\hat{n}_i \cdot (k\nabla T_i) = \epsilon(G_i - \sigma T_i{}^4), \tag{2.26}$$

where the incoming radiation G_i, is the sum of the incoming ambient radiation and the radiation from all of the other inner surface nodes which reaches node i. The value of G for a specific node, can be numerically calculated using the equation

$$G_i = \sum_{j=0\ j\neq i}^{N} F_{ji}T_j^4 + F_{amb}T_{amb}^4, \tag{2.27}$$

where F_{ji} is the view factor of surface i from surface j, and F_{amb} is the ambient view factor. The view factor F_{ji} is the fraction of the radiation leaving surface j, which is incident onto surface i. It depends on the distance between the elements, their unit normals and their areas. All F_{ji} must be calculated for each node, however the relative coarseness of the mesh around the inner surface helps to reduce the number of computations.

The material properties are given in Table 2.2. An approximate value is given for the specific heat capacity of ceria, ignoring its temperature dependence. A simulation in which the emissivity was varied between 0 and 1 was

Material	k	C_p	ρ	ϵ
Porous Ceria	$2.5\,\mathrm{W\,m^{-1}\,K^{-1}}$	$\approx 480\,\mathrm{J\,kg^{-1}\,K^{-1}}$	$1500\,\mathrm{kg\,m^{-3}}$	1
Insulation	$0.05\,\mathrm{W\,m^{-1}\,K^{-1}}$	$200\,\mathrm{J\,kg^{-1}\,K^{-1}}$	$1500\,\mathrm{kg\,m^{-3}}$	0.05

Table 2.2: Material properties used in the FEM simulation

conducted in order to see its effect. For values of emissivity greater than 0.4, there was very little change in the power absorbed. This is because there are multiple internal reflections inside the cavity and thus most of the radiation is eventually absorbed. For simplicity the inner surfaces were then set to radiate as black bodies for the remainder of the simulations ($\epsilon = 1$). The outer surface was set to have a low emissivity of 0.05 in order to approximate more insulation or an outer reflective layer.

The simulation is time dependent and it starts with the porous ceria at a temperature of 1273 K. The simulation stops when any piece of the reactor reaches 1923 K. The oxygen partial pressure was assumed to be constant at $P_{\mathrm{O}_2} = 1$ Pa. For simplicity, it was assumed that this partial pressure was maintained by a vacuum, which limits our heat transfer to radiative heat transfer only.

In this example the input power was varied to check the effects of various solar concentrations on the reactor's performance.

The input power was given a Gaussian distribution around the inner surface which is shown in Fig. 2.14. This was used as an approximation of the power distribution one might expect to come from a CPC. The temperature variation around the inner surface in Fig. 2.14 is small, which shows that the

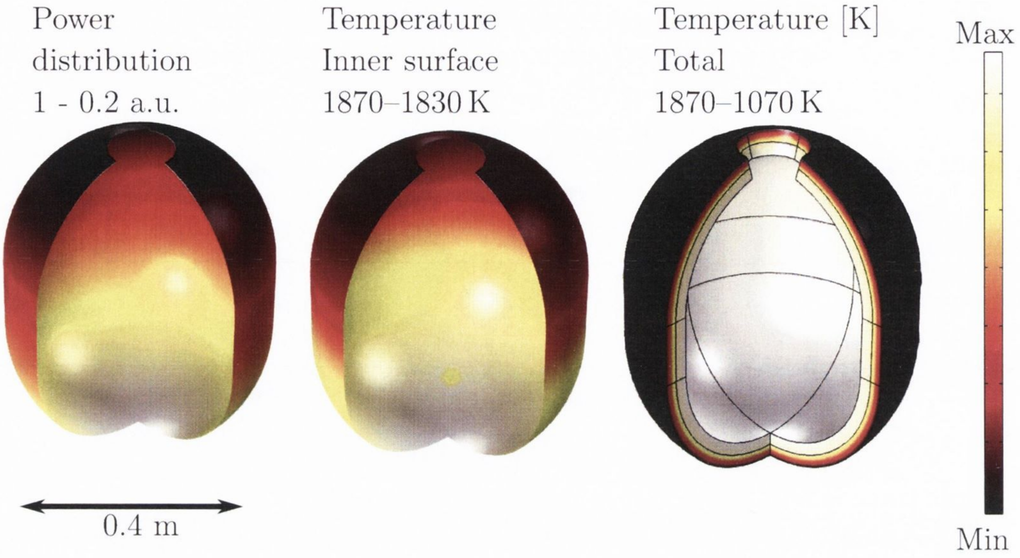

Figure 2.14: Color plots of the normalised power distribution, the temperature around the inner surface and the temperature over the whole reactor near the end of reduction.

incoming power is effectively distributed around the cavity by radiative heat transfer.

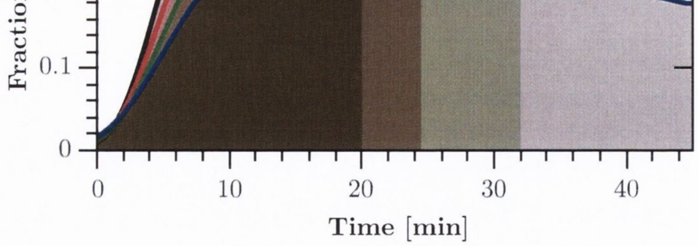

Figure 2.15: Fraction of the total input power consumed vs. time for a number of different input power densities, which are given in $kW\,m^{-2}$.

In order to evaluate the reactor performance, we can integrate the heat consumed by the ceria reduction, and the power absorbed and emitted by the insulation and inner surfaces of the reactor. Figure 2.15 shows the fraction of the total input power which is consumed by the reduction vs. time. The input power density in kW m^{-2} corresponds roughly to the solar concentration, so the highest input power would require a concentration factor of 1900 suns. The higher the input power the shorter the time the reactor takes to reach the maximum temperature. The power consumed is plotted here as a normalised quantity, with the total input power being 1. Therefore, the area under each curve divided by the area of the total normalised power (1 × time), gives the fraction of the total energy supplied which is consumed by the reaction.

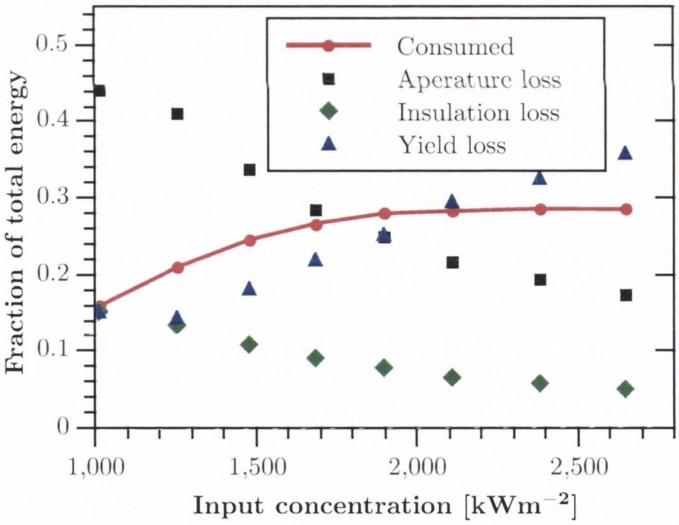

Figure 2.16: Fraction of total energy supplied vs. input concentration for the energy consumed, the energy re-radiated through the aperture and the energy lost through the insulation. Also shown is the yield loss which is another normalised quantity.

From Fig. 2.16 we see that with increasing input power both the insulation losses and the aperture losses decrease. This can be understood by considering that for a given input power the reactor will have a steady state temperature where the heat losses are equal to the input power. This temperature increases with input power, so the reactor is further from steady state for greater input powers and thus suffers less losses.

The consumed power increases with input power, but eventually begins to approach a limiting value. The theoretical limit for the fraction of heat consumed is given by the heating efficiency, η_{heat}, in Chapter 3. However, it is not exactly the value approached in this case, as higher input powers result in less uniform heating. This means that not all of the ceria reaches the maximum reduction and thus less heat is consumed. This can be seen by considering the yield loss which is described by the equation

$$\text{Yield loss} = 1 - \frac{\text{Yield obtained}}{\text{Maximum yield}}. \tag{2.28}$$

The maximum yield is the yield one would get if all of the ceria was heated to the maximum temperature and reached reaction equilibrium. The yield loss increases with the input power. For the higher input powers the ceria is heated very fast and thus there are greater temperature gradients in the ceria. This is important for both yield and reactor durability as thermal shock could reduce reactor lifetime. If for higher powers the ceria could be heated uniformly, then the fraction of total energy consumed would approach the theoretical limit.

Although very simplified, such simulations can provide excellent insight into what might limit a reactors performance.

2.7 Conclusions

An Arrhenius type model for the thermal reduction and oxidation of CeO_2 in an oxygen atmosphere was developed by considering the processes involved in the reactions. By analyzing equilibrium data from the literature with the model as a template, we were able to fix the difference between the activation energies of reduction and oxidation, the oxygen partial pressure dependence, the ratio of the frequency factors and the maximum removable oxygen in this reaction regime. We then examined the re-oxidation of cerium in order to determine the activation energy and frequency factor for the re-oxidation term in the model. This fixed the remainder of the constants involved in the model. The model's reaction kinetics were then compared to novel experimental data. The experimental results agree well with the model predictions in the temperature and pressure ranges examined.

The model should be particularly useful for reactor design work. Its simple analytical form means it can easily be coupled to heat flow and or chemical species transport simulations. This should allow for more accurate optimization of reactor design.

In the next chapter the model is employed in a thermodynamic analysis of fuel production using CeO_2.

Chapter 3

Thermodynamics of CeO_2 fuel production

In this chapter the thermodynamics of thermochemical fuel production using a CeO_2 redox cycle are studied. The need to reduce the oxygen partial pressure in order to improve efficiency is investigated, with both sweep gas and vacuum pumping considered as methods of achieving this. At ambient pressure the cycles can be maximised with respect to the temperature swing, the minimum oxygen partial pressure and the extent of the oxidation reaction. For reduction at 1500 °C the maximum fuel conversion efficiency was found to be 4.5%, which is significantly lower than the values found in previous studies. In addition isothermal operation had very low efficiency (less than 2%) under all of the conditions considered. If the system is operated at lower than ambient pressure, the pumping efficiency will depend on the pressure. From an investigation of commercially available pumps the pressure dependence was given an analytical expression. The results showed the cycles have an optimal operating pressure, and that using sweep gas as well as pumping, only reduced the overall efficiency. The efficiency was maximised with respect to the temperature swing, the reduction pressure and the extent of oxidation, giving a peak efficiency of 7.5% for a reduction temperature of 1500 °C. Reducing the pressure during reduction could also be beneficial due to improved reaction kinetics at lower pressure, and an increased yield due to lower oxygen partial pressures. Recovering heat from both the high temperature ceria and the oxidation reaction, and using it as process heat was also considered. With 60% of this heat being recovered, the peak efficiency for the 1500 °C pumped cycle increased to 11%. Finally the practicality of the cycles, in terms of the quantity of ceria required to maintain continuous operation, are considered and some suggestions for improving the cycle are given.

3.1 Introduction

Thermodynamic studies of the ceria fuel production cycles suggest that solar to fuel efficiencies exceeding 30 % could be achievable [129, 130]. In practice fuel conversion efficiencies have been low, with values less than 2 % [93, 102]. In this chapter a more in-depth analysis of different cycle conditions is explored with an aim of better understanding if and how these high efficiencies can be achieved.

The majority of work performed on ceria has been for temperature swing cycles. However, some recent studies have brought to light the possibility of an isothermal cycle [131–134]. An isothermal fuel production cycle based on ceria has been demonstrated at the laboratory scale by Venstrom *et al.* [99].

A recent thermodynamic study by Ermanoski *et al.* suggested that isothermal fuel production would have low efficiency due to the unfavorable thermodynamics of an isothermal cycle [135]. They explain that the oxidation and reduction reactions do not proceed spontaneously and without some additional work the yields will be reduced. Instead, the authors determine that there must be a temperature difference between oxidation and reduction which offers a maximum efficiency. This maximum arises because there is a trade off between energy losses due to cycling the temperature and the losses due to operating the cycle under unfavourable thermodynamic conditions.

In this chapter an analysis of the efficiency of such cycles with a realistic look at the different constraints affecting the efficiency is provided. This includes an analysis on different methods used to reduce the oxygen partial pressure during reduction and a full analysis of the oxidation reaction. This allows the efficiency to be maximised by selecting the cycle parameters.

The oxygen partial pressure can be reduced using a sweep gas with low oxygen concentration (*e.g.* N_2), by pumping the system to a lower operating pressure during reduction or by some combination of these two methods. The minimum quantities of sweep gas required are calculated using equilibrium considerations.

The pumping efficiency is given a pressure dependence which has not been considered in previous studies. The lower the operating pressure of the reactor, the less efficient the pumps will be. This is due to pump leakage which increases with decreasing pressure, and the thermal losses which increase with the compression ratio. In addition smart pumping (in which oxygen is pumped off at it's equilibrium pressure) is used to minimise the energy needed for pumping. This idea was recently noted by Ermanoski, who considered the effect of performing reduction in a series of chambers each with decreasing pressure [136], which increased the efficiency.

The oxidation reaction is also given full consideration with the amount of oxidiser needed determined from equilibrium considerations. In some previous cases this quantity may have been underestimated. Here we also introduce a fraction completed parameter to allow the oxidation to stop short of completion which can greatly reduce the amount of oxidiser required.

Finally the practicality of the cycle is discussed based on the amount of ceria which must be used in a reactor per kW of power stored as fuel. These considerations depend on the cycle time (reaction kinetics) and the yield of the cycle.

3.2 Thermodynamics

All of the thermodynamic properties used in this study have an analytical form, meaning that the calculations are very simple and can be reproduced with basic mathematical software. The aim of this is to allow other authors to easily modify the calculations to determine the maximum thermodynamic efficiencies for specific reactor properties.

It is also important to note that the analytical functions given require the temperature to be in Kelvin and the pressure in bar. However, the plots and the descriptions give the temperature in terms of Celsius for the convenience of the reader.

In the case of a temperature swing cycle, there are inevitably difficulties in recuperating the heat used to change the temperature of the ceria and reusing it in the cycle. There have been some ideas for solid state heat recuperation within the cycle. A counter rotating ring design was proposed by Sandia National Laboratories [58, 60], which allows the relatively hot ceria coming from the reduction zone to transfer heat to the relatively cool ceria coming from the oxidation zone. A similar design was proposed by Lapp *et al.* which used counter rotating concentric cylinders [137]. Unfortunately, the implementation of these designs would greatly increase the reactor complexity and likely introduce unnecessary thermal losses. For this reason it is initially assumed that the solid state change in temperature of the ceria is lost heat (although, some of this heat could be utilised for heating the incoming H_2O and CO_2).

$$\mathrm{CeO}_{2-\delta_{\mathrm{ox}}} \xrightarrow{heat=\Delta H_{\mathrm{rd}}} \mathrm{CeO}_{2-\delta_{\mathrm{rd}}} + \frac{\Delta\delta_{\mathrm{eq}}}{2}\mathrm{O}_2 \qquad T_{\mathrm{rd}} \qquad P_{f\mathrm{O}_2} \tag{3.1}$$

$$\mathrm{CeO}_{2-\delta_{\mathrm{rd}}} + \Delta\delta_{\mathrm{eq}}\mathrm{H}_2\mathrm{O} \longrightarrow \mathrm{CeO}_{2-\delta_{\mathrm{ox}}} + \Delta\delta_{\mathrm{eq}}\mathrm{H}_2 \qquad T_{\mathrm{ox}} \qquad \mathrm{H}_2\mathrm{O} \tag{3.2}$$

$$\Delta T = T_{\mathrm{rd}} - T_{\mathrm{ox}} \qquad \Delta\delta_{\mathrm{eq}} = \delta_{\mathrm{rd}} - \delta_{\mathrm{ox}} \tag{3.3}$$

The cycle reactions are described by equations 3.1 and 3.2. The ceria is reduced at a temperature T_{rd} in a low oxygen atmosphere with an oxygen partial pressure of $P_{f\mathrm{O}_2}$, to a vacancy concentration of δ_{rd}. It is oxidized at a temperature T_{ox} in a 1 bar steam atmosphere (H_2O) to a vacancy concentration δ_{ox}. Only cycles for which $T_{\mathrm{rd}} \geq T_{\mathrm{ox}}$ are considered, and thus the temperature difference ΔT is always positive or zero ($\Delta T \geq 0$). The equilibrium yield per cycle is the difference in the vacancy stoichiometry $\Delta\delta_{\mathrm{eq}}$. For convenience, the deviations from stoichiometry δ, are defined as a unit-less oxygen vacancy concentration.

$$\delta = \frac{[\mathrm{O_{vac}}]}{[\mathrm{Ce}]} \tag{3.4}$$

Where $[\mathrm{O_{vac}}]$ is the concentration of oxygen vacancies and $[\mathrm{Ce}]$ is the concentration of cerium atoms.

The values for equilibrium vacancy concentrations δ can be obtained from the equilibrium equation

$$\left(\frac{\delta}{0.35-\delta}\right) = 8700 \times P_{\mathrm{O_2}}^{-0.217} \exp\left(\frac{-195.6\ [\mathrm{kJ\,mol^{-1}}]}{RT}\right), \tag{3.5}$$

which is derived in the previous chapter (Eqn. 2.12) and in a publication written by the author [138]. The pre factor here of 8700 is different to that in Eqn. 2.12 as we have switched pressure units from Pascals to bar. Here the temperature must be given in Kelvin and the oxygen partial pressure in bar. Re-arranging this Eqn. yields an expression for δ which depends only on temperature and oxygen partial pressure, $\delta(T, P_{\mathrm{O_2}})$. In order to calculate δ_{rd}, both T_{rd} and the final oxygen partial pressure $P_{f\mathrm{O_2}}$ are substituted into Eqn. 3.5. The final oxygen partial pressure $P_{f\mathrm{O_2}}$, is the target lower partial pressure to be attained at the end of the reduction cycle.

In order to calculate δ_{ox}, T_{ox} and the oxygen partial pressure in 1 bar of H_2O at T_{ox}, were substituted into Eqn. 3.5. A similar calculation for CO_2 gives lower values of δ_{ox}, which is more favourable in terms of yield. The values of P_{O_2} in 1 bar of H_2O or CO_2 were calculated and are shown in the appendix of this chapter using standard equilibrium conditions.

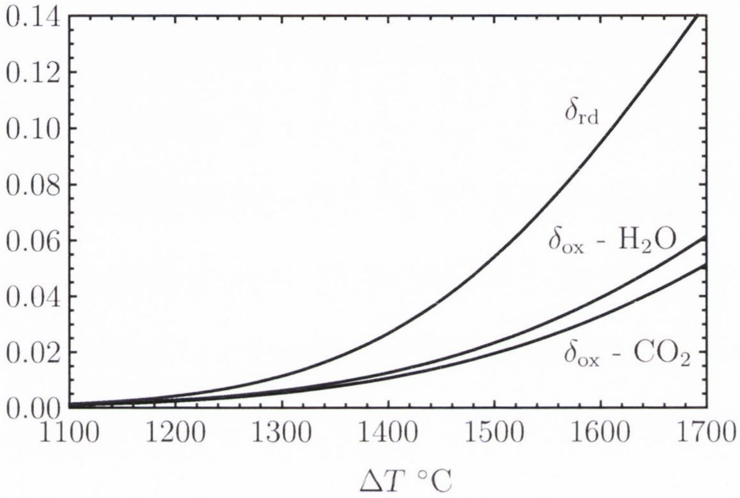

Figure 3.1: The equilibrium stoichiometry δ vs. the temperature T for a reduction with $P_{fO_2} = 1\times10^{-5}$ labelled δ_{rd}, an atmosphere of 1 bar H_2O labelled δ_{ox}, and an atmosphere of 1 bar CO_2 labelled δ_{ox} - CO_2.

Figure 3.1 shows the values of equilibrium δ in a low oxygen partial pressure atmosphere, a steam atmosphere and a CO_2 atmosphere. An isothermal cycle will have a change in stoichiometry equal to the difference between the reduction and oxidation values for a given temperature. The values of δ_{red} and δ_{ox} here agree well with the previous thermodynamic analysis of Bader *et al.* [132].

3.2.1 Reduction and heating

The energy required to remove oxygen from ceria is the change in enthalpy for reduction ΔH_{rd}. This change in enthalpy was found by Panlener *et al.* to only depend on the stoichiometry δ [91]. The curve for the change in enthalpy given in Panlener's work was extracted and fit with a polynomial.

$$\Delta H_{\mathrm{rd}}(\delta) = (478 - 1158\ \delta + 1790\ \delta^2 + 23368\ \delta^3 - 64929\ \delta^4) \times 10^3 \quad [\mathrm{J\,mol^{-1}}] \tag{3.6}$$

The heat required to reduce one mole of ceria from δ_{ox} to δ_{rd} can then be calculated by integrating the molar change in enthalpy from δ_{ox} to δ_{rd}. However, oxidising the ceria to δ_{ox} requires that the ceria oxidation reaction reach equilibrium, which will require excessive amounts of oxidiser. Therefore, it is useful to introduce a stopping point for the oxidation reaction,

$$\delta_{\mathrm{ox}}(\alpha) = \delta_{\mathrm{ox}} + (1 - \alpha)\Delta\delta_{\mathrm{eq}} \qquad 0 < \alpha \leq 1 \tag{3.7}$$

where α is the fraction complete. Setting α to values less than one stops the oxidation reaction short of equilibrium. The energy required to reduce a mole of ceria is then

$$Q_{\mathrm{rd}} = \int_{\delta_{\mathrm{ox}}(\alpha)}^{\delta_{\mathrm{rd}}} \Delta H_{\mathrm{rd}}(\delta) d\delta \quad [\mathrm{J\,mol^{-1}}]. \tag{3.8}$$

For a given cycle, as described previously, there is also the energy cost of heating the ceria. This is given by

$$Q_{\mathrm{CeO_2}} = \int_{T_{\mathrm{ox}}}^{T_{\mathrm{rd}}} C_{p_{\mathrm{CeO_2}}}(T)dT \quad [\mathrm{J\,mol^{-1}}], \tag{3.9}$$

where the specific heat capacity of ceria was obtained from the work of Pankratz [2], and fit with a polynomial (see appendix) in the range 300 - 2300 K. The dependence on δ was ignored as within the ranges of δ considered (0 - 0.1), only a 1.5 % change in heat capacity is predicted [95].

The heating efficiency can now be defined as

$$\eta_{\mathrm{heat}} = \frac{\alpha\Delta\delta_{\mathrm{eq}}\mathrm{HHV}_{\mathrm{H_2}}}{Q_{\mathrm{rd}} + Q_{\mathrm{CeO_2}}}, \tag{3.10}$$

where $\alpha\Delta\delta_{\mathrm{eq}}\mathrm{HHV}_{\mathrm{H_2}}$ is the energy stored in the fuel, and $Q_{\mathrm{rd}} + Q_{\mathrm{CeO_2}}$ is the heat required to reduce and change the temperature of the ceria. These are the heat inputs to the main part of the reactor as seen in Fig. 3.6. The heating efficiency should clearly show the energy losses due to the difference in enthalpies ($\Delta H_{\mathrm{rd}} - \mathrm{HHV}_{\mathrm{H_2}}$) and the energy required to cycle the temperature. It sets an upper bound on the fuel production efficiency when there is no solid state heat recovery.

In Fig. 3.2 the heating efficiency is plotted for a range of different $P_{f\mathrm{O_2}}$, with $T_{\mathrm{rd}} = 1500$ °C, which is taken as the standard reduction temperature throughout the rest of the chapter. For the values of $P_{f\mathrm{O_2}} > 10^{-4}$, the heating efficiency becomes negative for small ΔT. This is because the cycle is no longer possible as $\Delta\delta_{\mathrm{eq}} < 0$. Otherwise, the heating efficiency again

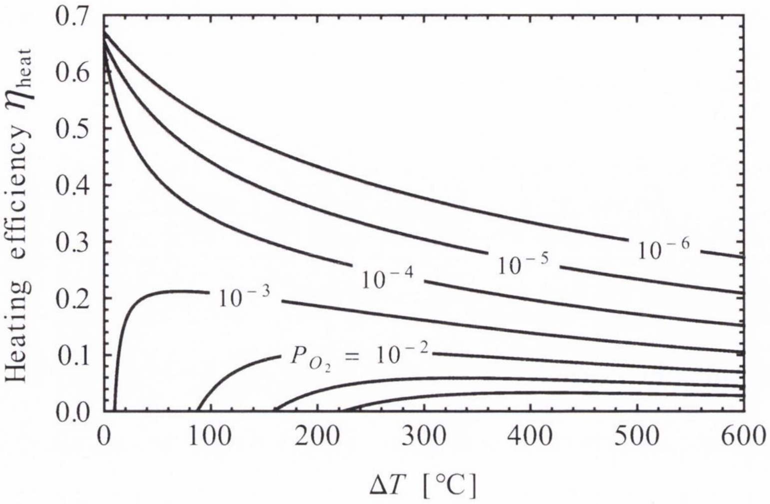

Figure 3.2: Heating efficiency vs. the change in temperature ΔT for a range of values of P_{fO_2} (1 to 10^{-6} bar), with $T_{\text{rd}} = 1500$ °C and $\alpha = 1$.

increases with decreasing ΔT and P_{fO_2}. The ceria cycle could be operated with reduction in pure oxygen at ambient pressure, shown by the lowest line in the graph ($P_{fO_2} = 1$ bar), but the heating efficiency is very low (≈ 3 % for $\Delta T = 500$ °C). This shows the importance of reducing the oxygen partial pressure during reduction.

Another very important aspect is the yield, $\Delta\delta_{\text{eq}}$. The number of moles of ceria that need to be heated per cycle to produce 1 mole of H_2 is the inverse of the yield, $\frac{1}{\Delta\delta_{\text{eq}}}$. The thermal losses due to heating of the ceria (re-radiation, insulation losses.. etc) will increase if more ceria must be heated to produce a mole of fuel. For this reason cycles with a larger yield should result in less thermal losses per unit of fuel produced. In addition, the practical challenges associated with cycling large amounts of ceria per unit of fuel produced may ultimately decide the technical viability of such cycles.

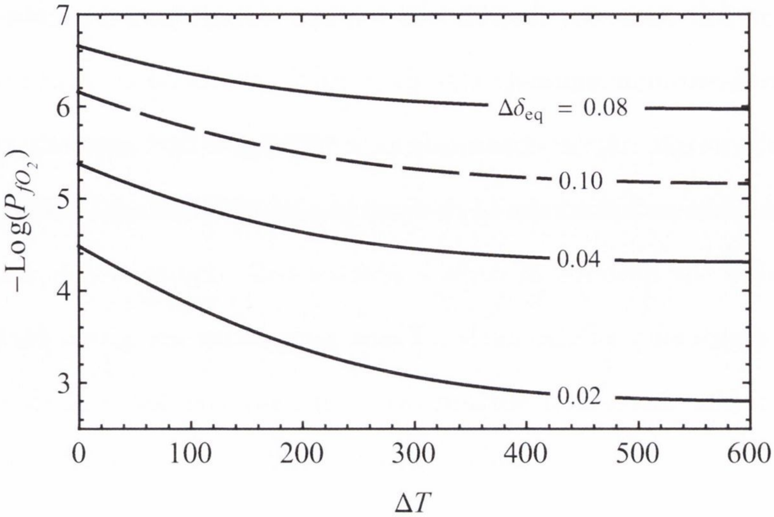

Figure 3.3: Contours of constant $\Delta\delta_{\mathrm{eq}}$ in a plot of $P_{f\mathrm{O}_2}$ vs. ΔT with T_{rd} = 1500 °C. The dashed line is for T_{rd} = 1600 °C.

In Fig. 3.3 lines of constant yield are plotted to show the effects of both $P_{f\mathrm{O}_2}$ and ΔT on the yield. Increasing ΔT allows for much higher $P_{f\mathrm{O}_2}$, which is important due to the difficulties associated with achieving such low oxygen partial pressures. The dashed line shows the effect of increasing T_{rd} to 1600 °C, which greatly reduces the constraints on ΔT and $P_{f\mathrm{O}_2}$ for a given yield. For T_{rd} = 1500 the dashed line would be outside the area of the graph at virtually unachievable partial pressures.

The yields shown above are still relatively low and will result in large amounts of ceria being cycled to produce relatively small amounts of fuel. A cycle with T_{rd} = 1500 °C, ΔT = 500 °C and oxygen partial pressures of 10^{-4}, 10^{-5} and 10^{-6} will require 29, 19 and 12 moles of ceria (4.8, 3.2 and 2 kg) respectively per mole of fuel produced (2 g). In the worst case of $P_{f\mathrm{O}_2}$ = 10^{-4} bar, a reactor with an output of 100 kW would then need to cycle ceria at a rate of 100 kgmin^{-1}. If it takes on the order of tens of minutes to complete one full cycle then a 100 kW reactor would need a number of tons of ceria to operate continuously.

Although rough, these considerations highlight the importance of the yield of the cycle and the rate of cycling (reaction kinetics). These parameters determine the amount of ceria a reactor will require which will greatly affect the practicality of the cycle. These properties are given further consideration in the discussion section, and for now the focus shall return to efficiency.

3.2.2 Sweep gas

During the reduction step the oxygen partial pressure can be reduced using a sweep gas. In this case we consider nitrogen, which can be produced via cryogenic rectification. This gives nitrogen gas with an oxygen impurity concentration of 1 ppm, with an electrical energy cost of approximately 15 $\mathrm{kJ\,mol^{-1}}$ [139]. Assuming that heat can be converted to electricity with an efficiency of 40 %, the cost of producing nitrogen for the reduction of one mole of ceria is

$$Q_{N_2} = n_{\text{gas}}(1 - \bar{x}_{O_2}) \times 37500 \quad [J\,mol^{-1}], \tag{3.11}$$

where n_{gas} is the total number of moles of gas (O_2 +N_2) which leave the reactor per mole of ceria cycled and $\bar{x}_{O_2}$ is the average mole fraction of oxygen in the sweep gas over one cycle.

It remains to determine the average mole fraction of oxygen $\bar{x}_{O_2}$ and the number of moles of gas n_{gas}, per mole of ceria cycled. The minimum n_{gas} can be calculated by assuming that all of the oxygen released during reduction is at equilibrium conditions. This gives the minimum since if the partial pressure is increased past equilibrium the reaction can no longer proceed. By rearranging Eqn. 3.5, the equilibrium P_{O_2} can be expressed as

$$P_{O_2}(\delta, T) = \left(\frac{8700(0.35-\delta)\exp\left(\frac{-195.6\ kJmol^{-1}}{RT}\right)}{\delta} \right)^{\frac{1}{0.217}} \quad [bar], \tag{3.12}$$

and the mole fraction of released oxygen is then

$$x_{O_2}(\delta, T) = \frac{P_{O_2}(\delta, T) - 10^{-6}P}{P}, \tag{3.13}$$

where the $10^{-6}P$ is to account for the 1 ppm O_2 already in the sweep gas. The number of moles of gas per mole of vacancies created is then given by

$$\frac{\partial n_{\text{gas}}(\delta, T)}{\partial \delta} = \frac{1}{2x_{O_2}(\delta, T)}, \tag{3.14}$$

where $2x_{O_2}$ accounts for there being half a mole of O_2 per mole of vacancies. In addition, n_{gas} will be at a minimum if the sweep gas is only used to remove the oxygen when at the upper temperature T_{rd}, as the equilibrium P_{O_2} goes up with temperature. The minimum n_{gas}, is then given by the normalised integral

$$n_{\text{gas}} = \frac{\int_{\delta_{\text{ox}}(\alpha)}^{\delta_{\text{rd}}} \frac{\partial n_{\text{gas}}(\delta,T)}{\partial \delta}\, d\delta}{\alpha \Delta \delta_{\text{eq}}}. \tag{3.15}$$

The maximum average mole fraction of oxygen in the product stream is then

$$\bar{x}_{O_2} = \frac{\alpha \Delta \delta_{\text{eq}}}{2n_{\text{gas}}}. \tag{3.16}$$

It is necessary to introduce an additional condition on the value of P_{O_2}. If $P_{O2} \geq P$, it must be set equal to the total pressure. In other words, in the case where no sweep gas is needed, the oxygen is just removed at the operating pressure of the reactor as it heats up, avoiding errors in the value of $\bar{x}_{O_2}$.

$$P_{O_2}(\delta, T) = \begin{cases} P_{O_2}(\delta, T) & : P_{O_2}(\delta, T) < P \\ \\ P & : P_{O_2}(\delta, T) \geq P \end{cases} \tag{3.17}$$

The maximum average oxygen mole fraction is obtained in the same way except that in Eqn. 3.13 the expression for P_{O_2} is given by Eqn. 3.17. The value $\bar{x}_{O_2}$ is very important as it determines the amount of sweep gas needed per mole of fuel produced, and hence can greatly effect the efficiency.

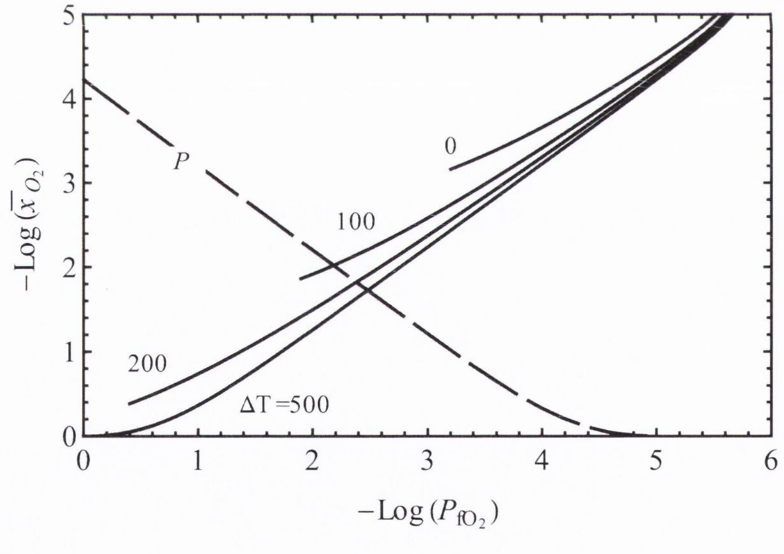

Figure 3.4: A plot of $-\log(\bar{x}_{O_2})$ vs. $-\log(P_{fO_2})$ with $T_{\mathrm{rd}} = 1500$ °C. The solid lines are for a range of values of ΔT (0, 100, 200 and 500) with $P = 1$ bar. The dashed line is a plot of $-\log(\bar{x}_{O_2})$ vs. $-\log(P)$, with $P_{fO_2} = 10^{-5}$ bar and $T_{\mathrm{rd}} = 1500$ °C.

In Fig. 3.4, the results for the cycles with $\Delta T < 500$ stop abruptly as the cycle becomes impossible when $\Delta\delta_{\text{eq}} < 0$. For reduction operating at a total pressure of 1 bar, $\bar{x}_{\text{O}_2}$ decreases with decreasing $P_{f\text{O}_2}$. The energy cost of producing nitrogen is quite high and thus cycles with low $\bar{x}_{\text{O}_2}$ ($< 10^{-2}$) will suffer from very poor efficiency. In order to obtain low $P_{f\text{O}_2}$ it may be more sensible to pump the system to lower pressures, which reduces the amount of sweep gas needed. This is illustrated by the dashed line in Fig. 3.4.

It can be seen that with $P = 1$ bar isothermal cycles have minimum $\bar{x}_{\text{O}_2}$ of $\approx 10^{-3}$, which will result in very poor efficiency. This appears to agree with the experimental demonstration of the isothermal cycle performed by Venstrom *et al.* [99], where ceria was reduced at 1500 °C using a sweep gas flow rate of 581 $\text{ml}\,\text{min}^{-1}\text{g}^{-1}$ for 9.5 min resulting in a yield of $\Delta\delta = 0.01$ (see Fig. 5 in their manuscript), which corresponds to an $\bar{x}_{\text{O}_2}$ of approximately 1.2×10^{-4}. Here the maximum $\bar{x}_{\text{O}_2}$ was calculated to be 2.0×10^{-4}, for a cycle with $T_{\text{rd}} = 1500$ °C, $\alpha = 0.66$, $\Delta T = 0$, with a yield $\alpha\Delta\delta_{\text{eq}} = 0.01$ (these values were determined from the data presented in the Venstrom paper) and using CO_2 as the oxidiser. This maximum value is greater than that obtained in practice by Venstrom *et al.* by a factor of 1.7, which seems plausible and offers some support for the calculation.

An important aspect of using a sweep gas is that it must be heated to the reduction temperature. The gas leaving the reactor can be used to heat the sweep gas entering the reactor via a heat exchanger. The energy cost of heating the sweep gas is then

$$Q_{\mathrm{gas}} = (1-\varepsilon_{\mathrm{gas}})\left(n_{\mathrm{gas}}(1-\bar{x}_{\mathrm{O}_2})\int_{T_{amb}}^{T_{\mathrm{rd}}} C_{p_{\mathrm{N}_2}}(T)dT\right) \quad [Jmol^{-1}], \qquad (3.18)$$

where $n_{\mathrm{gas}}(1-\bar{x}_{\mathrm{O}_2})$ is the number of moles of nitrogen used in the reduction of one mole of ceria and $\varepsilon_{\mathrm{gas}}$ is the heat exchanger effectiveness. The specific heat capacity of nitrogen as a function of temperature was obtained from the work of McBride *et al.* [1] and fit with a polynomial which is given in table 3.3 in the appendix of this chapter.

3.2.3 Pumping

If the system is maintained at lower than atmospheric pressure there is additional energy needed to pump the gases. It makes sense to only pump once the reactor has reached T_{rd}, as this maximises the oxygen partial pressure $P_{\mathrm{O}_2}(\delta, T)$, and thus reduces the amount of pumping work necessary.

Here we consider the optimal case, where the oxygen is pumped at its equilibrium pressure if this is greater than the target operating pressure. The upper pressure is restricted to a maximum of ambient pressure giving a pumping pressure of

$$P_{\mathrm{pmp}}(\delta, T) = \begin{cases} P_{amb} & : P_{\mathrm{O}_2}(\delta, T) > P_{amb} \\ P_{\mathrm{O}_2}(\delta, T) & : P_{amb} > P_{\mathrm{O}_2}(\delta, T) > P \\ P & : P_{\mathrm{O}_2}(\delta, T) \leq P \end{cases} \qquad (3.19)$$

The energy required to pump is assumed to be that of pumping an ideal gas

$$\frac{\partial Q_{\text{pmp}}}{\partial \delta} = \frac{RT}{2\eta_{\text{pmp}}(P_{\text{pmp}})} \ln\left(\frac{P_{\text{pmp}}(\delta, T_{\text{rd}})}{P_{amb}}\right), \tag{3.20}$$

where the factor of two accounts for there being two moles of vacancies per mole of oxygen. The total energy required to pump the gases is

$$Q_{\text{pmp}} = \int_{\delta_{\text{ox}}(\alpha)}^{\delta_{\text{rd}}} \frac{\partial Q_{\text{pmp}}}{\partial \delta} d\delta + \frac{n_{\text{gas}}(1 - \bar{x}_{\text{O}_2})RT}{\eta_{\text{pmp}}(P)} \ln\left(\frac{P}{P_{amb}}\right), \tag{3.21}$$

where the first term is that of pumping the oxygen, and the second term is the energy required to pump the sweep gas which is only used when the pressure reaches the lower value of P. The gas is assumed to be at a temperature of 70 °C during pumping. Note that the pumping efficiency η_{pump}, is given a pressure dependence which is explained later.

3.2.4 Oxidation

Finally, we have the energy costs of oxidation, which is the cost of heating the oxidiser H_2O. The oxidation is assumed to take place at ambient pressure. In the appendix of this chapter, the ratio between H_2 and H_2O for steam in equilibrium with $CeO_{2-\delta}$ is calculated to be

$$R_{\frac{\text{H}_2}{\text{H}_2\text{O}}}(\delta, T_{\text{ox}}) = \exp\left(\frac{-\Delta G_{\text{ws}}(T_{\text{ox}})}{RT_{\text{ox}}} - \frac{1}{2}\ln(P_{\text{O}_2}(\delta, T_{\text{ox}}))\right), \tag{3.22}$$

where $P_{O_2}(\delta, T_{ox})$ is given by Eqn. 3.12. The equilibrium mole fraction of H_2 is then

$$\frac{x_{H_2}}{1} = \frac{x_{H_2}}{x_{H_2O} + x_{H_2} + x_{O_2}} = \frac{\frac{x_{H_2}}{x_{H_2O}}}{\frac{x_{H_2O}}{x_{H_2O}} + \frac{x_{H_2}}{x_{H_2O}} + \frac{x_{O_2}}{x_{H_2O}}} \approx \frac{R_{\frac{H_2}{H_2O}}}{1 + R_{\frac{H_2}{H_2O}}}, \tag{3.23}$$

since $x_{H_2O} + x_{H_2} + x_{O_2} = 1$ and $x_{O_2} << x_{H_2O} + x_{H_2}$. To get the mole fraction of hydrogen produced by the reaction with ceria, the equilibrium hydrogen in a pure steam atmosphere must also be subtracted giving

$$x_{H_2}(\delta, T_{ox}) = \frac{R_{\frac{H_2}{H_2O}}(\delta, T_{ox})}{1 + R_{\frac{H_2}{H_2O}}(\delta, T_{ox})} - x_{H_2}(T_{ox})_{eq}, \tag{3.24}$$

where $x_{H_2}(T_{ox})_{eq}$ is the equilibrium mole fraction of hydrogen in an isolated H_2O atmosphere at temperature T_{ox} (calculated in the appendix of this chapter). This equilibrium mole fraction ($x_{H_2}(T_{ox})_{eq}$) must be subtracted to get the exact mole fraction of hydrogen produced by the oxidation reaction with ceria. The number of moles of oxidiser required per mole of fuel produced is then

$$\frac{\partial n_{H_2O}(\delta, T_{ox})}{\partial \delta} = \frac{1}{x_{H_2}(\delta, T_{ox})}, \tag{3.25}$$

with the total number of moles of oxidiser required to cycle one mole of ceria given by

$$n_{H_2O} = \frac{\int_{\delta_{ox}(\alpha)}^{\delta_{rd}} \frac{\partial n_{H_2O}(\delta, T_{ox})}{\partial \delta} d\delta}{\alpha \Delta \delta_{eq}}. \tag{3.26}$$

Figure 3.5 shows how $\bar{x}_{H_2}$ depends on ΔT. For isothermal oxidation hundreds of moles of oxidiser are required to produce a mole of fuel, but this decreases rapidly for increasing ΔT. Decreasing the value of P_{fO_2} also

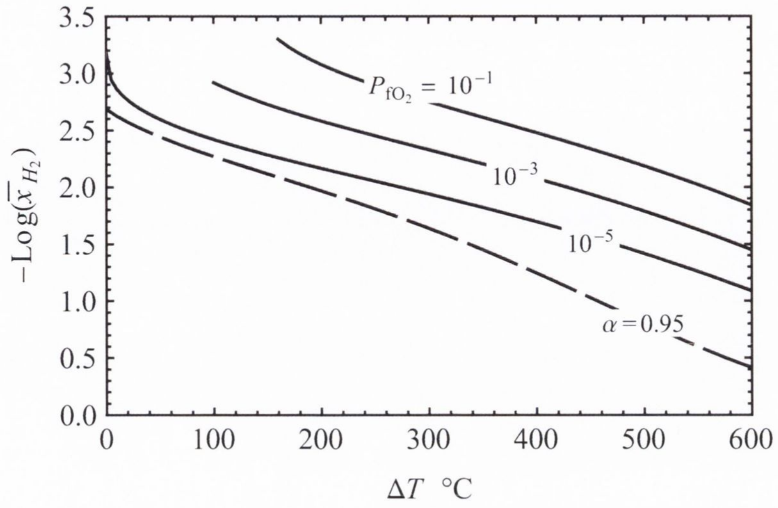

Figure 3.5: A plot of -log($\bar{x}_{\text{H}_2}$) vs. the change in temperature ΔT. The solid lines are different values of $P_{f\text{O}_2}$ (10^{-1}, 10^{-3} and 10^{-5} bar) with T_{rd} = 1500 °C. The dashed line shows the effect of stopping the oxidation reaction before equilibrium at 95 % completion, with T_{rd} = 1500 °C and $P_{f\text{O}_2} = 10^{-5}$ bar.

decreases the amount of oxidiser required, and where the lines abruptly stop is where operation becomes impossible as $\Delta\delta_{\text{eq}} < 0$. Stopping the oxidation at 95 % completion is also shown to greatly reduce the amount of oxidiser.

The calculation was also performed for an oxidiser of CO_2, the results of which are shown in Fig. 3.15 in the appendix. Again we can compare the results to the experimental demonstration of the isothermal cycle performed by Venstrom *et al.* [99], where ceria was oxidised in CO_2 at 1500 °C using an oxidiser flow rate of 297 $\text{ml}\,\text{min}^{-1}\text{g}^{-1}$ for 0.9 min, resulting in a yield of $\alpha\Delta\delta_{\text{eq}} = 0.01$, which corresponds to an $\bar{x}_{CO}$ of approximately 5.3×10^{-3}. Here the maximum $\bar{x}_{\text{CO}}$ was calculated to be 7.3×10^{-3}, for a cycle with T_{rd} = 1500 °C, $\alpha = 0.66$, $\Delta T = 0$, with a yield $\alpha\Delta\delta_{\text{eq}} = 0.01$. As before the value is larger than that obtained in practice as expected, and the numbers are reasonably close which again offers support for the calculation. The low concentration of CO is very impractical as it must be separated from the product stream, which is not a trivial task. Together with sweep gas energy costs, these technical demands will make ambient pressure isothermal operation both impractical and very inefficient.

A heat exchanger can be used to heat the oxidiser using the out flowing oxidiser and fuel. The energy required for oxidation is then given by

$$Q_{\mathrm{H_2O}} = n_{\mathrm{H_2O}}(1 - \epsilon_{\mathrm{gas}})\left(\int_{100}^{T_{\mathrm{ox}}} C_{p_{\mathrm{H_2O}}}(T)dT + L_{\mathrm{H_2O}}\right), \tag{3.27}$$

where $L_{\mathrm{H_2O}}$ is the latent heat of vaporisation of water. The same heat exchanger efficiency as that of the sweep gas heat exchanger is used for simplicity. This is a modest assumption as some of the heat released during oxidation ($Q_{\mathrm{rd}} - \alpha\Delta\delta_{\mathrm{eq}}\mathrm{HHV}_{\mathrm{H_2}}$), should also be available for heating the oxidiser.

3.2.5 Plant efficiency

In order to account for losses consider that, for a given fuel production plant, the heat required to power all of the processes can be collected and supplied with an efficiency η_{plant}. This is to account for losses in solar collection and thermal losses due to re-radiation. It can be defined as

$$\eta_{\mathrm{plant}}(T_{\mathrm{rd}}, C) = \frac{0.9(1\,\mathrm{kW} \times C - \sigma(T_{\mathrm{rd}}^4 - T_{amb}^4))}{1\,\mathrm{kW} \times C}, \tag{3.28}$$

where C is the solar concentration and the factor of 0.9 is to account for 10 % losses from the solar collectors. Note that this assumes that all the process heat is supplied to the reactor at temperature T_{rd}. This is a modest assumption as temperature swing cycles can be at lower temperatures during heating phase and some of the processes (Q_{pmp}, $Q_{\mathrm{H_2O}}$ and $Q_{\mathrm{N_2}}$) could be supplied with heat at lower temperatures.

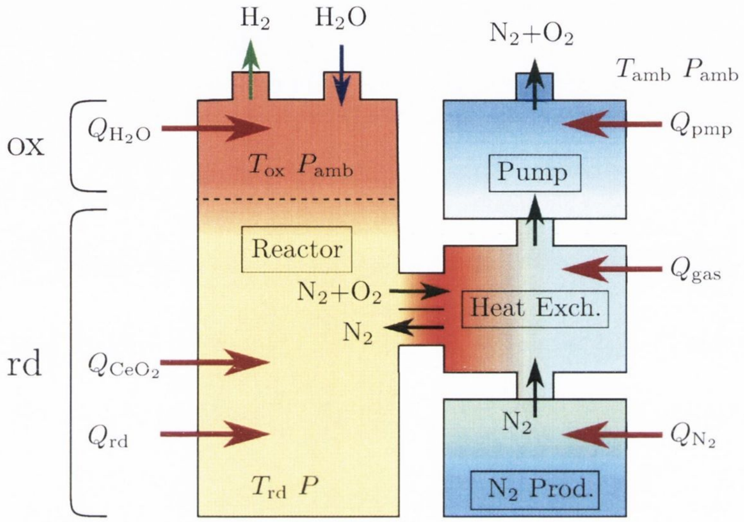

Figure 3.6: A schematic of the reactor showing the processes involved in reduction, their heat costs, and the flow of the nitrogen gas and the cycle products.

Figure 3.6 shows the various processes and heat inputs required for fuel production. The oxidation and reduction sections (seperated by a dashed line in the schematic) of the main reactor can be separated in space or in time. For spacial separation, both oxidation and reduction can be performed continuously in two separate reactor chambers allowing for automatic separation of the products H_2 and O_2. The alternative is to operate a batch reactor and perform the reduction and oxidation reactions alternately (at different times) in the same reactor. The products are produced at different times so they are again automatically separated. With all of the energy costs, the fuel production efficiency can can now be defined as

$$\eta_{\text{fuel}} = \frac{\eta_{\text{plant}} \alpha \Delta\delta_{\text{eq}} \text{HHV}_{\text{H}_2}}{Q_{\text{rd}} + Q_{\text{CeO}_2} + Q_{\text{N}_2} + Q_{\text{gas}} + Q_{\text{pmp}} + Q_{\text{H}_2\text{O}}}. \tag{3.29}$$

If the system is at ambient pressure then $Q_{\text{pmp}} = 0$ and if the system is pumped to the target lower oxygen partial pressure ($P = P_{f\text{O}_2}$) then no sweep gas is needed and $Q_{\text{N}_2} = Q_{\text{gas}} = 0$.

η_{pmp}	0.15
ε_{gas}	0.75
C	3000

Table 3.1: Initial values for efficiency and solar concentration.

The values for the process efficiencies and solar concentration were fixed and are displayed in table 3.1. It seems feasible that the heat exchanger could have an effectiveness of 0.75, providing 75 % of the heat needed for the sweep gas and oxidiser. Initially an efficiency of 15 % is used for η_{pmp} with a more in-depth analysis of pumping and the pumping efficiency given in the next section.

3.3 Results

If the system is operated at ambient pressure there should be a value of $P_{f\text{O}_2}$ which maximises the efficiency due to the trade off between the sweep gas processing ($Q_{\text{N}_2} + Q_{\text{gas}}$) costs and the amount of fuel produced ($\alpha\Delta\delta_{\text{eq}}$). For isothermal cycles the sheer quantities of sweep gas and oxidiser required means the efficiency will be very low, and so we initially focus on temperature swing cycles.

3.3.1 Ambient pressure reduction

For the initial results of reduction at atmospheric pressure the values ΔT = 500 °C and α = 0.95 were selected to offer a low $Q_{\mathrm{H_2O}}$. The calculated values of the fuel production efficiency for a range of values of T_{rd} are shown in Fig. 3.7. Each curve has a peak efficiency, and the position of the peak depends on T_{rd}. The peak is due to the fact that decreasing $P_{f\mathrm{O_2}}$ greatly reduces $Q_{\mathrm{gas}} + Q_{\mathrm{N_2}}$, which are the dominant terms at low $P_{f\mathrm{O_2}}$, but it also decreases $\alpha\Delta\delta_{\mathrm{eq}}\mathrm{HHV}_{\mathrm{H_2}}$, which ultimately reduces the efficiency for higher values of $P_{f\mathrm{O_2}}$.

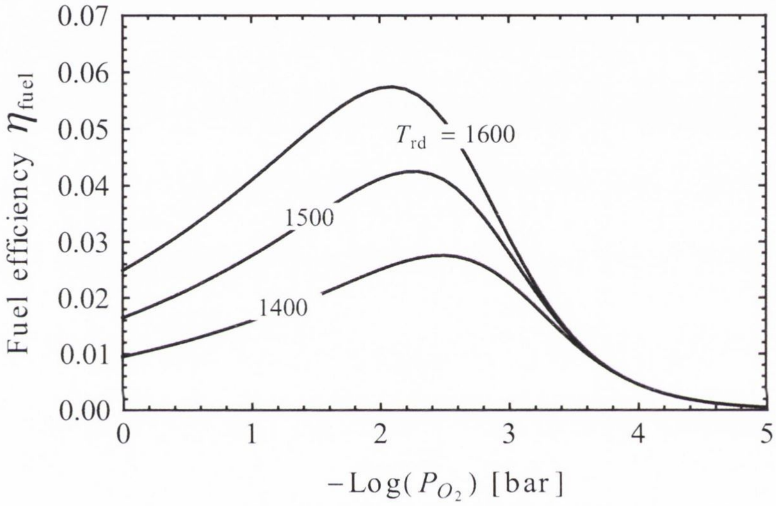

Figure 3.7: A plot of the η_{fuel} vs. $-log(P_{f\mathrm{O_2}})$ for a range of values of T_{rd} (1400 1500 and 1600 °C), with $P = 1$ bar, $\Delta T = 500$ °C and $\alpha = 0.95$.

The optimal values of $P_{f\mathrm{O_2}}$ found here offer a very poor yield and low efficiency. Despite this, it is interesting to look at the effect of ΔT on the cycle efficiency when operated at ambient pressure. Figure 3.8 shows the effect that

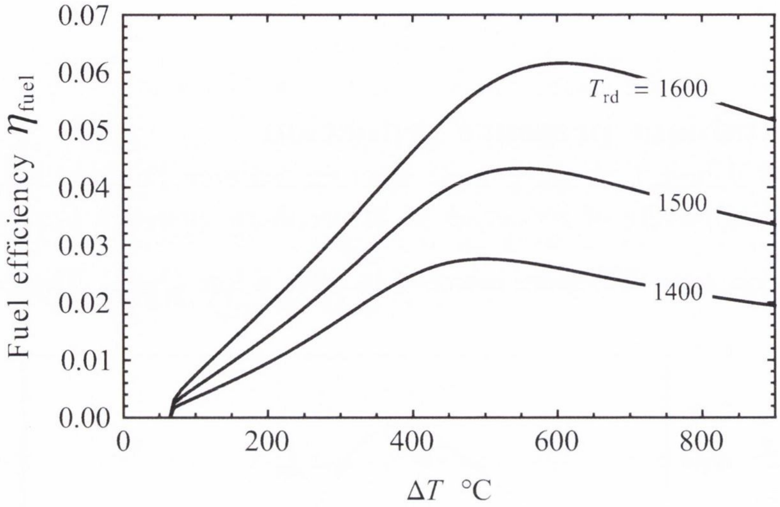

Figure 3.8: A plot of the η_{fuel} vs. ΔT for a range of values of T_{rd} (1400 1500 and 1600 °C), with $P = 1$ bar, $\alpha = 0.95$ and the peak values of P_{fO_2} from Fig. 3.7.

ΔT has on the fuel production efficiency. For small enough ΔT the efficiency goes to zero due to the cycle yield becoming negative, $\alpha\Delta\delta_{\text{eq}} < 0$. There is also an optimal ΔT which is due to a balance between the amount of heat required for oxidation Q_{H_2O}, and the amount of heat that is needed to change the temperature of the ceria, Q_{CeO_2}. With increasing ΔT, Q_{H_2O} decreases and up to a point $\alpha\Delta\delta_{\text{eq}}\text{HHV}_{H_2}$ increases. However, Q_{CeO_2} also increases and eventually increasing ΔT has a negative effect. This can all be seen in figure 3.9 which shows the effect of changing ΔT on the fractional energy costs.

For a cycle with $T_{\text{rd}} = 1500$ °C, increasing ε_{gas} from 0.75 to 0.95 raised the maximum efficiency from approximately 4 to 5 % and shifted the optimal ΔT from around 500 to 400 °C. The increase is relatively small, as although Q_{gas} and Q_{H_2O} are greatly reduced, the energy required to produce the sweep gas is

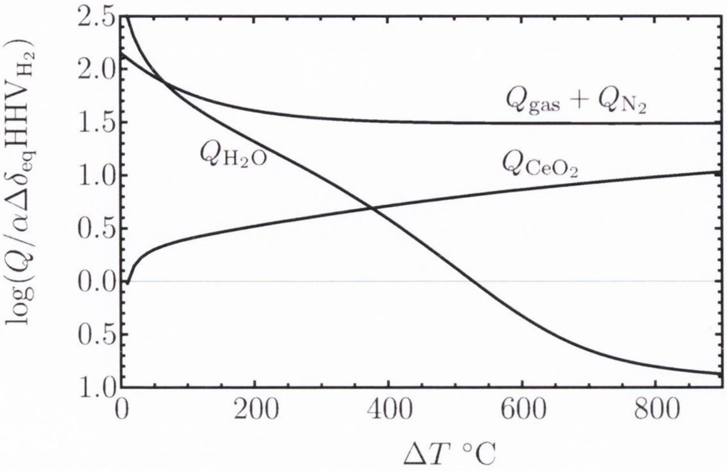

Figure 3.9: A plot of the $\log\left(\frac{Q}{\alpha\Delta\delta_{\text{eq}}\text{HHV}_{\text{H}_2}}\right)$ vs. ΔT with $T_{\text{rd}} = 1500$ °C, $P = 1$ bar, $\alpha = 0.95$ and $P_{f\text{O}_2} = 10^{-4}$.

still very high. In any case, it is unlikely that gas phase heat exchangers with such high efficiencies could be developed for the temperatures considered.

3.3.2 Reducing the reduction operating pressure

Note that the value for η_{pmp} used here is given in table 3.1, as are the values of C and ε_{gas}. Figure 3.10 shows the effect of decreasing the operating pressure on the reactor efficiency. This was assumed to be the sole method of reducing the oxygen partial pressure, so that $Q_{\text{N}_2} = Q_{\text{gas}} = 0$. There is a maximum efficiency which is due to $Q_{\text{H}_2\text{O}}$ decreasing with ΔT and Q_{CeO_2} increasing. This is very similar to the results obtained by Ermanoski *et al.* for temperature swing cycles [135].

A pumping efficiency of 15% is very high for a pressure change of three to five orders of magnitude, so this result is not realistic. In reality the pumping efficiency will decrease with decreasing pressure.

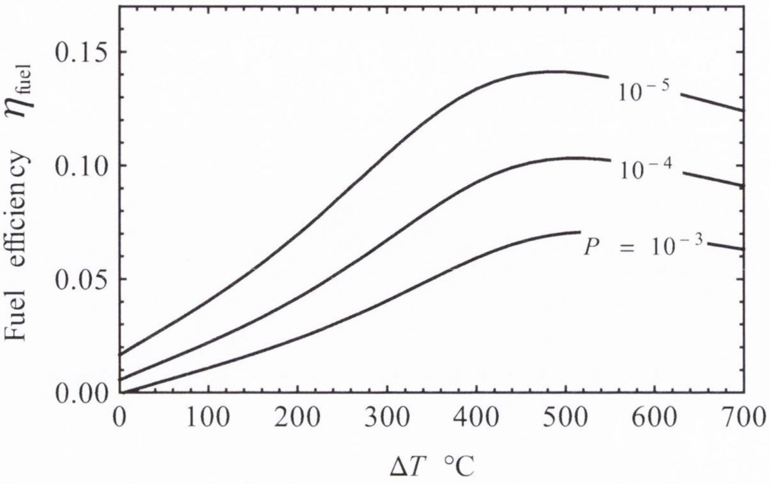

Figure 3.10: A plot of the η_{fuel} vs. the change in temperature ΔT for a range of values of reactor operating pressure P, with $T_{\mathrm{rd}} = 1500$ °C, $P_{fO_2} = P$ and $\alpha = 0.95$.

From the investigation of commercially available vacuum pumps (Busch vacuum pumps) an approximate value for the efficiency of the pump can be set. In Fig. 3.11 the pumping efficiency for some standard pumps is plotted on a log-log scale. The points form approximately a line which suggest that the efficiencies dependence on the pressure can be described with a power law.

At lower pressures the efficiency of the pumps is very low. However, the current vacuum pump industry is largely focused on simply maintaining low pressures without much interest in pumping efficiency. Efficiency improvements could likely be possible through the use of inter-cooling or the development of the more efficient axial flow type compressors for vacuum pumping. For this reason the pumping efficiency is assumed to be described by

$$\eta_{\text{elec to pump}}(P) = P^{0.5437}, \tag{3.30}$$

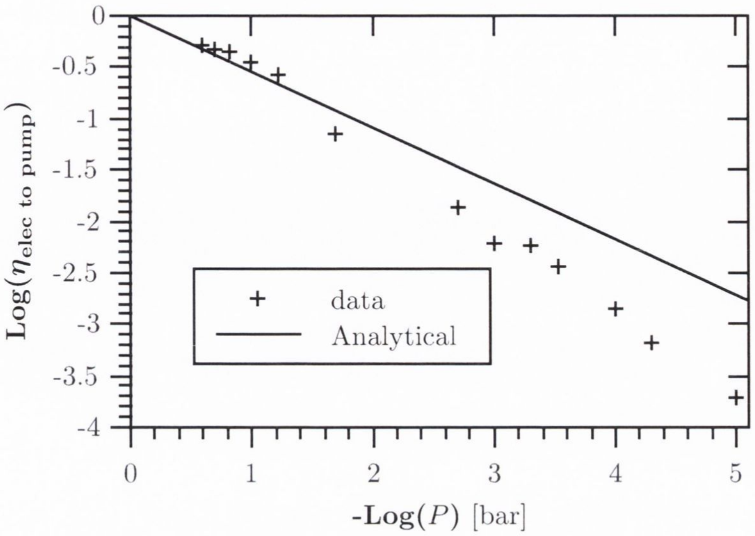

Figure 3.11: A plot of the log($\eta_{\text{pump to elec}}$) vs. -log($P$) where the points are values calculated from commercially available pump specs, and the line is the analytical expression used in here with a slope of 0.5437.

which is also plotted in Fig. 3.11. Assuming the conversion of heat to electricity has an efficiency of 40 %, the pumping efficiency will then be

$$\eta_{\text{pmp}}(P) = 0.4\,\eta_{\text{elec to pump}}(P) = 0.4\,P^{\,0.5437}. \qquad (3.31)$$

If there is no pressure change the pumping efficiency approaches 40 %, and at 10^{-5} the efficiency is almost an order of magnitude higher than the actual efficiency of the pumps investigated. The efficiency of an optimised axial flow compressor could be a lot higher, but the important fact here is that in general we would expect the pressure dependence of the efficiency to obey a power law.

Figure 3.12 shows the effect of pumping the system to lower pressures with the new pumping efficiency. For each value of T_{rd} there is an opti-

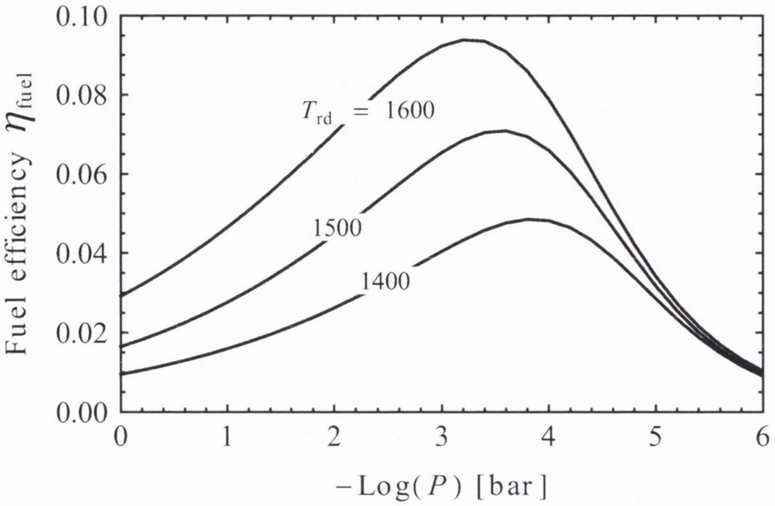

Figure 3.12: A plot of the η_{fuel} vs. -Log(P) for a range of values of T_{rd} (1400, 1500 and 1600 °C), with $T_{\text{ox}} = 1000$ °C, $P = P_{fO_2}$ and $\alpha = 0.95$.

mal operating pressure P and reducing the pressure further decreases the efficiency. The peak efficiency here is substantially higher than for ambient pressure operation and it has a lower P_{fO_2} meaning a better yield. For the results shown here $P = P_{fO_2}$ and no sweep gas was used. It was found that using a sweep gas as well as pumping only reduced the efficiency due to the high energy cost of producing the sweep gas.

Performing the reduction at lower than ambient pressure may have other benefits. Given that there is a net release of gas in the reduction reaction, there will be local pressure changes. These pressure changes can drive mass transport in the form of pressure wave propagation and pressure driven diffusion. Both of these processes should be more prominent at lower pressures as $\frac{\Delta P}{P}$ will increase. In addition if the ceria is formed into a porous monolith, which is often the case, the general diffusion gas phase mass transport also increases with decreasing pressure [140]. The reaction kinetics in a vacuum are very rapid, which can be seen in the previous work by the authors [138]. Many authors have measured much slower reaction kinetics at atmospheric pressure [105–109], which may be a result of restricted gas phase transport properties.

From this analysis we see that with some improvements to vacuum pumps, their use increases the efficiency as compared to using a sweep gas. The pumps pressure dependence means that there will be an optimal lower operating pressure to which the system should be pumped to during reduction. For the cycle conditions investigated here, optimal efficiency was around 7.5%.

3.3.3 Heat recovery

The heat used to change the temperature of the ceria ($Q_{\mathrm{CeO_2}}$) has, up till now, been disregarded as lost heat. As discussed earlier there have been a number of designs suggested for exchanging this heat from the hot reduced ceria to the relatively cooler oxidised ceria [58, 60, 137]. These designs greatly increase reactor complexity and introduce some difficulties. They involve bringing the reduced and oxidised ceria into close proximity, which allows them to exchange oxygen. The oxidised and reduced ceria have different equilibrium oxygen partial pressures and when exposed to the same atmosphere they will exchange oxygen until they reach equilibrium. This will result in a decrease in both efficiency and yield.

A much more simple and sensible approach would be to try convert the ceria heat $Q_{\mathrm{CeO_2}}$, into process heat. This would involve cooling the ceria in a heat exchanger which should be much easier to achieve. The efficiencies calculated so far have been quite low due to the heat cost of the other processes (Q_{pmp} and $Q_{\mathrm{H_2O}}$ for a pumped reactor), and thus heat recovery in this way could offer significant improvements without the complication of ceria to ceria heat recuperation.

There is also a small quantity of heat released during oxidation

$$Q_{\mathrm{ox}} = Q_{\mathrm{rd}} - \alpha \Delta\delta_{\mathrm{eq}} \mathrm{HHV}_{\mathrm{H_2}} \tag{3.32}$$

, some of which could be recovered and used as process heat. The amount of recovered heat is limited by the total heat required for the lower temperature processes giving

$$Q_{\mathrm{rec}} = \begin{cases} \varepsilon_{\mathrm{rec}}(Q_{\mathrm{ox}} + Q_{\mathrm{CeO_2}}) & : Q_{\mathrm{pmp}} + Q_{\mathrm{H_2O}} > \varepsilon_{\mathrm{rec}}(Q_{\mathrm{ox}} + Q_{\mathrm{CeO_2}}) \\ Q_{\mathrm{pmp}} + Q_{\mathrm{H_2O}} & : Q_{\mathrm{pmp}} + Q_{\mathrm{H_2O}} < \varepsilon_{\mathrm{rec}}(Q_{\mathrm{ox}} + Q_{\mathrm{CeO_2}}) \end{cases}, \tag{3.33}$$

for a pumped reactor, where $\varepsilon_{\mathrm{rec}}$ is the effectiveness of the heat recovery and $Q_{\mathrm{ox}} = Q_{\mathrm{rd}} - \alpha \Delta\delta_{\mathrm{eq}} HHV_{H_2}$. The fuel efficiency then becomes

$$\eta_{\mathrm{fuel}} = \frac{\eta_{\mathrm{plant}} \alpha \Delta\delta_{\mathrm{eq}} \mathrm{HHV}_{\mathrm{H_2}}}{Q_{\mathrm{rd}} + Q_{\mathrm{CeO_2}} + Q_{\mathrm{pmp}} + Q_{\mathrm{H_2O}} - Q_{\mathrm{rec}}}, \tag{3.34}$$

where the recovered heat Q_{rec} is subtracted from the other heat costs.

Figure 3.13 shows the effect of recovering 60% of the heat from the hot ceria and from the oxidation reaction. The maximum efficiency occurs at a sharp kink, which is when the recovered heat is just enough to cover the

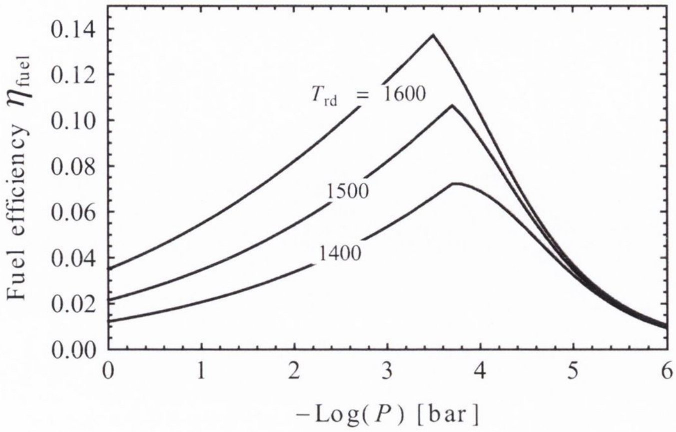

Figure 3.13: A plot of η_{fuel} vs. $-\log(P)$ for a range of values of T_{rd} (1400, 1500 and 1600 °C), with $\varepsilon_{\text{rec}} = 0.6$, $P = P_{fO_2}$, and $\alpha = 0.95$. The values of ΔT were 420, 520 and 580 °C respectively, which approximately optimised the efficiency.

lower temperature process heat ($Q_{\text{pmp}} + Q_{H_2O} = \varepsilon_{\text{rec}}(Q_{\text{ox}} + Q_{\text{CeO}_2})$). The efficiency was optimised with respect to ΔT and P giving a maximum of $\eta_{\text{fuel}} = 11\,\%$. The yield is also improved as the optimum pressure was lower when heat recovery was used.

3.4 Discussion

Calculations for CO_2 splitting gave very similar results to those seen for water splitting for temperature swing cycles. In general it required less CO_2 to oxidise the ceria and thus the efficiency was slightly higher. One drawback of CO_2 splitting is that a mixture of CO and CO_2 needs to be separated which was neglected in the calculations and would reduce the efficiency. Some select results for CO_2 splitting are presented in the appendix at the end of the chapter.

3.4.1 Quantities of ceria

As mentioned earlier the total quantity of ceria which must be used in a reactor may be one of the major technical challenges preventing the implementation of the ceria cycle on a large scale. For a plant with an output power of $\dot{Q}_{\mathrm{out}}$, the amount of ceria in moles per second which must be cycled is

$$\dot{n}_{\mathrm{CeO_2}} = \frac{\dot{Q}_{\mathrm{out}}}{\alpha \Delta\delta_{\mathrm{eq}} \mathrm{HHV}_{\mathrm{H_2}}} \quad [\mathrm{mol\,s^{-1}}], \tag{3.35}$$

and the total mass of ceria required per kilowatt output is given by

$$\frac{\partial m_{\mathrm{CeO_2}}}{\partial \dot{Q}_{\mathrm{out}}} = t_{\mathrm{cyc}} M(\mathrm{CeO_2}) \frac{\partial \dot{n}_{CeO_2}}{\partial \dot{Q}_{\mathrm{out}}} \quad [\mathrm{kg\ kW^{-1}}], \tag{3.36}$$

where t_{cyc} is the time it takes to complete one full cycle and $M(\mathrm{CeO_2})$ is the molar mass of ceria.

The time for one full cycle in the case of early prototypes was on the order of 50 min [93, 102]. For this reaction time, a cycle with $T_{\mathrm{rd}} = 1500$ °C, operating at atmospheric pressure with the optimum efficiency conditions found above and 50 % solid state heat recovery, would require 138 kg of ceria per kW output with a peak efficiency of around 7.5%. Asides from the technical challenges associated with handling such quantities of ceria, the fuel output from a reactor using 138000 kg of ceria would not suffice to power a Toyota Prius engine (150 kW) [141], operating in parallel. This would make scaling up of this technology infeasible in terms of both cost and practicality. In order to reduce the quantity of ceria, the cycle time must be greatly reduced and the yield improved.

The majority of the cycle time in these cases was spent on the reduction reaction. The kinetics of this reaction are very rapid [138], and thus this cycle time could be greatly improved upon. The yield can be improved by either increasing T_{rd} or decreasing $P_{f\mathrm{O}_2}$. If more efficient pumps could be developed the optimal $P_{f\mathrm{O}_2}$ would decrease, increasing both the efficiency and yield.

As a very optimistic pumping scenario, one might assume that pumps similar to transonic or supersonic axial flow compressor with very high efficiency could be developed. These pumps which are under research for the aeronautics industry could offer compression ratios of 1.6 per stage with an efficiency of 85 % per stage [142]. This would correspond to changing the pressure power factor in Eqn. 3.31 from 0.54 to 0.27. For a cycle with $T_{\mathrm{rd}} = 1500$ °C, $\varepsilon_{\mathrm{rec}} = 0.5$, $\varepsilon_{\mathrm{gas}} = 0.75$ and $C = 3000$, the maximised efficiency would then be approximately 16 %. If the the cycle time were 10 min this would give $\frac{\partial m_{CeO_2}}{\partial \dot{Q}_{\mathrm{out}}} = 7$ kg kW^{-1}, which is a great improvement. This improvement is due to the optimal P for the efficent pump being reduced to 10^{-5}, which greatly improves the yield. Pushing the reduction temperature to 1600 °C with the same cycle conditions gave an efficiency of around 21 % and $\frac{\partial m_{CeO_2}}{\partial \dot{Q}_{\mathrm{out}}} = 4$ kg kW^{-1}.

These findings may help to improve two step thermochemical fuel production cycles in general. For a given metal oxide cycle (MO_x), as well as the cost of the oxide, improving the efficiency and reducing $\frac{\partial m_{\mathrm{MO_x}}}{\partial \dot{Q}_{\mathrm{out}}}$ are likely the key issues which will decide the cycles success. If oxygen partial pressure must be reduced, then efficient vacuum pumps may be key to implementing the cycles.

These calculations neglect to take into account the use of dopants to improve the redox properties of ceria. The addition of both Zr and Hf to the ceria latice have been shown to increase the fuel production yield [106, 112]. These dopants also improve the high temperature stability of ceria allowing for a higher T_{rd}, meaning that such dopants could offer very significant improvements in η_{fuel} and n_{CeO_2}.

3.5 Conclusions

In this chapter the thermodynamics of CeO_2 thermochemical fuel production were analysed. For cycles operating at ambient pressure the maximum efficiency was found to be very low ($\approx 4.5\%$ for $T_{\text{rd}} = 1500$ °C) due to the very large amounts of sweep gas required to reduce the oxygen partial pressure. Isothermal cycles had very low efficiency under all conditions due to the excessive amounts of oxidiser required for the oxidation reaction.

The effect of performing the reduction at reduced pressures was investigated for pumps which have an efficiency that decreases with decreasing operating pressure. The results show the cycles have an optimal operating pressure and that using sweep gas as well as pumping only reduced the efficiency. Decreasing the pressure may offer other benefits. It improves the gas phase transport properties, which should improve the reduction kinetics. The optimal efficency, without solid state heat recovery, for a cycle operating at 1500 °C was found to be 7.5 %.

Instead of trying to recycle the heat from the ceria by exchanging it between hot and cold ceria, it is proposed this heat should simply be converted to process heat for powering the vacuum pumps and heating the oxidiser. With much more practical methods of heat recovery available, such as quenching the ceria in a heat exchanger this can offer significant efficiency gains.

Finally the amount of ceria which is needed per kW output power was investigated. For the normal cycle conditions considered, the amount of ceria required was extremely excessive and likely detrimental to any large scale implementation of this technology. Combined with the results of the efficiency, it seems that great improvements are needed if this cycle is to become competitive with more standard methods of renewable fuel production such as photovoltaic powered electrolysis. Some core technologies need to be developed, such as efficient vacuum pumps and high temperature heat exchangers for the oxidiser and for cooling the ceria. The use of dopants to improve both the yield and cycle time, would also improve both the efficiency and the practicality of the cycle.

3.6 Appendix

In this appendix the equilibrium oxygen partial pressure as a function of temperature in 1 bar of both H_2O and CO_2 is calculated. In addition the equlibrium concentration of fuel in the oxidiser is computed and some efficiency results for CO_2 splitting are given. Specific heat capacities are given in table 3.3 and standard Gibbs energy and enthalpy of formation are given in table 3.2.

$H_2O \longrightarrow H_2 + \frac{1}{2}O_2$	$\Delta H_f^\circ = 241.82$ [kJmol^{-1}]	$\Delta G_f^\circ = 228.61$ [kJmol^{-1}]
$CO_2 \longrightarrow CO + \frac{1}{2}O_2$	$\Delta H_f^\circ = 283.00$ [kJmol^{-1}]	$\Delta G_f^\circ = 257.23$ [kJmol^{-1}]

Table 3.2: Standard change in enthalpy and Gibbs free energy at 298 K and 1 bar (SATP).

3.6.1 Oxygen partial pressure in oxidiser

$$H_2O \longrightarrow H_2 + \frac{1}{2}O_2 \tag{3.37}$$

The equilibrium constant for the water splitting reaction isy

$$K_{\mathrm{ws}}(T) = \frac{x_{H_2} x_{O_2}^{0.5}}{x_{H_2O}}, \tag{3.38}$$

where x represents the mole fractions of each species, and K_{ws} is the equilibrium constant. The value of the equilibrium constant at SATP can be calculated using

$$K_{\mathrm{ws}}^\circ = \exp\left(\frac{-\Delta G_f^\circ}{RT}\right), \tag{3.39}$$

and the standard change in Gibbs energy given in table 3.2.

The temperature dependence of the equilibrium constant is

$$\ln\left(\frac{K_{\mathrm{ws}}(T)}{K^{\circ}_{\mathrm{ws}}}\right) = \int_{298\,K}^{T} \frac{\Delta H(T)}{RT^2} dT. \tag{3.40}$$

The temperature dependence of the change in enthalpy for water splitting can be determined from the energy required to raise the temperature of the steam compared to that of the products, which is

$$\Delta H(T) = \Delta H^{\circ}_{f} - \int_{298\,K}^{T} C_{p_{\mathrm{H_2O}}}(T) - C_{p_{\mathrm{H_2}}}(T) - \frac{1}{2} C_{p_{\mathrm{O_2}}}(T)\, dT. \tag{3.41}$$

Polynomial fits of the specific heat capacities are given in table 3.3.

$C_{p_{\mathrm{N_2}}}(T)$	$28.12 + 8.059 \times 10^{-4}\, T + 6.882 \times 10^{-6} T^2 - 3.871 \times 10^{-9} T^3 + 6.104 \times 10^{-13} T^4$
$C_{p_{\mathrm{O_2}}}(T)$	$25.38 + 1.458 \times 10^{-2} T - 6.210 \times 10^{-6} T^2 + 1.012 \times 10^{-9} T^3$
$C_{p_{\mathrm{H_2}}}(T)$	$29.99 - 3.818 \times 10^{-3}\, T + 5.335 \times 10^{-6}\, T^2 - 1.161 \times 10^{-9}\, T^3$
$C_{p_{\mathrm{CeO_2}}}(T)$	$37.10 + 0.113\, T - 1.19 \times 10^{-4}\, T^2 + 5.69 \times 10^{-6}\, T^3 - 9.62 \times 10^{-10}\, T^4$
$C_{p_{\mathrm{H_2O}}}(T)$	$31.43 + 3.332 \times 10^{-3}\, T + 1.115 \times 10^{-5}\, T^2 - 5.448 \times 10^{-9}\, T^3 + 7.543 \times 10^{-13}\, T^4$
$C_{p_{\mathrm{CO_2}}}(T)$	$20.99 + 6.768 \times 10^{-2}\, T - 4.960 \times 10^{-5}\, T^2 + 1.779 \times 10^{-8}\, T^3 - 2.495 \times 10^{-12}\, T^4$
$C_{p_{\mathrm{CO}}}(T)$	$28.98 - 3.412 \times 10^{-3}\, T + 1.480 \times 10^{-5}\, T^2 - 8.959 \times 10^{-9}\, T^3 + 1.655 \times 10^{-12}\, T^4$

Table 3.3: Polynomial fits of specific heat capacities C_p [$\mathrm{J\,mol^{-1}\,K^{-1}}$]. They were fit from 300 - 2300 K and the polynomial value was always within 1 % of the literature value [1, 2]

Using equations 3.39, 3.40 and 3.41, $K_{\mathrm{ws}}(T)$ can now be calculated for a given temperature. From the balanced reaction given in Eqn. 3.37 the mole fractions of hydrogen and steam can be defined as $x_{\mathrm{H_2}} = 2x_{\mathrm{O_2}}$ and

$x_{\mathrm{H_2O}} = 1 - 3x_{\mathrm{O_2}}$. These can be substituted into Eqn. 3.38 to get

$$K_{\mathrm{ws}}(T) = \frac{2x_{\mathrm{O_2}}^{1.5}}{1 - 3x_{\mathrm{O_2}}}. \tag{3.42}$$

Given that $x_{\mathrm{O_2}}$ at the temperatures considered (T < 2000 K) should be quite low, solving this condition iteratively once is enough to accurately determine $x_{\mathrm{O_2}}$.

$$K_{\mathrm{ws}}(T) = 2x'_{\mathrm{O_2}}{}^{1.5} \qquad x_{\mathrm{O_2}}(T) = \left(K_{\mathrm{ws}}(T)\frac{1 - 3x'_{\mathrm{O_2}}}{2}\right)^{-1.5} \tag{3.43}$$

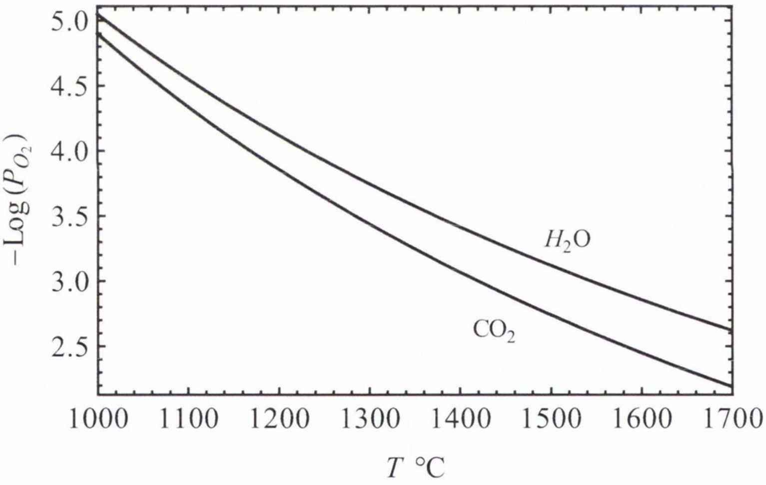

Figure 3.14: -Log($P_{\mathrm{O_2}}$) vs. temperature in 1 bar of steam and CO$_2$.

The same procedure can be followed to compute the oxygen mole fraction in CO$_2$ as a function of temperature. The oxygen partial pressure is then simply the mole fraction multiplied by the total pressure.

3.6.2 Oxidiser equilibrium

Here we calculate the amount of oxidiser required to re-oxidise the ceria. The Gibbs free energies must add up to that of water splitting at any given temperature giving

$$\Delta G_{\mathrm{ws}}(T) = \Delta G_{\mathrm{rd}}(T) + \Delta G_{\mathrm{ox}}(T). \tag{3.44}$$

The reactions equations are given by the following.

$$\mathrm{H_2O} \longrightarrow \mathrm{H_2} + \frac{1}{2}\mathrm{O_2} \tag{3.45}$$

$$\frac{1}{\delta_{\mathrm{rd}} - \delta_{\mathrm{ox}}}\mathrm{CeO}_{2-\delta_{\mathrm{ox}}} \longrightarrow \frac{1}{\delta_{\mathrm{rd}} - \delta_{\mathrm{ox}}}\mathrm{CeO}_{2-\delta_{\mathrm{rd}}} + \frac{1}{2}\mathrm{O_2} \tag{3.46}$$

$$\frac{1}{\delta_{\mathrm{rd}} - \delta_{\mathrm{ox}}}\mathrm{CeO}_{2-\delta_{\mathrm{rd}}} + \mathrm{H_2O} \longrightarrow \frac{1}{\delta_{\mathrm{rd}} - \delta_{\mathrm{ox}}}\mathrm{CeO}_{2-\delta_{\mathrm{ox}}} + \mathrm{H_2} \tag{3.47}$$

Using the Eqn. $\Delta G = -RT\ln(K)$ and the equilibrium constants

$$K_{\mathrm{rd}} = \frac{(a_{\mathrm{O_2}})^{\frac{1}{2}}(a_{\mathrm{CeO}_{2-\delta_{\mathrm{rd}}}})^{\frac{1}{\Delta\delta}}}{(a_{\mathrm{CeO}_{2-\delta_{\mathrm{ox}}}})^{\frac{1}{\Delta\delta}}} \qquad K_{\mathrm{ox}} = \frac{(a_{\mathrm{H_2}})(a_{\mathrm{CeO}_{2-\delta_{\mathrm{ox}}}})^{\frac{1}{\Delta\delta}}}{(a_{\mathrm{H_2}})(a_{\mathrm{CeO}_{2-\delta_{\mathrm{rd}}}})^{\frac{1}{\Delta\delta}}}, \tag{3.48}$$

we can write Eqn. 3.44 as

$$\Delta G_{\mathrm{ws}}(T) = -RT\ln\left(\frac{(a_{\mathrm{O_2}})^{\frac{1}{2}}(a_{\mathrm{H_2}})(a_{\mathrm{CeO}_{2-\delta_{\mathrm{rd}}}})^{\frac{1}{\Delta\delta}}(a_{\mathrm{CeO}_{2-\delta_{\mathrm{ox}}}})^{\frac{1}{\Delta\delta}}}{(a_{\mathrm{H_2O}})(a_{\mathrm{CeO}_{2-\delta_{\mathrm{ox}}}})^{\frac{1}{\Delta\delta}}(a_{\mathrm{CeO}_{2-\delta_{\mathrm{rd}}}})^{\frac{1}{\Delta\delta}}}\right). \tag{3.49}$$

Simplifying and subbing in the partial pressures for the activities gives

$$-RT\ln\left(\frac{P_{\mathrm{H_2}}}{P_{\mathrm{H_2O}}}\right) = \Delta G_{\mathrm{ws}}(T) + \frac{RT}{2}\ln(P_{\mathrm{O_2}}). \tag{3.50}$$

The equilibrium oxygen partial pressure during the reduction reaction is

$$P_{O_2}(\delta, T) = \left(\frac{8700(0.35 - \delta) \exp\left(\frac{-195.6 \ kJmol^{-1}}{RT} \right)}{\delta} \right)^{\frac{1}{0.217}} \quad [bar], \qquad (3.51)$$

which can be subbed in to Eqn. 3.50 to get the the equilibrium ratio between oxidiser and fuel for a given stoichiometry δ, and temperature T. The temperature will be T_{ox}, and we must considered the equilibrium state for a range of deltas.

$$\ln\left(\frac{P_{H_2}}{P_{H_2O}} \right) = \frac{-\Delta G_{\text{ws}}(T_{\text{ox}})}{RT} - \frac{1}{2} \ln(P_{O_2}(\delta, T_{\text{ox}})) \qquad (3.52)$$

From Eqn. 3.52 we get the equilibrium ratio between H_2 and H_2O to be

$$R_{\frac{H_2}{H_2O}}(\delta, T_{\text{ox}}) = \frac{P_{H_2}}{P_{H_2O}} = \exp\left(\frac{-\Delta G_{\text{ws}}(T_{\text{ox}})}{RT} - \frac{1}{2} \ln(P_{O_2}(\delta, T_{\text{ox}})) \right). \qquad (3.53)$$

The value of $\Delta G_{\text{ws}}(T)$ can be calculated using $K_{\text{ws}}(T)$ from the previous section, and the formula $\Delta G = -RT \ln(K)$.

3.6.3 CO_2 splitting

The same calculation shown above can be made to determine $R_{\frac{CO}{CO_2}}$. There are a number of other differences to consider when calculating the efficiency of CO_2 splitting. The value of δ_{ox} needs to be changed throughout the calculations, as CeO_2 has a lower equilibrium vacancy concentration in CO_2 compared to water. In addition the heat required to sustain the oxidation reaction becomes

$$Q_{\mathrm{CO}_2} = n_{\mathrm{CO}_2}(1-\epsilon_{\mathrm{gas}})\left(\int_{T_{amb}}^{T_{\mathrm{ox}}} C_{p\mathrm{CO}_2}(T)dT\right), \tag{3.54}$$

where $n_{\mathrm{CO}_2} = \dfrac{1}{\bar{x}_{\mathrm{CO}}}$.

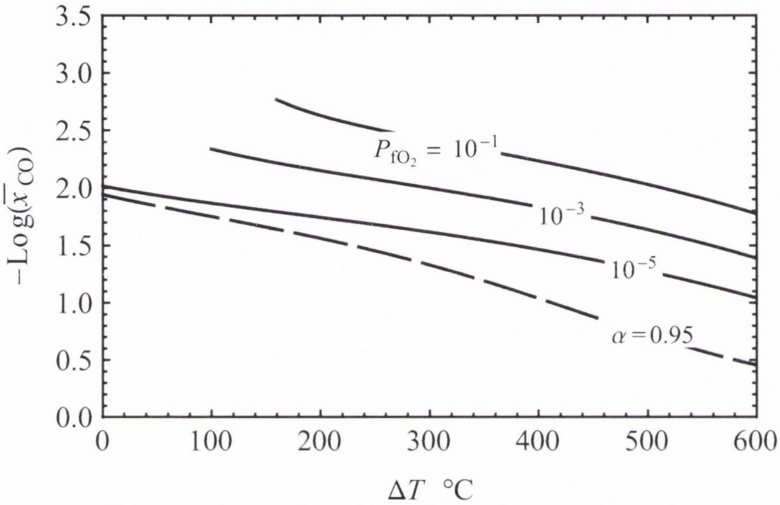

Figure 3.15: A plot of -log($\bar{x}_{\mathrm{CO}}$) vs. the change in temperature ΔT. The solid lines are different values of $P_{f\mathrm{O}_2}$ (10^{-1}, 10^{-3} and 10^{-5} bar) with T_{rd} = 1500 °C. The dashed line shows the effect of stopping the oxidation reaction before equilibrium at 95 % completion, with T_{rd} = 1500 °C and $P_{f\mathrm{O}_2} = 10^{-5}$ bar.

The calculation of $\bar{x}_{\mathrm{CO}}$, was performed the same as that for $\bar{x}_{\mathrm{H}_2}$, except using $R_{\frac{\mathrm{CO}}{\mathrm{CO}_2}}$ and δ_{ox} in CO_2. This resulted in less oxidiser which can be seen by comparing Fig. 3.5 to Fig. 3.15. In general this gave slightly greater fuel production efficiency, which can be seen in Fig. 3.16. This is neglecting the fact that the product stream is a mixture of CO_2 and CO which needs to be separated, causing a decrease in the efficiency.

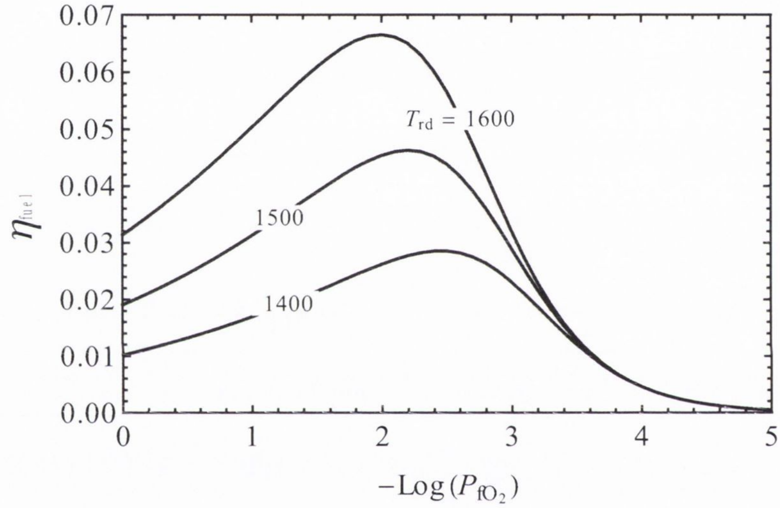

Figure 3.16: A plot of the η_{fuel} vs. $-log(P_{f\text{O}_2})$ for a range of values of T_{rd} (1400 1500 and 1600 °C), with $P = 1$ bar, $\Delta T = 500$ °C, $\alpha = 0.95$ amd using CO_2 as the oxidiser.

Chapter 4

Experimental oxidation and reduction

In this chapter, experimental results of the oxidation and reduction of cerium dioxide are presented. The results were obtained using the same system described in chapter 2, but with some modifications. A new shutter was added which allowed for more reproducible reduction and oxidation heating curves. Ceria samples, produced by the author, with both Zr and Hf dopants were investigated. The samples were analysed using XRD, SEM and the system built by the author for oxidation and reduction cycles. From XRD it was confirmed that the dopants were indeed incorporated into the ceria lattice, and in combination with SEM analyses, the addition of Zr and Hf was seen to improve the high temperature stability of the samples. The experimental oxidation of the samples showed that the dopants reduced the oxidation rate. Arrhenius plots suggested that the activation energy was decreasing with increasing dopant concentration, but that the frequency factor was also drastically decreasing; resulting in slower oxidation kinetics.

The oxidation and reduction kinetics of Zr doped ceria samples from the DLR were also investigated. These samples were annealed at higher temperatures and thus lower activity was expected as a result of more sintering. This was indeed the case with oxidation rates much slower than the samples produced by the author. However, there was a wider range of doping concentrations and the trend of decreasing oxidation kinetics for increasing Zr concentration was again observed. Finally reduction of these samples was reproducible enough to suggest that the reduction kinetics were simply limited by the temperature increase.

4.1 Introduction

As discussed in Chapter 1 Section 1.4.3, the introduction of dopants into the ceria lattice can change its redox properties. Doping ceria with ions which have the same valence, but lower ionic radius, such as Zr^{4+} and Hf^{4+}, has been shown to increase the reducibility of ceria [106–110]. This means that the addition of Zr and Hf dopants increases the equilibrium vacancy concentration $\delta(P_{\mathrm{O}_2}, T)$.

In Chapter 2 it was shown that the literature equilibrium data could be described using the balanced reaction equation

$$\frac{d\delta}{dt} = (\delta_{max} - \delta) A_{rd} \exp\left(\frac{-E_{rd}}{RT}\right) - \delta P_{O_2}^{\,n} A_{\mathrm{ox}} \exp\left(\frac{-E_{\mathrm{ox}}}{RT}\right) = 0. \qquad (4.1)$$

Thus, if dopants change the equilibrium oxygen vacancy concentration δ, they must also be changing the reaction kinetics in some way. For example; if the addition of dopants decreased the rate of oxidation, but left the rate of reduction unchanged, then the equilibrium $\delta(P_{O_2}, T)$ would be greater than that of pure ceria.

In this chapter we discuss experimental results aimed at determining the effect that Zr and Hf dopants have on the reaction kinetics.

4.2 Experimental techniques

4.2.1 Powder diffraction

Powder diffraction or X-ray diffraction is a technique used to characterise materials. The principle is the same as single crystal x-ray diffraction, except that every crystal orientation is represented in the scan.

In x-ray diffraction the position of the peaks for a given crystallographic orientation can be determined using Bragg's law [143].

$$n\lambda = 2dsin(\theta) \tag{4.2}$$

For a crystalline powder, every orientation should be present and thus a scan varying θ should give different peaks corresponding to the different lattice orientations. Analysis of the peak positions, relative intensities and peak widths can provide a lot of information about materials. This can include the crystal structure, the lattice parameters, the particle size and/or the amount of disorder in the crystal.

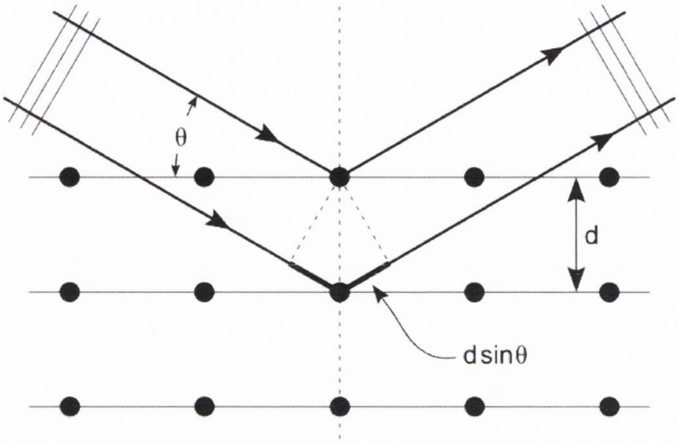

Figure 4.1: A schematic showing the principle behind Bragg's law. Constructive interference leads to peaks at the positions described by Eqn. 4.2

The scans presented in this work were performed using a Bruker D8 x-ray diffraction system (Cu K-α with monochromator).

4.2.2 Scanning Electron Microscopy

In order to look at the morphology of the samples they were imaged with a scanning electron microscope. A focused beam of electrons incident on the sample is used to produce a raster scan of the surface. The beams position is combined with the a detected signal to produce an image showing the topography of a surface. The signal detected is produced by secondary electrons emitted from the sample surface.

Typically when examining non conductive materials they must be treated before performing SEM scans. However, although ceria is a ceramic, it was found that simply using low operating voltage in the system allowed the samples to be imaged without charging effects. The images shown in this work were taken using a Zeiss Ultra Plus - SEM.

4.2.3 Sample preperation

Samples were prepared by pressing the required oxides into pellets and annealing them in the same way described in Chapter 2 Section 2.3. The oxide powders used were CeO_2, ZrO_2 and HfO_2. They were all obtained from Sigma-Aldrich and their specifications are given in Table 4.1. In addition, graphite powder was used as a pore former. This was achieved by mixing the graphite with the oxide powders before making the pellets. The graphite then undergoes auto-combustion during annealing leaving void space within the pellets. The specifications of the graphite powder used are also given in Table 4.1.

Material	Supplier	SUK	Purity	Particle Size
CeO_2	Sigma-Aldrich	544841	Not given	< 25 nm
ZrO_2	Sigma-Aldrich	544760	Not given	< 100 nm
HfO_2	Sigma-Aldrich	202118	98 %	Not given
Graphite	Sigma-Aldrich	282863	Not given	< 20 μm

Table 4.1: Specifications of the different materials used for preparing the samples

Doping was achieved by mixing the CeO_2 nano-powder with the desired amount of dopant oxide powder; either ZrO_2 or HfO_2. The mixture was placed in a sealed beaker with polished steel ball bearings (5mm diameter) and then sonicated in an ultrasonic bath for 30 min. After this step the appropriate amount of graphite was added for the desired porosity and the mixing procedure was repeated. A 5 mm diameter Specac pellet die was used to press the mixture into pellets which were then annealed for 3 hrs at 1000 °C to remove the graphite, followed by 24 hrs at 1500 °C to sinter the oxides together. Both annealing steps were conducted in the same furnace with the temperature increasing to 1000 °C, stopping there for 3 hours, followed by a temperature increase to 1500 °C for 24 hrs before cooling down. As discussed in Chapter 1 Section 1.4.3 ceria has a very accommodating lattice for these particular dopants [111]. In fact, in the results it is seen that simply annealing the mixtures of oxide nano-powders as described here, is enough to incorporate the dopants into the ceria fluorite structure.

One notable issue was that during the annealing process the samples shrank losing some of their void space. Table 4.2 shows the volume shrinkage of a number of samples which were produced, but not used in the experiments. For each sample the volume and density of three different pellets were measured and the results were averaged. The target void space is the initial percentage of the filled pellet volume which was graphite. During annealing, the pure ceria samples collapsed more than the doped samples, which suggests that the doped samples had better stability at high temperatures. This is in agreement with the study of ceria catalysts which showed that addition of Zr improved the thermal stability [144].

The final samples used for the results presented made allowances for this collapse by using more graphite in the pure ceria samples than in the doped samples. The final void space of all the samples, determined by measuring the mass and volume of the pellets, was in the range 69 - 72 %. Therefore, it is assumed that the differences in void space from sample to sample would have a negligible effect on the reaction kinetics.

Sample	Target v.s.	Void space	Volume shrinkage
CeO_2	60 %	50.6 ± 1.7 %	9.4 %
CeO_2	75 %	63.8 ± 1.9 %	11 %
$Ce_{0.9}Zr_{0.1}O_2$	60 %	56.2 ± 1.8 %	3.8 %
$Ce_{0.9}Zr_{0.1}O_2$	75 %	70.5 ± 2 %	4.5 %
$Ce_{0.8}Zr_{0.2}O_2$	60 %	56.4 ± 1.8 %	3.6 %
$Ce_{0.8}Zr_{0.2}O_2$	75 %	70.9 ± 1.9 %	4.1 %

Table 4.2: Table showing the target void space, the actual void space and the volume shrinkage of the samples after being annealed for 24 hrs at 1500 °C.

4.2.4 Oxidation and reduction measurements

The investigation of oxidation and reduction reactions was performed using a custom built system constructed by the author. This system was described in Chapter 2 Section 2.3, but a number of changes were made for the experiments presented in this section. A shutter was added to the system which uncovers the beam emitted from the Xenon arc lamp at a controlled speed. The shutter is just an electrical linear drive with a sheet of steel (the shutter) attached to it and extending it in front of the lamps beam. A number of shutter speeds can be selected, uncovering the lamps beam at different rates and thus allowing for control of the rate of temperature increase.

For the experiment described in Chapter 2 the samples were simply heated with a constant power, resulting in a rapid temperature increase. When the shutter is used, the power incident on the sample is increasing with time, giving a more gradual and reproducible temperature increase curve. This

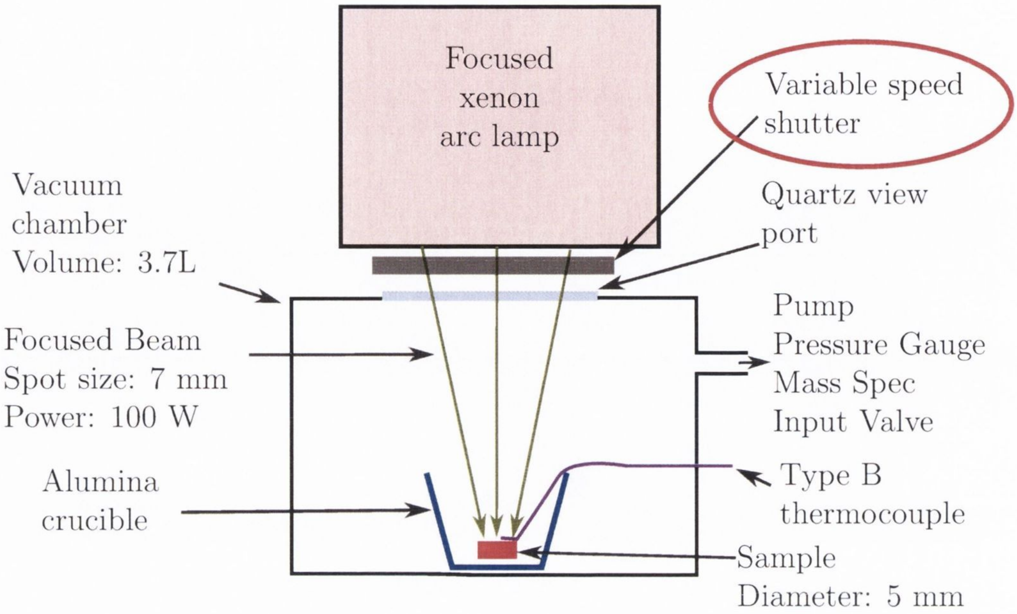

Figure 4.2: A schematic showing the system with the added variable speed shutter.

should allow for a more accurate look at the effects of temperature on the rate of reaction. The shutter can also be left in place until the plasma of the lamp stabilises (30 seconds after ignition) resulting in less fluctuations of the power output of the lamp.

In Fig. 4.3 we see the temperatures recorded with and without the variable speed shutter. The red line shows the typical radiative heating curve which is very steep initially, but which levels off quite rapidly as the temperature nears equilibrium. The time over which the temperature is changing is very brief, giving limited data for Arrhenius plots. However, the three temperature increase rates shown for the shutter have a more gradual temperature increase and should be easier to analyse. In addition, as the rate of

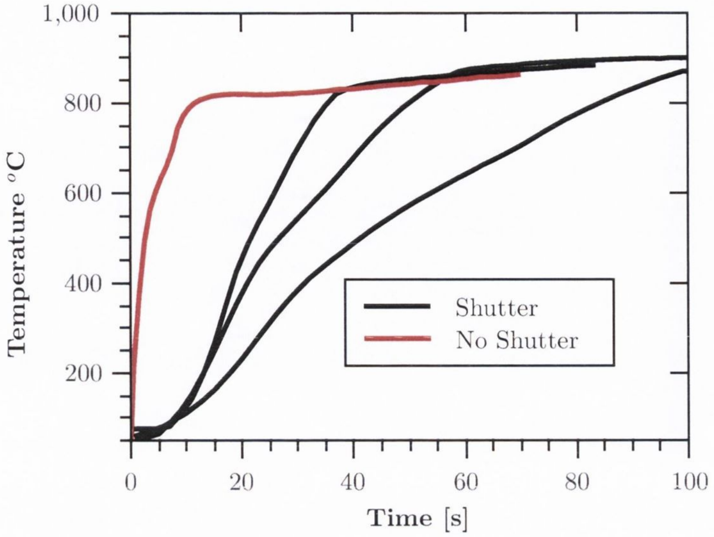

Figure 4.3: Temperature vs. time for oxidation heating rates, with and without the shutter. The three black lines show the temperature increase profile for three different shutter speeds.

change of temperature is smaller there is less likely to be large temperature gradients within the sample.

The system also has a number of novelties when compared to other experimental methods used for the analysis of the ceria redox cycle. For example reduction and oxidation using a thermo-balance is usually restricted to temperature increase rates of the order 20 - 50 °C min^{-1} [107, 112], where as the system described here can achieve temperature increase rates in excess of 100 °C s^{-1}; which is hundreds of times faster than is possible with a thermo-balance.

Another example of the unique nature of the system is the gas phase transport properties. Most experimental measurements of oxidation and reduction are performed at atmospheric pressure and use a sweep gas to remove reaction products [106, 107, 112]. During reduction oxygen must diffuse away from the region of ceria at which it is produced. In the case of porous pellets (or even dense pellets) this diffusion may be slow, even when a sweep gas is used to remove the oxygen. The diffusion coefficient in a gas is proportional to the inverse of the pressure.

$$D \propto \frac{1}{P} \tag{4.3}$$

In this work both oxidation and reduction take place at less than 20 Pa as opposed to 10^5 Pa, resulting in much faster diffusion rates. In addition oxygen released during reduction or absorbed during oxidation accounts for a significant amount of the total gas in the chamber. This means that gas phase transport is also driven by pressure gradients generated when oxygen is released or absorbed by the sample. Pressure gradients could disperse the gases as fast as the speed of sound. For these reasons it is very unlikely that gas phase transport will in anyway restrict the kinetics measured in this work. In other analysis techniques, such as using a thermo-balance, gas phase transport is likely to play a very important role in the kinetics.

Figure 4.4 shows a photograph of the experimental apparatus. There are two chambers, the main chamber where the sample is placed and the mass spectrometer chamber which is pumped to lower pressure and receives a small leak of gas from the main chamber. The pressure in the main chamber is monitored using a capacitance manometer. In addition there is an oxygen supply and a type B thermocouple as shown in the photograph.

The procedure outlined in Chapter 2 Section 2.3, is repeated here including more details on the use of the variable speed shutter.

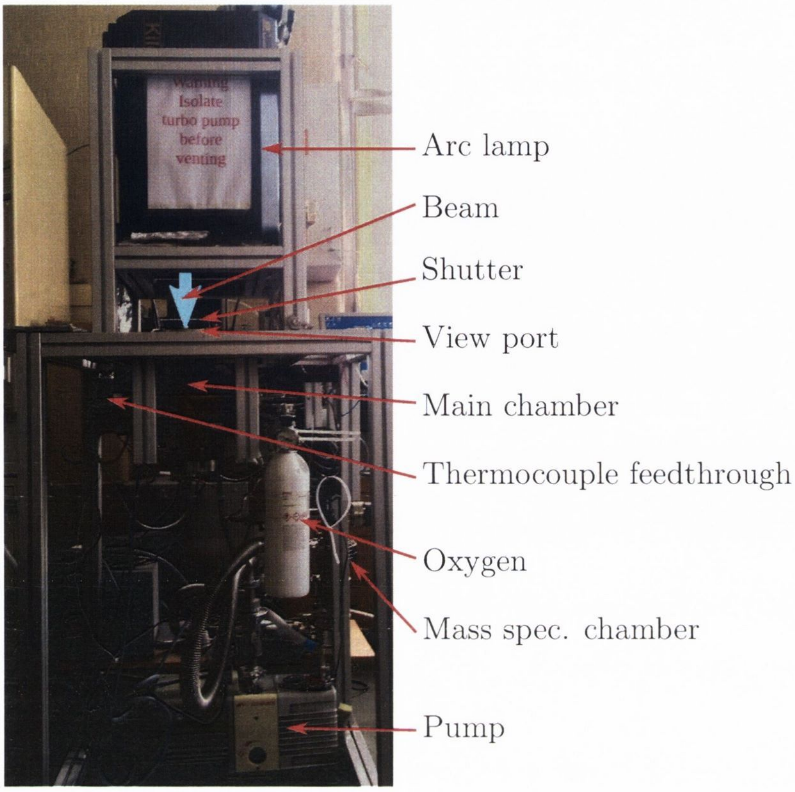

Figure 4.4: A photograph of the system showing many of the components.

A reduction cycle is started by pumping the chamber down to 1 Pa, and then sealing the chamber off from the pump. The lamp is then switched on and the shutter is activated which uncovers the beam and heats the sample to high temperatures of approximately 1600 °C. The changes in sample temperature, gas temperature, pressure and gas composition are all recorded once per second.

At the end of the reduction the system is again pumped to remove oxygen. The chamber is then sealed and the sample is allowed to cool for 40 min reaching approximately 30-40 °C. This is to ensure that the sample is cool enough to prevent the oxidation reaction beginning immediately on the introduction of oxygen into the system.

A re-oxidation cycle may then be conducted by first flushing the system with oxygen twice to remove other gases, and then filling with oxygen and pumping down to a pressure value of 15 Pa. The sample is then heated using the Xenon lamp where the input power reduced by a filter and the shutter slowly uncovering the beam. The changes in temperature, pressure and gas composition are again recorded.

The background pressure increase due to heating of the chamber without a sample present were taken into account by running oxidation and reduction cycles with no sample present. In the case of the re-oxidation cycles, the power incident into the chamber is relatively moderate and the increase in pressure is negligible.

4.3 Experimental Results

4.3.1 XRD

The annealed pellets were scanned using the standard 2θ powder scan. A scanning step size of 0.01 degrees was used and a scan range from 24 - 120 degrees was taken. Each scan took approximately 14 hours, which was required in order to get a good signal to noise ratio.

A portion of the scans for the Zr doped samples are shown in Fig. 4.5. All three samples show the cubic fluorite structure of CeO_2 [145]. In addition, the introduction of Zr (ionic radius = 85 pm) instead of Ce (ionic radius =

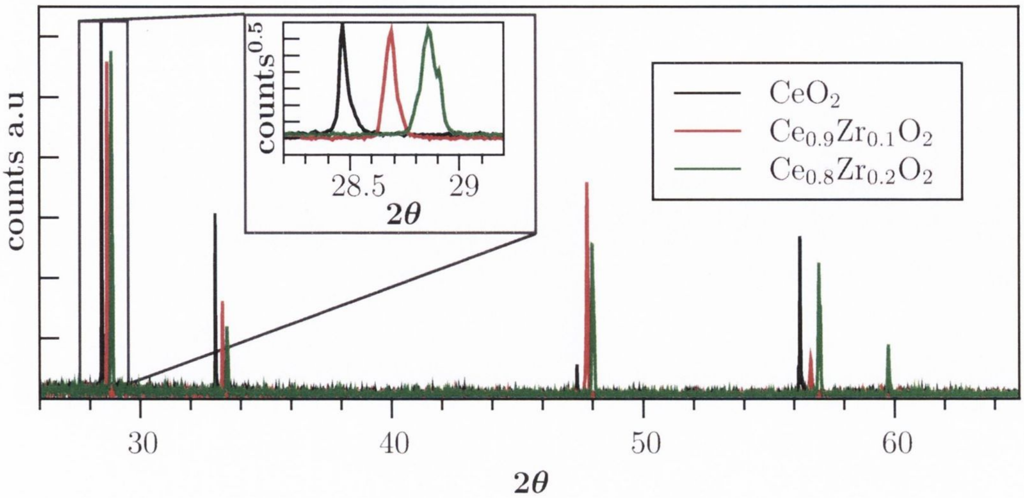

Figure 4.5: XRD scans of Zr doped samples and pure ceria.

101 pm) [146], shifts the peaks to the right. This can be explained by the smaller ionic radius of Zr as reducing the d in Eqn. 4.2, where since λ is constant, and thus θ must increase to satisfy Eqn. 4.2. Just such a change in the lattice spacing is predicted by Vegard's law [147], and has been observed by other authors [148]. This offers strong evidence that the Zr in the pellets has replaced some of the Ce in the ceria lattice.

The same section of the scans is shown for the Hf doped samples in Fig. 4.6. The ionic radius of Hf (85 pm) is again smaller than that of Ce and very close to that of Zr [146], so we expect the peaks to shift in a similar way to those seen for Zr doping. The peaks also show more broadening than the Zr doped samples. This suggests there is more disorder in the lattice, and a closer look at the main peak of $Ce_{0.8}Hf_{0.2}O_2$ appears to show 3 separate peaks combining to make one broad peak. Therefore, the broadening is likely caused by having more than a single concentration of Hf in the sample and thus secondary phases.

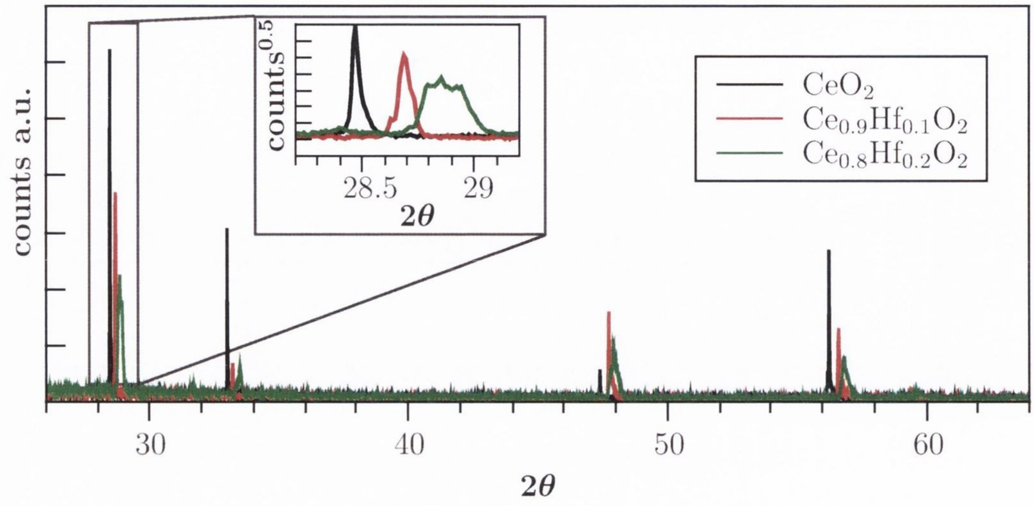

Figure 4.6: XRD scans of Hf doped samples and pure ceria.

Analysis of the scans was carried out with the XRD software MAUD [149], which uses the standard Rietveld refinement method to fit the diffraction spectra [150]. The fits can be used to extract information on the lattice parameter and average crystal size. However, the crystal size is obtained from the peak widths, which can also be affected by disorder in the lattice. It is still convenient to show the extracted crystal size as it can be be taught of as a measure of the peak broadening due to lattice disorder.

The lattice parameters determined from the XRD scans were in agreement with those predicted by Vegard's law, as seen in Table 4.3. The crystal size decreases upon addition of Zr into the ceria lattice. This shows that the addition of Zr introduces some extra disorder into the lattice which may or may not be as a results of smaller crystal sizes. However, the high temperature stability of CeO$_2$ is improved by the addition of Zr dopants [144], and thus these samples may have underwent less sintering during the annealing process.

Sample	$\bar{r}_A$ [pm]	Vegard's a [Å]	a [Å]	Crystal size [nm]
CeO_2	117.67	5.421	5.421	980 ± 170
$Ce_{0.9}Zr_{0.1}O_2$	117.167	5.383	5.383	970 ± 160
$Ce_{0.8}Zr_{0.2}O_2$	116.67	5.344	5.353	600 ± 30
$Ce_{0.9}Hf_{0.1}O_2$	117.13	5.382	5.383	260 ± 7
$Ce_{0.8}Hf_{0.2}O_2$	116.6	5.342	5.357	180 ± 6

Table 4.3: Table showing the average ionic radius of the atoms in the material $\bar{r}_A$, the lattice parameter predicted by Vegard's law, the lattice parameter determined from the Rietveld fit and the average crystal size determined from the peak width.

For the Hf doped samples the average crystal size was much smaller. As explained previously, this fit may not be attributed to size effects alone and these values cannot be interpreted as the actual crystal size. The multi-peak structure of each peak suggests that there is more disorder (multi-phases) in the samples and thus the average crystal size cannot be determined in any confidence from the XRD fit.

In summary, the smaller ionic radius of the Zr and Hf dopants contracts the ceria crystal lattice. There is an arbitrary aspect to the determination of the crystal size, which does not account for disorder, or regions of different concentration. Thus, it cannot be concluded from XRD that the high temperature stability of the samples is improving with doping.

4.3.2 SEM

The scans presented here were taken using a secondary electron detector, with a beam bias of 4 kV. Results from these scans allow us to see the morphology of the samples. In particular, they give a picture of the porous structure of the samples.

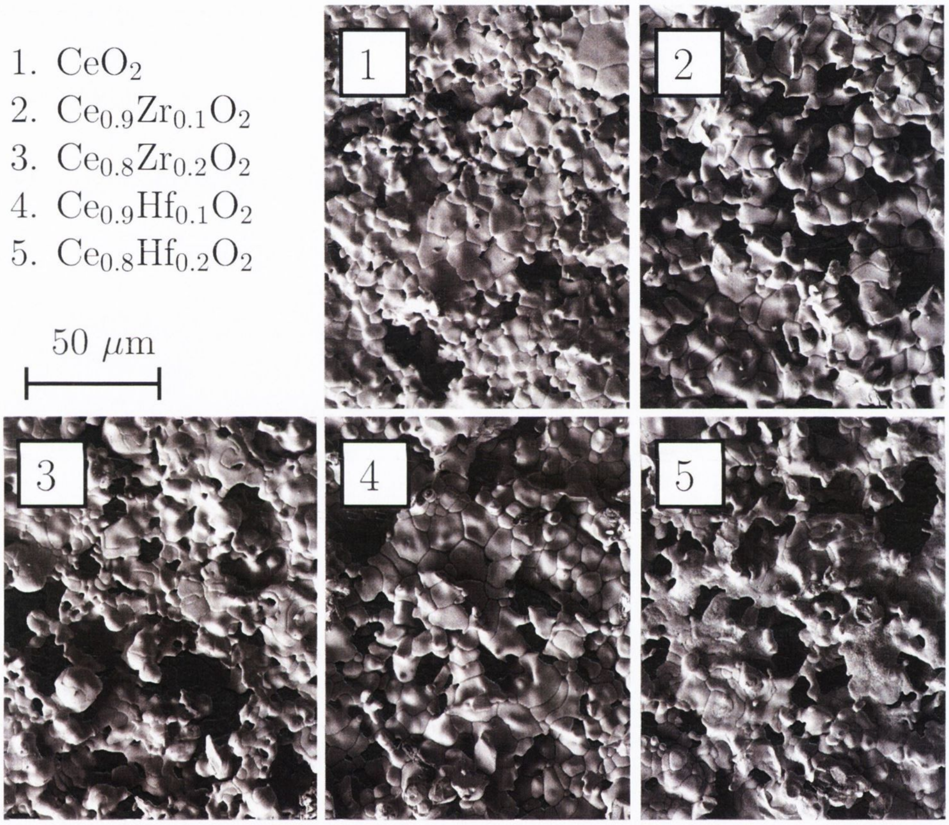

Figure 4.7: SEM micro graphs of the different samples showing their porous structure.

Figure 4.7 shows the different samples and their porosity, with the doped samples appearing to have a more robust porous structure. This is in agreement with the the sample preparation which suggesting the doped samples underwent less shrinkage during annealing. These results suggest that the dopants improve the high temperature stability of ceria. This is a large benefit as the material must maintain its reactivity over thousands of cycles if it is to be used in fuel production cycles.

Comparing these SEM images to the sample shown in Chapter 2 Fig. 2.8 we see that the overall porous structure and grain size is smaller. For the pure ceria sample shown here, the grain-like structure appears to be approximately half the size of that shown in Fig. 2.8. This is likely due to inconsistencies in the furnace used. The furnace elements and the thermocouple degrade over time and are replaced regularly. Thus the accuracy of the set temperature can vary, and a small difference in temperature could have a large effect on the sintering over 24 hrs. However, this is not an issue if the model is correct as it should only result in a change to the frequency factors due to the change in surface area; and the activation energy should still be the same.

4.3.3 Oxidation results

As described in Chapter 2 Section 2.2.2, the oxidation reaction is more convenient to examine. The reduction in the system appears to only be limited by the heating rate, which is illustrated later.

We would like to look at the effect of the dopants on the reaction rate. The heating rates were much more reproducible so we can directly compare oxidation rates for samples which were subject to the same heating rate.

Figure 4.8 shows the oxidation rate for the different samples. From this it can be seen that the addition of Zr and Hf dopants reduces the oxidation rate, and it reduces further for increasing dopant concentration. This is despite

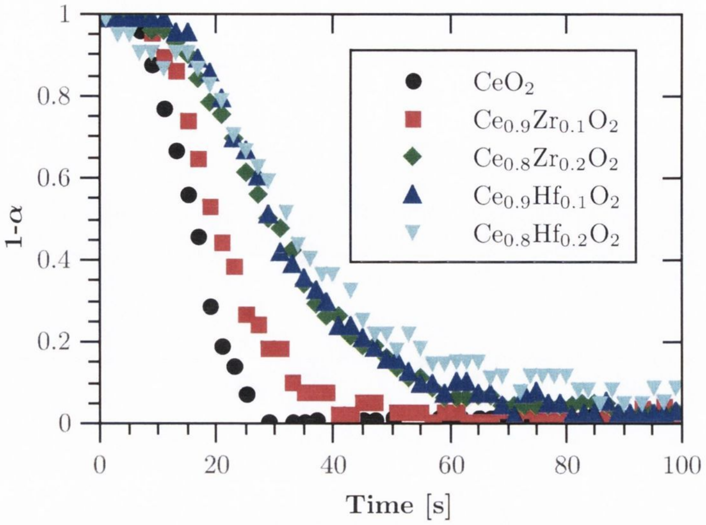

Figure 4.8: The fraction of remaining vacancies $(1-\alpha)$ vs. time for the different samples, all of which were heated with the steepest (black) heating curve shown in Fig. 4.3.

XRD and SEM results suggesting that these doped samples should have a higher surface area.

If compared to the oxidation rates in Chapter 2, the pure ceria oxidises faster here. This is most likely due to the higher surface area due to less sintering as seen in the SEM results. This should show up in the kinetic results as an increased frequency factor (A_{ox}), and should not change the activation energy (E_{ox}).

In these experiments the samples were heated with a more controlled temperature increase. In Chapter 2 the samples quickly reached steady state temperature after which point the data is no longer useful for Arrhenius plots as the temperature is no longer changing. This is one of the reasons why oxidation up to only 50 % complete was considered. Instead here the sample temperature is changing throughout the reaction and it should be possible to use all of the data for the Arrhenius plots. Consider again the oxidation rate equation.

$$\frac{d\delta}{dt} = -(1-\alpha)^{x}\delta P_{O_2}^{\,n} A_{\text{ox}} \exp\left(\frac{-E_{\text{ox}}}{RT}\right) \tag{4.4}$$

Previously we did not use the $(1-\alpha)^x$ term to account for diffusion in the analysis, as it was assumed that it would not have a strong effect at the initial stage of the reaction considered. However, diffusion must be approximated in some way if the entire reaction is to be analysed. The data can be plotted according to the following equation.

$$\ln\left(\frac{-(1-\alpha)^{-x}}{\delta P_{O_2}^{\,n}}\frac{d\delta}{dt}\right) = \frac{-E_{\text{ox}}}{RT} + \ln(A_{\text{ox}}) \qquad \ln(k) = \frac{-E_{\text{ox}}}{RT} + \ln(A_{\text{ox}}) \tag{4.5}$$

The value of x in the $(1-\alpha)$ term was set to $\frac{1}{3}$ in Chapter 2. In this section the plots were made for various different values of x to see what gave the best straight line. The best value was approximately $x = 1$, which implies that diffusion plays a more important role than previously considered.

Each sample was reduced and re-oxidised six times, twice for each temperature increase curve. Figure 4.9 shows the linear fits for each sample. There are approximately fifty data points per sample and the temperature range covered is larger than that seen in Chapter 2 Fig. 2.10, and thus the results here should be more accurate.

It is notable that activation energy for pure ceria E_{ox}, is within the error of that found in Chapter 2 despite the overall rate being much faster. This sup-

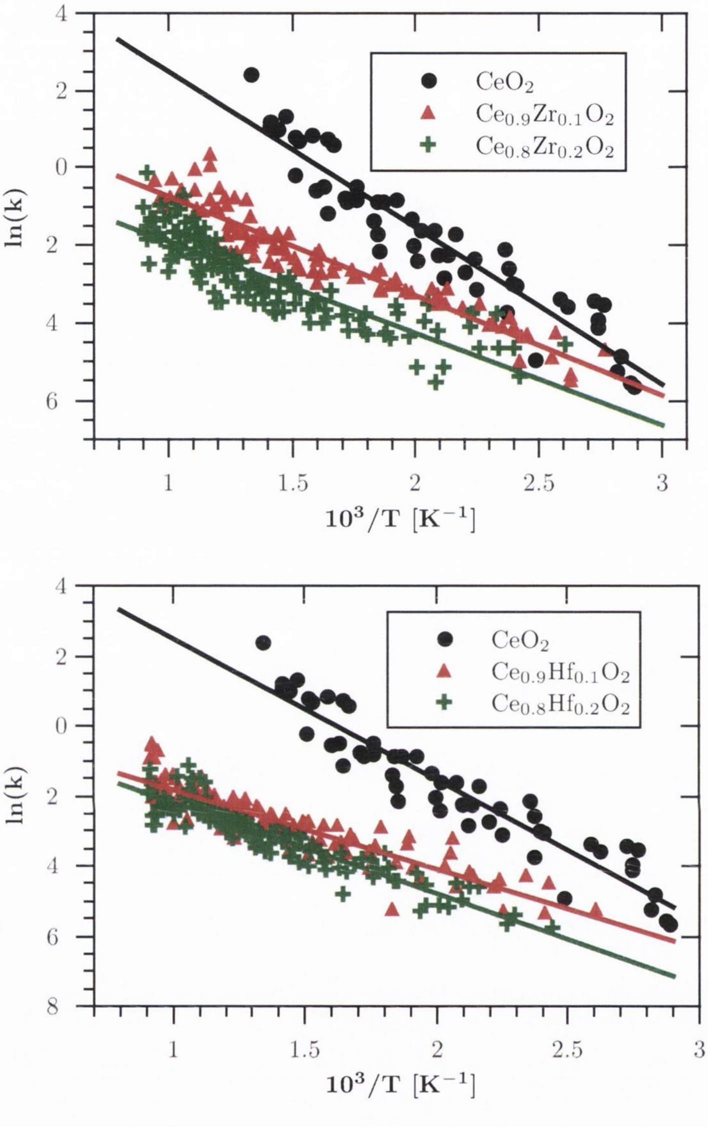

Figure 4.9: Arrhenius plots and linear fits of oxidation for the different samples. The slope of each fit is $-E_{\text{ox}}$ and the intercept is $\ln(A_{\text{ox}})$.

ports our analysis method. The frequency factor drastically increased, which is expected as a result of the samples being less sintered and thus having a higher surface area ($A_{\text{ox}} \propto$ Surface area). The error in the frequency factor is quite large, which could be a result of the samples undergoing sintering during the reduction.

Sample	E_{ox} [kJ mol^{-1}]	A_{ox} [s^{-1}]
CeO_2	33.5 ± 3	680 ± 600
$Ce_{0.9}Zr_{0.1}O_2$	21.3 ± 2.5	6.3 ± 3
$Ce_{0.8}Zr_{0.2}O_2$	19.7 ± 2.5	1.6 ± 1
$Ce_{0.9}Hf_{0.1}O_2$	18.9 ± 2.5	1.6 ± 1
$Ce_{0.8}Hf_{0.2}O_2$	21.2 ± 2.5	1.5 ± 1

Table 4.4: Slope and intercept data of each linear fit giving E_{ox} and A_{ox}.

Interestingly, it seems from the analysis that the dopants reduce the activation energy, but also greatly reduce the frequency factor. This could be due to Zr atoms at the surface reducing the available reaction areas. There could even be an accumulation of Zr at the surface. Preliminary XPS results suggest this, but a full analysis of all the samples is required and it is only mentioned here as a speculative reason for the reduced frequency factors.

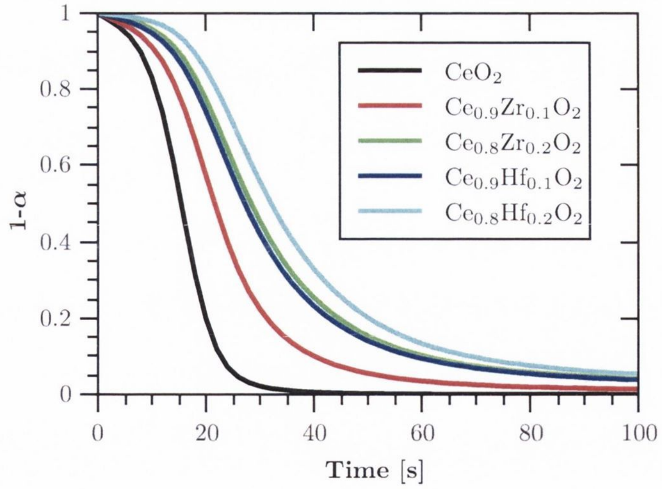

Figure 4.10: The fraction of remaining vacancies $(1 - \alpha)$ vs. time calculated using the determined parameters and the same heating curve as Fig. 4.8.

Putting the temperature curve and initial δ back into Eqn. 4.4, along with the determined reaction parameters, should result in similar rates to those seen Fig. 4.8. This can be seen in Fig. 4.10 which is indeed very similar to the experimentally measured rates for each sample.

4.4 DLR samples

Other samples produced at the German Aerospace Center (DLR) in Cologne by Friedemann Call and his colleagues were also investigated. The samples were of the form $Ce_{1-x}Zr_xO_2$, with x varying from 0 - 0.3 in steps of 0.05.

4.4.1 Synthesis

The production of the oxide powders was as follows: Desired amounts of Ce^{3+} nitrate (99.9 % purity, Merck) and Zr^{4+} oxynitrate hexahydrate (99.99 % purity, Sigma Aldrich) were dissolved in deionised water using a reaction vessel made of quartz. Citric acid (99 % purity, Merck), also dissolved in deionised water, was added to the nitrates in a molar ratio of 1:2 (cations:citric acid). Water evaporation at 95 °C on a heating plate under continuous stirring yielded a yellow coloured gel. Heating this gel to 200 °C for 20 minutes resulted in a swollen foam exhibiting a very low density. During slow heating to 500 °C, auto combustion took place leaving a fine oxide powder in the reaction vessel. Subsequent calcination in the reaction vessel in a muffle furnace at 800 °C for 1h under air ensured the removal of remaining carbonaceous species. Further calcination at 1400 °C for 1 h in a Pt crucible completed the synthesis route. For each composition two batches were synthesised to guarantee reproducibility.

The synthesised doped oxide powders were then mixed with a pore former (Poly Ethylene Glycol) and pressed into pellets using a 5 mm diameter pellet die. These pellets were then annealed at 1000 °C to remove the pore former, followed by annealing at 1650 °C for two hours to induce sintering. The final porosity of the samples were in the range 55-60%. Note that these samples were sintered at higher temperature than the samples produced by the author (1500 °C) which likely caused the lower porosity in comparison to the authors samples (70 %).

4.4.2 Oxidation and reduction

The samples produced by the DLR typically weighed around 45–50 mg compared to the 30 mg samples produced by the author. These larger samples cause a greater change in pressure in the system which gives higher resolution for the recorded pressure change. Currently characterisation data is being collected for these samples, such as XRD, SEM and XPS, however the results obtained for oxidation and reduction help to illustrate a few points.

Oxidation

The larger change in pressure means the signal to noise ratio is better for these samples. Figure 4.11 shows the typical temperature and pressure measurements for a reduction and oxidation cycle. As we can see the data has less noise than that shown in both Fig. 4.8 and Chapter 2 Section 2.4.

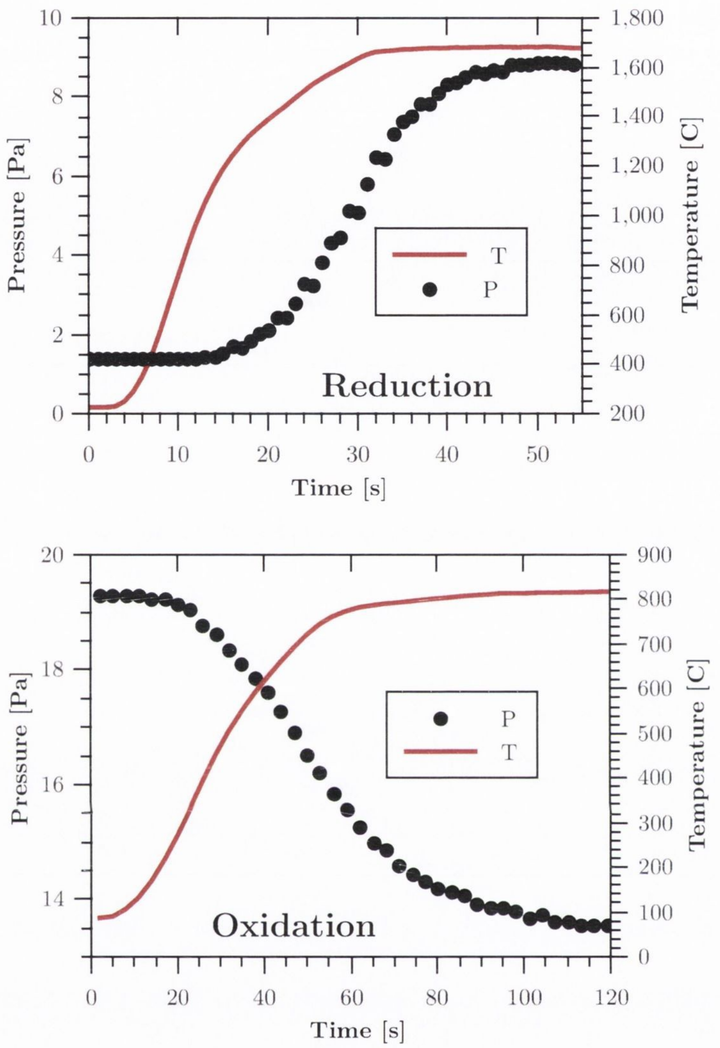

Figure 4.11: Typical raw data measurements taken during a reduction and an oxidation.

The oxidation reaction also proceeds more slowly, which may be due to the higher annealing temperature reducing the surface area. Figure 4.12 shows the rate of oxidation for several different samples. Overall the oxidation kinetics are much slower than those shown in Fig. 4.8, however the same trend of the reaction rate decreasing for increasing Zr concentration is evi-

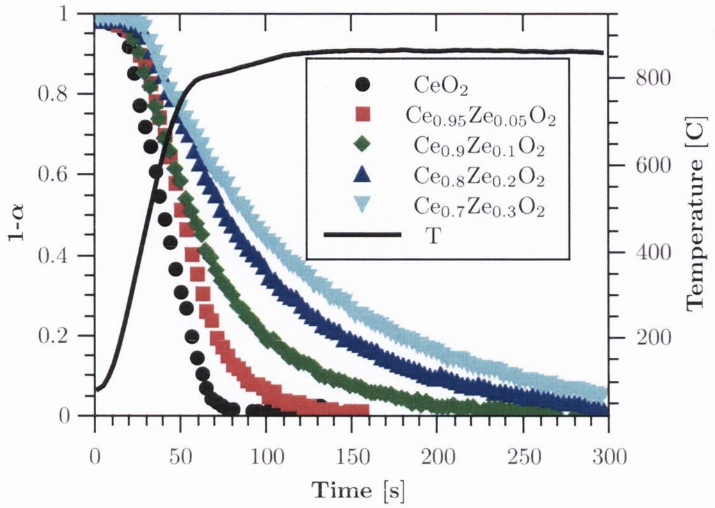

Figure 4.12: The fraction of remaining vacancies $(1-\alpha)$ vs. time during oxidation reactions for a number of different Zr concentrations (DLR samples).

dent. Here, even more concentrations were examined which more conclusively shows the decrease in oxidation rate for increasing Zr dopant concentration.

If the analysis approach is correct then we would expect there to be no change in activation energy when we compare samples of the same Zr concentration. The slower reaction rate must be due to a reduced frequency factor which may be a result of lower surface area and reduced porosity. We can check this by comparing the DLR samples to those produced by the author.

Again we analyse the data according to Eqn. 4.5 and make an Arrhenius plot.

Figure 4.13 shows Arrhenius plots of both a DLR 10 % Zr sample and one of the 10 % Zr samples analysed in Section 4.3.3. The TCD sample shows a linear relationship over all points. The DLR sample initially appears to be linear with the same slope as the TCD sample, but with a much lower

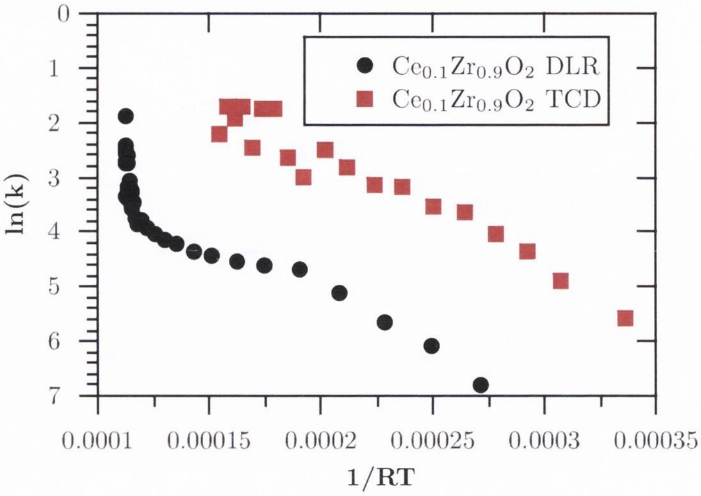

Figure 4.13: A plot of $\ln(k)$ vs. $\frac{1}{RT}$ for the 10 % Zr doped samples produced at DLR (Black) compared to those produced by the author (Red).

intercept. This would imply that at the initial stages of the reaction the kinetics of the DLR sample appear to be well described by our reaction model. The two samples would have the same activation energy, but the DLR sample would have a much lower frequency factor which would explain the much slower rate. However, as the reaction proceeds there is a clear deviation from the linear relationship. At approximately 660 °C ($\frac{1}{RT} = 0.00018$) there is a turning point where both the slope and the activation energy decrease significantly. This is likely due to the model no longer holding due to some other effect becoming the rate controlling step.

The reaction could now be diffusion controlled, with the diffusion of vacancies in the bulk now playing the main role in the oxidation kinetics. Increasing the power factor on the $(1 - \alpha)$ term did not give a straight line, and the kink remained in the same position. The full diffusion equation with our model as the boundary condition could be necessary to correctly model the material. It could also be the case that there are trapped volumes (due to the lower porosity) inside the sample which slows the reaction after a certain point. The results obtained from SEM, XRD and XPS should help to determine what the cause of the deviation is and what reaction model might best describe the new kinetics observed.

Reduction

A number of issues make it difficult to measure the kinetics of the reduction reaction in a reproducible way. One problem, which at the time of writing this thesis had only recently been realised, is that the output power of the xenon lamp is unstable for the first 30 seconds after it is turned on. This was addressed by blocking the lamp with the shutter for 40 seconds and then uncovering the lamp with the shutter at maximum speed. This offered a much more reproducible heating curve which should allow different reductions to be directly compared.

The oxidation results for the DLR samples showed greater pressure changes and slower kinetics than the samples produced by the authors. The samples produced by the authors show no noticeable difference in reduction kinetics and due to the speed of reduction and inconsistencies with the lamp output power the resolution of this reaction was very poor. In an attempt to get some information on the reduction reaction the DLR samples were analysed using the heating method described above, the hope being that the lower activity of these samples compared to the authors samples might slow the reduction enough to observe its kinetics.

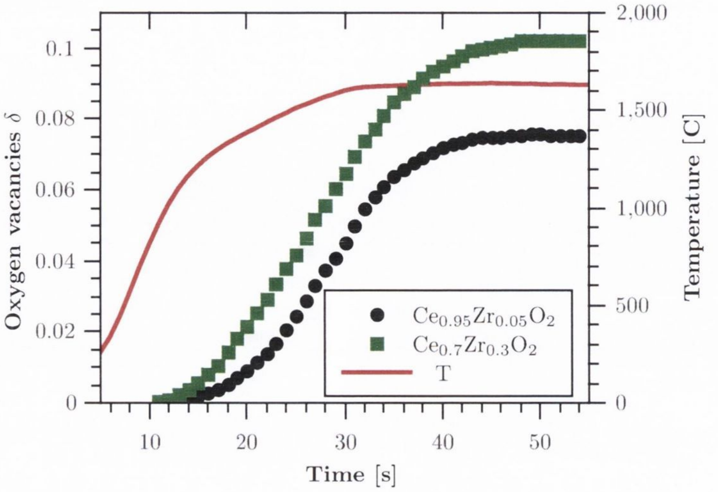

Figure 4.14: A plot of δ and T vs. time for the reduction of 5 and 30 % Zr doped samples.

We see in Fig. 4.14 the reduction rate for two of the DLR samples with two different dopant concentrations. The sample with 30 % Zr dopant reaches a higher reduction state which is expected, but there are no obvious differences in the reaction kinetics. Both samples begin to release oxygen at around the same stage and also reach equilibrium at the upper temperature at the same time. It is most likely that the kinetics are limited by the heating rate. The samples may not be exactly uniformly heated leading to the reaction apparently reaching equilibrium after temperature reaches equilibrium.

From this we can conclude that the reduction reaction kinetics are very rapid and in most practical cases they will be limited by either heating rate or gas phase transport. It may be possible to extract some small amount of information from our reduction kinetics but any attempt at fitting Arrhenius plots to the kinetics would not be physical.

4.5 Conclusions

In ceria, Zr and Hf dopants were found to increase the high temperature stability. This was concluded from the SEM images, and the extent of sample shrinkage during annealing of the samples. These dopants were also found to reduce the rate of oxidation. Arrhenius fits showed that the dopants reduced E_{ox} by approximately $10\,\mathrm{kJ\,mol^{-1}}$ (from 33 to $20\,\mathrm{kJ\,mol^{-1}}$), but also greatly reduced the A_{ox}. The decrease in A_{ox} was enough to reduce the reaction kinetics at the temperatures considered. The rate of oxidation was also seen to decrease with increasing Zr concentration.

Oxidation and reduction of ceria samples produced by the DLR of the form $\mathrm{Ce}_{1-x}\mathrm{Zr}_x\mathrm{O}_2$, with x varied in the range 0–0.3 in steps of 0.05, were also analysed. The samples were larger in mass and offered better resolution in the measurement of pressure changes in the system. These samples confirmed the effect of Zr on the oxidation kinetics, with the oxidation rate decreasing with increasing Zr concentration. Arrhenius plots showed an initial slope similar to the sample produced by the author, but the results deviated from a straight line suggesting that a different approach was needed for later stages of the reaction. This is most likely due to the higher temperature at which the samples were annealed resulting in a lower surface area and thus making bulk diffusion more important.

The DLR samples combined with some minor changes in experimental procedure also offered better insight into the reduction reaction. Upon heating from 1000 °C to 1650 °C in 20 seconds no difference was seen in the reduction kinetics of different samples, as they all appeared to simply follow the heating rate. This suggests that reduction is very rapid and in most practical cases would almost certainly be limited by heating rate or gas phase transport.

Conclusions and Outlook

Conclusions

n Chapter 2 an analytical model of ceria reduction and oxidation was developed. The system is modelled as an equilibrium reaction with Arrhenius rate constants. It predicts both equilibrium composition and reaction kinetics of oxidation and reduction in oxygen atmosphere. A very useful application was demonstrated by coupling the model to a radiative heating simulation of a hypothetical cavity reactor. This allowed the reduction step of a thermochemical reaction to be analysed. The model should prove useful for optimising reactor designs via FEM simulations. The model is also utilised in the later chapters.

The thermodynamic energy costs and performance of the ceria fuel production cycle were analysed in Chapter 3. For cycles operating at ambient pressure the maximum efficiency was found to be very low ($\approx 4.5\%$ for $T_{\mathrm{rd}} = 1500$ °C) due to the very large amounts of sweep gas required to reduce the oxygen partial pressure. Isothermal cycles had very low efficiency ($< 2\%$) under all conditions due to the excessive amounts of oxidiser required for the oxidation reaction.

The effect of pumping the system to reduce the oxygen partial pressure was also considered. The pumping efficiency was given a pressure dependence, which was determined from the specifications of commercially available pumps. In addition, instead of trying to recycle the heat from the ceria by exchanging it between hot and cold ceria, it is proposed this heat should simply be converted to process heat for powering the vacuum pumps and heating the oxidiser. Assuming 60% solid state heat recovery the efficiency was maximised with respect to the cycle operating conditions (reduction pressure, temperature swing and extent of the oxidation reaction) giving a peak efficiency of 11%.

Finally the amount of ceria which is needed per kW output power was investigated. For the normal cycle conditions considered, the amount of ceria required was extremely excessive and likely detrimental to any large scale implementation of this technology. Combined with the results of the efficiency, it seems that great improvements are needed if this cycle is to become competitive with more standard methods of renewable fuel production such as photovoltaic powered electrolysis. Some core technologies need to be developed, such as efficient vacuum pumps and high temperature heat exchangers for the oxidiser and for cooling the ceria. The use of dopants to improve both the yield and cycle time, would also improve both the efficiency and the practicality of the cycle.

In the final chapter, structural characterisations and the results of the reduction and oxidation experiments for both pure and doped ceria are presented. The dopants used were Zr and Hf, which are known to improve the reducibility of ceria. These dopants replace ceria in the fluorite phase making materials of the form, $Ce_{1-x}M_xO_2$ (M=Zr or Hf), with values of x up to 0.2. From SEM images and a lower volume shrinkage of porous pellets during annealing, it was concluded that both Zr and Hf improved the high temperature stability of ceria. The dopants were also shown to slow down the rate of oxidation with the lower rates for higher dopant concentrations.

The oxidation results obtained for each sample were fit with an Arrhenius plot and the values of E_{ox} and A_{ox} were determined. The dopants reduced the value of E_{ox}, but also greatly reduced the value of A_{ox}, which reduced the overall oxidation rate.

Samples produced by the DLR, with a better spread of Zr concentrations also confirmed the trend of deceasing oxidation rates for increasing dopant concentrations. The results from these samples also suggested that for larger grain sizes it may be necessary to consider the diffusion as a rate controlling step.

Reduction of the DLR samples was performed in a more reproducible way than for previous samples. The results suggested that even with very high heating rates (≥ 50 C°s^{-1}), the reduction rate was controlled by the heating rate. This means that in most practical situations reduction rates will simply be limited by heating rates or gas phase transport properties.

Outlook

All three aspects of the work can be linked together using a thermogravimetric study of ceria doped with Zr. This will allow the equilibrium data of doped ceria to be fitted by the analytical model developed in Chapter 2.

The oxidation kinetics obtained in Chapter 4 combined with the parameters obtained from fitting the equilibrium data can be used to form a complete model describing the doped materials. This model can be used for heat flow simulations and used in the thermodynamic analysis presented in Chapter 3. These thermogravimetric experiments are currently being planned with our colleagues in the DLR.

Another issue that we aim to address is the reduced reaction kinetics of doped ceria. These reduced oxidation rates may be more pronounced for oxidation in H_2O and CO_2, which could increase heat losses during oxidation. It is believed that the addition of small amounts of ions with a lower valence than Ce^{4+}, such as Sm^{3+} and La^{3+}, which improve the oxygen ion mobility [103, 104], will also improve the oxidation kinetics. The DLR have already completed thermogravimetric studies of ceria doped with Zr and small amounts of Sm or La. It remains for the author to perform oxidation and reduction analysis to determine the effect on the kinetics.

Finally, the author believes that the work described in this thesis offers a good step forward in understanding and assessing these fuel production technologies. The kinetic model can be used in reactor design and combined with the thermodynamic analysis should allow for more informed reactor and cycle selection. Finally the reaction kinetics show that reduction rates in a reactor can be controlled and improved by controlling the heating rates and gas phase transport and assessing the effect of dopants on the oxidation rates remains a key question.

Bibliography

[1] B. J. McBride, S. Gordon, and M. A. Reno. Thermodynamic data for fifty reference elements. *NASA Technical Paper*, 3287, 1993.

[2] L. B. Pankratz and R. V. Mrazek. Thermodynamic properties of elements and oxides. *US Bureau of Mines Bulletin*, 672, 1982.

[3] T. F. Stocker and D. Qin. Climate change 2013, the physical science basis. Technical Report 5, Intergovernmental Panel on Climate Change, 2014.

[4] F. Christopher and O. Jean Pierre. Climate change 2014, impacts, adaptation, and vulnerability. Technical Report 5, Intergovernmental Panel on Climate Change, 2014.

[5] T. Hernandez-Tejeda and R. Quadrelli. Climate change 2014, mitigation of climate change. Technical Report 5, Intergovernmental Panel on Climate Change, 2014.

[6] S. Vazquez, S. Lukic, E. Galvan, L. Franquelo, and J. Carrasco. Energy storage systems for transport and grid applications. *Industrial Electronics, IEEE Transactions on*, 57(12):3881–3895, Dec 2010.

[7] J. Kopyscinski, T. J. Schildhauer, and S. M. Biollaz. Production of synthetic natural gas (sng) from coal and dry biomass a technology review from 1950 to 2009. *Fuel*, 89(8):1763 – 1783, 2010.

[8] J. O. Bockris. The hydrogen economy: Its history. *International Journal of Hydrogen Energy*, 38(6):2579 – 2588, 2013.

[9] J. J. Cheng and G. R. Timilsina. Status and barriers of advanced biofuel technologies: A review. *Renewable Energy*, 36(12):3541 – 3549, 2011.

[10] A. Demirbas. Political, economic and environmental impacts of biofuels: A review. *Applied Energy*, 86, Supplement 1(0):S108 – S117, 2009. Bio-fuels in Asia.

[11] M. G. Walter, E. L. Warren, J. R. McKone, S. W. Boettcher, Q. Mi, E. A. Santori, and N. S. Lewis. Solar water splitting cells. *Chemical Reviews*, 110(11):6446–6473, 2010.

[12] A. Fujishima and K. Honda. Electrochemical photolysis of water at a semiconductor electrode. *Nature*, 238(5358):37–38, 1972.

[13] M. Ni, M. K. Leung, D. Y. Leung, and K. Sumathy. A review and recent developments in photocatalytic water-splitting using for hydrogen production. *Renewable and Sustainable Energy Reviews*, 11(3):401 – 425, 2007.

[14] I. S. Direct thermal decomposition of water. In *Solar-hydrogen energy systems*, pages 59 – 79. Pergamon Press, Oxford and New York, 1979.

[15] A. Kogan. Direct solar thermal splitting of water and on site separation of the products i. theoretical evaluation of hydrogen yield. *International Journal of Hydrogen Energy*, 22(5):481 – 486, 1997.

[16] S. Baykara. Hydrogen production by direct solar thermal decomposition of water, possibilities for improvement of process efficiency. *International Journal of Hydrogen Energy*, 29(14):1451 – 1458, 2004.

[17] C. Bale, P. Chartrand, S. Degterov, G. Eriksson, K. Hack, R. Ben Mahfoud, J. Melançon, A. Pelton, and S. Petersen. Factsage thermochemical software and databases. *Calphad*, 26(2):189–228, 2002.

[18] C. Bale, E. Bélisle, P. Chartrand, S. Decterov, G. Eriksson, K. Hack, I.-H. Jung, Y.-B. Kang, J. Melançon, A. Pelton, et al. Factsage thermochemical software and databasesrecent developments. *Calphad*, 33(2):295–311, 2009.

[19] A. Kogan. Direct solar thermal splitting of water and on-site separation of the products iv. development of porous ceramic membranes for a solar thermal water-splitting reactor. *International Journal of Hydrogen Energy*, 25(11):1043 – 1050, 2000.

[20] H. Ohya, M. Yatabe, M. Aihara, Y. Negishi, and T. Takeuchi. Feasibility of hydrogen production above 2500 K by direct thermal decomposition reaction in membrane reactor using solar energy. *International Journal of Hydrogen Energy*, 27(4):369 – 376, 2002.

[21] A. Kogan. Direct solar thermal splitting of water and on-site separation of the productsii. experimental feasibility study. *International Journal of Hydrogen Energy*, 23(2):89 – 98, 1998.

[22] A. Kogan, E. Spiegler, and M. Wolfshtein. Direct solar thermal splitting of water and on-site separation of the products. iii.: Improvement of reactor efficiency by steam entrainment. *International Journal of Hydrogen Energy*, 25(8):739 – 745, 2000.

[23] S. Baykara. Experimental solar water thermolysis. *International Journal of Hydrogen Energy*, 29(14):1459 – 1469, 2004.

[24] J. E. Funk. Thermochemical hydrogen production: past and present. *International Journal of Hydrogen Energy*, 26(3):185 – 190, 2001.

[25] J. Funk and R. Reinstrom. *System study of hydrogen generation by thermal energy*. Jun 1964.

[26] J. E. Funk and R. M. Reinstrom. Energy requirements in production of hydrogen from water. *Industrial & Engineering Chemistry Process Design and Development*, 5(3):336–342, 1966.

[27] J. Funk. Thermochemical production of hydrogen via multistage water splitting processes. *International Journal of Hydrogen Energy*, 1(1):33 – 43, 1976.

[28] D. R. O'keefe, J. H. Norman, and D. G. Williamson. Catalysis research in thermochemical water-splitting processes. *Catalysis Reviews*, 22(3):325–369, 1980.

[29] C. Bamberger and D. Richardson. Hydrogen production from water by thermochemical cycles. *Cryogenics*, 16(4):197 – 208, 1976.

[30] J. Russell, J.L. and J. Porter. A search for thermochemical water-splitting cycles. In T. Vezirolu, editor, *Hydrogen Energy*, pages 517–529. Springer US, 1975.

[31] J. Pangborn and J. Sharer. Analysis of thermochemical water-splitting cycles. In T. N. Vezirolu, editor, *Hydrogen Energy*, pages 499–515. Springer US, 1975.

[32] R. Shinnar, D. Shapira, and S. Zakai. Thermochemical and hybrid cycles for hydrogen production. a differential economic comparison with electrolysis. *Industrial & Engineering Chemistry Process Design and Development*, 20(4):581–593, 1981.

[33] J. M. Ogden. Prospects for building a hydrogen energy infrastructure. *Annual Review of Energy and the Environment*, 24(1):227–279, 1999.

[34] G. Besenbruch, K. McCorkle, J. Norman, D. OKeefe, J. Schuster, P. Trester, and M. Yoshimoto. *Hydrogen production by the GA sulfur-iodine process: a progress report.* May 1980.

[35] L. Brecher, S. Spewock, and C. Warde. The westinghouse sulfur cycle for the thermochemical decomposition of water. *International Journal of Hydrogen Energy*, 2(1):7 – 15, 1977.

[36] A. Terada, J. Iwatsuki, S. Ishihara, H. Noguchi, S. Kubo, H. Okuda, S. Kasahara, N. Tanaka, H. Ota, K. Onuki, and R. Hino. Development of hydrogen production technology by thermochemical water splitting. process pilot test plan. *Journal of Nuclear Science and Technology*, 44(3):477–482, 2007.

[37] Hythec: An {EC} funded search for a long term massive hydrogen production route using solar and nuclear technologies. *International Journal of Hydrogen Energy*, 32(1011):1516 – 1529, 2007. {EHEC2005}.

[38] A. Yogev, A. Kribus, M. Epstein, and A. Kogan. Solar tower reflector systems: A new approach for high-temperature solar plants. *International Journal of Hydrogen Energy*, 23(4):239 – 245, 1998.

[39] D. Barlev, R. Vidu, and P. Stroeve. Innovation in concentrated solar power. *Solar Energy Materials and Solar Cells*, 95(10):2703 – 2725, 2011.

[40] A. Steinfeld, P. Kuhn, A. Reller, R. Palumbo, J. Murray, and Y. Tamaura. Solar-processed metals as clean energy carriers and water-splitters. *International Journal of Hydrogen Energy*, 23(9):767–774, 1998.

[41] C. Perkins and A. W. Weimer. Likely near-term solar-thermal water splitting technologies. *International Journal of Hydrogen Energy*, 29(15):1587 – 1599, 2004.

[42] S. Abanades, P. Charvin, G. Flamant, and P. Neveu. Screening of water-splitting thermochemical cycles potentially attractive for Hydrogen production by concentrated solar energy. *Energy*, 31(14):2805 – 2822, 2006.

[43] T. Nakamura. Hydrogen production from water utilizing solar heat at high temperatures. *Solar Energy*, 19(5):467 – 475, 1977.

[44] S. Licht. Thermochemical solar hydrogen generation. *Chem. Commun.*, pages 4635–4646, 2005.

[45] T. Kodama and N. Gokon. Thermochemical cycles for high-temperature solar Hydrogen production. *Chemical Reviews*, 107(10):4048–4077, 2007.

[46] F. Sibieude, M. Ducarroir, A. Tofighi, and J. Ambriz. High temperature experiments with a solar furnace: The decomposition of fe3o4, mn3o4, cdo. *International Journal of Hydrogen Energy*, 7(1):79 – 88, 1982.

[47] T. Kodama. High-temperature solar chemistry for converting solar heat to chemical fuels. *Progress in Energy and Combustion Science*, 29(6):567 – 597, 2003.

[48] A. Steinfeld. Solar thermochemical production of Hydrogena review. *Solar Energy*, 78(5):603 – 615, 2005.

[49] M. D. Allendorf, R. B. Diver, J. E. Miller, and N. P. Siegel. Thermodynamic analysis of mixed-metal ferrites for hydrogen production by two-step water splitting. In *ASME 2006 International Solar Energy Conference*, pages 285–290. American Society of Mechanical Engineers, 2006.

[50] M. D. Allendorf, R. B. Diver, N. P. Siegel, and J. E. Miller. Two-step water splitting using mixed-metal ferrites: thermodynamic analysis and characterization of synthesized materials. *Energy & Fuels*, 22(6):4115–4124, 2008.

[51] H. Kaneko, T. Kodama, N. Gokon, Y. Tamaura, K. Lovegrove, and A. Luzzi. Decomposition of Zn-ferrite for O_2 generation by concentrated solar radiation. *Solar Energy*, 76(1-3):317 – 322, 2004. Solar World Congress 2001.

[52] F. Fresno, T. Yoshida, N. Gokon, R. Fernndez-Saavedra, and T. Kodama. Comparative study of the activity of Nickel ferrites for solar Hydrogen production by two-step thermochemical cycles. *International Journal of Hydrogen Energy*, 35(16):8503 – 8510, 2010.

[53] M. Inoue, N. Hasegawa, R. Uehara, N. Gokon, H. Kaneko, and Y. Tamaura. Solar hydrogen generation with $H_2O/ZnO/MnFe_2O_4$ system. *Solar Energy*, 76(1-3):309 – 315, 2004. Solar World Congress 2001.

[54] F. Fresno, R. Fernndez-Saavedra, M. B. Gmez-Mancebo, A. Vidal, M. Snchez, M. I. Rucandio, A. J. Quejido, and M. Romero. Solar Hydrogen production by two-step thermochemical cycles: Evaluation of the activity of commercial ferrites. *International Journal of Hydrogen Energy*, 34(7):2918 – 2924, 2009.

[55] H. Kaneko, T. Yokoyama, A. Fuse, H. Ishihara, N. Hasegawa, and Y. Tamaura. Synthesis of new ferrite, AlCu ferrite, and its oxygen deficiency for solar H_2 generation from H_2O. *International Journal of Hydrogen Energy*, 31(15):2256 – 2265, 2006.

[56] T. Kodama, Y. Kondoh, R. Yamamoto, H. Andou, and N. Satou. Thermochemical hydrogen production by a redox system of ZrO_2-supported Co(II)-ferrite. *Solar Energy*, 78(5):623 – 631, 2005. ¡ce:title¿Solar Hydrogen¡/ce:title¿.

[57] T. Kodama, N. Gokon, and R. Yamamoto. Thermochemical two-step water splitting by ZrO_2-supported $Ni_xFe_{3x}O_4$ for solar hydrogen production. *Solar Energy*, 82(1):73 – 79, 2008.

[58] R. B. Diver, J. E. Miller, M. D. Allendorf, N. P. Siegel, and R. E. Hogan. Solar thermochemical water-splitting ferrite-cycle heat engines. *Journal of Solar Energy Engineering*, 130(4):041001–041009, 2008.

[59] J. E. Miller, L. R. Evans, J. N. Stuecker, M. D. Allendorf, N. P. Siegel, and R. B. Diver. Materials development for the cr5 solar thermochemical heat engine. In *ASME 2006 International Solar Energy Conference*, pages 311–320. American Society of Mechanical Engineers, 2006.

[60] J. E. Miller, M. D. Allendorf, R. B. Diver, L. Evans, N. P. Siegel, and J. Stuecker. Metal oxide composites and structures for ultra-high temperature solar thermochemical cycles. *Journal of Materials Science*, 43:4714–4728, 2008.

[61] R. B. Diver, J. E. Miller, N. P. Siegel, and T. A. Moss. Testing of a cr5 solar thermochemical heat engine prototype. In *ASME 2010 4th International Conference on Energy Sustainability*, pages 97–104. American Society of Mechanical Engineers, 2010.

[62] N. Gokon, S. Takahashi, H. Yamamoto, and T. Kodama. Thermochemical two-step water-splitting reactor with internally circulating fluidized bed for thermal reduction of ferrite particles. *International Journal of Hydrogen Energy*, 33(9):2189–2199, 2008.

[63] N. Gokon, S. Takahashi, H. Yamamoto, and T. Kodama. New solar water-splitting reactor with ferrite particles in an internally circulating fluidized bed. *Journal of Solar Energy Engineering*, 131(1):011007, 2009.

[64] N. Gokon, T. Mataga, N. Kondo, and T. Kodama. Thermochemical two-step water splitting by internally circulating fluidized bed of $NiFe_2O_4$ particles: Successive reaction of thermal-reduction and water-decomposition steps. *International Journal of Hydrogen Energy*, 36(8):4757 – 4767, 2011.

[65] M. Roeb, A. G. Konstandopoulos, A. Steele, P. Stobbe, C. Agrafiotis, C. Sattler, R. Klüser, V. Zaspalis, L. Nalbandian, N. Monnerie, et al. Solar hydrogen production by a two-step cycle based on mixed iron oxides. *Journal of Solar Energy Engineering*, 128(2):125–133, 2006.

[66] M. Roeb, M. Neises, J.-P. Säck, P. Rietbrock, N. Monnerie, J. Dersch, M. Schmitz, and C. Sattler. Operational strategy of a two-step thermochemical process for solar hydrogen production. *International Journal of Hydrogen Energy*, 34(10):4537–4545, 2009.

[67] M. Roeb, J.-P. Säck, P. Rietbrock, C. Prahl, H. Schreiber, M. Neises, L. De Oliveira, D. Graf, M. Ebert, W. Reinalter, et al. Test operation of a 100kw pilot plant for solar hydrogen production from water on a solar tower. *Solar Energy*, 85(4):634–644, 2011.

[68] J.-P. Sck, M. Roeb, C. Sattler, R. Pitz-Paal, and A. Heinzel. Development of a system model for a hydrogen production process on a solar tower. *Solar Energy*, 86(1):99 – 111, 2012.

[69] A. Houaijia, C. Sattler, M. Roeb, M. Lange, S. Breuer, and J. P. Säck. Analysis and improvement of a high-efficiency solar cavity reactor design for a two-step thermochemical cycle for solar hydrogen production from water. *Solar Energy*, 97(0):26 – 38, 2013.

[70] H. Villafán-Vidales, C. Arancibia-Bulnes, U. Dehesa-Carrasco, and H. Romero-Paredes. Monte Carlo radiative transfer simulation of a cavity solar reactor for the reduction of Cerium oxide. *International Journal of Hydrogen Energy*, 34(1):115 – 124, 2009.

[71] I. Vishnevetsky, A. Berman, and M. Epstein. Features of solar thermochemical redox cycles for Hydrogen production from water as a function of reactants main characteristics. *International Journal of Hydrogen Energy*, 36(4):2817 – 2830, 2011.

[72] R. Palumbo, J. Lede, O. Boutin, E. Elorza Ricart, A. Steinfeld, S. Möller, A. Weidenkaff, E. Fletcher, and J. Bielicki. The production of zn from zno in a high-temperature solar decomposition quench process. the scientific framework for the process. *Chemical Engineering Science*, 53(14):2503–2517, 1998.

[73] A. Steinfeld. Solar hydrogen production via a two-step water-splitting thermochemical cycle based on zn/zno redox reactions. *International Journal of Hydrogen Energy*, 27(6):611–619, 2002.

[74] P. G. Loutzenhiser, A. Meier, and A. Steinfeld. Review of the two-step h2o/co2-splitting solar thermochemical cycle based on zn/zno redox reactions. *Materials*, 3(11):4922–4938, 2010.

[75] R. Palumbo, M. Keunecke, S. Möller, and A. Steinfeld. Reflections on the design of solar thermal chemical reactors: thoughts in transformation. *Energy*, 29(5):727–744, 2004.

[76] L. O. Schunk, A. Steinfeld, P. Haeberling, S. Wepf, D. Wuillemin, and A. Meier. A receiver-reactor for the solar thermal dissociation of zinc oxide. *Journal of Solar Energy Engineering*, 130(2):021009, 2008.

[77] D. Gstoehl, A. Brambilla, L. Schunk, and A. Steinfeld. A quenching apparatus for the gaseous products of the solar thermal dissociation of zno. *Journal of Materials Science*, 43(14):4729–4736, 2008.

[78] M. Roeb, M. Neises, N. Monnerie, F. Call, H. Simon, C. Sattler, M. Schmücker, and R. Pitz-Paal. Materials-related aspects of thermochemical water and carbon dioxide splitting: A review. *Materials*, 5(11):2015–2054, 2012.

[79] S. Abanades, P. Charvin, F. Lemont, and G. Flamant. Novel two-step sno_2/sno water-splitting cycle for solar thermochemical production of hydrogen. *International Journal of Hydrogen Energy*, 33(21):6021–6030, 2008.

[80] S. Abanades and M. Chambon. Co_2 dissociation and upgrading from two-step solar thermochemical processes based on zno/zn and sno_2/sno redox pairs. *Energy & Fuels*, 24(12):6667–6674, 2010.

[81] G. Levêque, S. Abanades, J.-C. Jumas, and J. Olivier-Fourcade. Characterization of two-step tin-based redox system for thermochemical fuel production from solar-driven CO_2 and H_2O splitting cycle. *Industrial & Engineering Chemistry Research*, 53(14):5668–5677, 2014.

[82] A. Trovarelli. Structural and Oxygen storage/release properties of CeO_2-based solid solutions. *Comments on Inorganic Chemistry*, 20(4-6):263–284, 1999.

[83] H. Imagawa, A. Suda, K. Yamamura, and S. Sun. Monodisperse ceo2 nanoparticles and their oxygen storage and release properties. *The Journal of Physical Chemistry C*, 115(5):1740–1745, 2011.

[84] E. Subbarao and H. Maiti. Solid electrolytes with oxygen ion conduction. *Solid State Ionics*, 11(4):317 – 338, 1984.

[85] E. L. Wilson, R. Grau-Crespo, C. L. Pang, G. Cabailh, Q. Chen, J. A. Purton, C. R. A. Catlow, W. A. Brown, N. H. de Leeuw, and G. Thornton. Redox behavior of the model catalyst pd/ceo2x/pt(111). *The Journal of Physical Chemistry C*, 112(29):10918–10922, 2008.

[86] M. Nolan, S. C. Parker, and G. W. Watson. Reduction of no2 on ceria surfaces. *The Journal of Physical Chemistry B*, 110(5):2256–2262, 2006.

[87] V. Kharton, F. Figueiredo, L. Navarro, E. Naumovich, A. Kovalevsky, A. Yaremchenko, A. Viskup, A. Carneiro, F. Marques, and J. Frade. Ceria-based materials for solid oxide fuel cells. *Journal of Materials Science*, 36:1105–1117, 2001.

[88] A. Stambouli and E. Traversa. Solid oxide fuel cells (SOFCs): a review of an environmentally clean and efficient source of energy. *Renewable and Sustainable Energy Reviews*, 6(5):433 – 455, 2002.

[89] K. Otsuka, M. Hatano, and A. Morikawa. Decomposition of water by cerium oxide of δ-phase. *Inorganica chimica acta*, 109(3):193–197, 1985.

[90] S. Abanades and G. Flamant. Thermochemical hydrogen production from a two-step solar-driven water-splitting cycle based on cerium oxides. *Solar Energy*, 80(12):1611 – 1623, 2006.

[91] R. Panlener, R. Blumenthal, and J. Garnier. A thermodynamic study of nonstoichiometric Cerium dioxide. *Journal of Physics and Chemistry of Solids*, 36(11):1213 – 1222, 1975.

[92] W. C. Chueh and S. M. Haile. A thermochemical study of Ceria: exploiting an old material for new modes of energy conversion and CO_2 mitigation. *Philosophical Transactions of the Royal Society A: Mathematical, Physical and Engineering Sciences*, 368(1923):3269–3294, 2010.

[93] P. Furler, J. R. Scheffe, and A. Steinfeld. Syngas production by simultaneous splitting of H_2O and CO_2 via ceria redox reactions in a high-temperature solar reactor. *Energy Environ. Sci.*, 5:6098–6103, 2012.

[94] E. Kümmerle and G. Heger. The structures of CCe_2O_{3+}, Ce_7O_{12}, and $Ce_{11}O20$. *Journal of Solid State Chemistry*, 147(2):485–500, 1999.

[95] M. Zinkevich, D. Djurovic, and F. Aldinger. Thermodynamic modelling of the Cerium Oxygen system. *Solid State Ionics*, 177(1112):989 – 1001, 2006.

[96] B. Bulfin, B. Murphy, O. Lubben, S. Krasnikov, and I. Shvets. Finite element method simulations of heat flow in fixed bed solar water splitting redox reactors. *International Journal of Hydrogen Energy*, 37(13):10028 – 10035, 2012.

[97] M. E. Dry. High quality diesel via the FischerTropsch process a review. *Journal of Chemical Technology & Biotechnology*, 77(1):43–50, 2002.

[98] M. E. Dry. The fischertropsch process: 19502000. *Catalysis Today*, 71(34):227 – 241, 2002.

[99] L. J. Venstrom, R. M. De Smith, Y. Hao, S. M. Haile, and J. H. Davidson. Efficient splitting of co2 in an isothermal redox cycle based on ceria. *Energy & Fuels*, 28(4):2732–2742, 2014.

[100] H. Kaneko, T. Miura, A. Fuse, H. Ishihara, S. Taku, H. Fukuzumi, Y. Naganuma, and Y. Tamaura. Rotary-type solar reactor for solar Hydrogen production with two-step water splitting process. *Energy & Fuels*, 21(4):2287–2293, 2007.

[101] H. Kaneko, Y. Ishikawa, C.-i. Lee, G. Hart, W. Stein, and Y. Tamaura. Simulation study of tokyo tech rotary-type solar reactor on solar field test at csiro in australia. In *ASME 2011 5th International Conference on Energy Sustainability*, pages 1673–1680. 2011.

[102] W. C. Chueh, C. Falter, M. Abbott, D. Scipio, P. Furler, S. M. Haile, and A. Steinfeld. High-flux solar-driven thermochemical dissociation of CO_2 and H_2O using nonstoichiometric Ceria. *Science*, 330(6012):1797–1801, 2010.

[103] H. Yahiro, Y. Eguchi, K. Eguchi, and H. Arai. Oxygen ion conductivity of the ceria-samarium oxide system with fluorite structure. *Journal of Applied Electrochemistry*, 18(4):527–531, 1988.

[104] X. Qi, Y. Lin, C. Holt, and S. Swartz. Electric conductivity and oxygen permeability of modified cerium oxides. *Journal of materials science*, 38(5):1073–1079, 2003.

[105] Q.-L. Meng, C. il Lee, S. Shigeta, H. Kaneko, and Y. Tamaura. Solar hydrogen production using $Ce_{1x}Li_xO_2$ solid solutions via a thermochemical, two-step water-splitting cycle. *Journal of Solid State Chemistry*, 194(0):343 – 351, 2012.

[106] Q.-L. Meng, C. il Lee, T. Ishihara, H. Kaneko, and Y. Tamaura. Reactivity of CeO_2-based ceramics for solar Hydrogen production via a two-step water-splitting cycle with concentrated solar energy. *International Journal of Hydrogen Energy*, 36(21):13435 – 13441, 2011.

[107] A. L. Gal and S. Abanades. Catalytic investigation of Ceria-Zirconia solid solutions for solar Hydrogen production. *International Journal of Hydrogen Energy*, 36(8):4739 – 4748, 2011.

[108] A. Le Gal and S. Abanades. Dopant incorporation in ceria for enhanced water-splitting activity during solar thermochemical hydrogen generation. *The Journal of Physical Chemistry C*, 116(25):13516–13523, 2012.

[109] A. Le Gal, S. Abanades, and G. Flamant. CO_2 and H_2O splitting for thermochemical production of solar fuels using nonstoichiometric Ceria and Ceria/Zirconia solid solutions. *Energy & Fuels*, 25(10):4836–4845, 2011.

[110] K.-S. Kang, C.-H. Kim, C.-S. Park, and J.-W. Kim. Hydrogen reduction and subsequent water splittingof Zr-added CeO_2. *J. Ind. Eng. Chem.*, 13(4):657–663, 2007.

[111] D.-J. Kim. Lattice parameters, ionic conductivities, and solubility limits in fluorite-structure mo2 oxide [m= hf4+, zr4+, ce4+, th4+, u4+] solid solutions. *Journal of the American Ceramic Society*, 72(8):1415–1421, 1989.